The Dissertation Committee for Ming Lei Certifies that this is the approved version of the following dissertation:

Nonlinear Optical Characterization of Advanced Electronic Materials

Committee:

Michael Downer, Supervisor

John Keto

Manfred Fink

Greg Sitz

John Ekerdt

Nonlinear Optical Characterization of Advanced Electronic Materials

by

Ming Lei, B.S.

Dissertation

Presented to the Faculty of the Graduate School of

The University of Texas at Austin

in Partial Fulfillment

of the Requirements

for the Degree of

Doctor of Philosophy

The University of Texas at Austin

August 2012

Dedication

To my beloved parents

Acknowledgements

I would like to express my best gratitude to my supervisor, Professor Michael C. Downer for his patient guidance, tremendous advice and inspiring encouragement throughout my entire Ph.D. program. I have learned so much from him, not only on the knowledge level but also on a personal one, which will benefit me a lot in my future career and life endeavors.

I owe my special thanks to our collaborators in SEMATECH: Dr. Jimmy Price, Dr. J. H. Yum, Dr. Gennadi Bersuker, Dr. Wei-e Wang, Dr. Kathy Dunn, Dr. P. Y. Hung, Dr. Man Hoi Wong, and Professor Sanjay Banerjee from Electrical and Computer Engineering Department at University of Texas at Austin. None of this work would be possible without their friendly collaborations and helpful comments and suggestions. I also appreciate Dr. Hualiang Shi, Dr. Huai Huang, Zhuijie Wu and Professor Paul Ho for their helpful training on some semiconductor fabrication process and the collaboration on the TSV project.

I thank my committee members, Professor John Keto, Professor Manfred Fink, Professor Greg Sitz and Professor John Ekerdt for reading this dissertation carefully and support.

For my dear colleagues, Dr. Yongqiang An, Dr. Jimmy Price, Dr. Robert Ehlert, Dr. Rafal Zgadzaj, Dr. Watson Henderson, Aaron Roberts, Zhengyan Li, Xiaohui Gao, Dr. Xiaoming Wang, Junwei Wei, J. C. Sanders, Loucas Loumakos, Neil Fazel, Rick Korzekwa, Hai-En Tsai, Yen-Yu Zhang, I really appreciate your help and great suggestions for my research.

I am deeply grateful to my parents for their love and support that they give me for everything I do and every decision I have made.

Nonlinear Optical Characterization of Advanced Electronic Materials

Ming Lei, Ph.D.

The University of Texas at Austin, 2012

Supervisor: Michael C. Downer

Continuous downscaling of transistor size has been the major trend of the semiconductor industry for the past half century. In recent years, however, fundamental physical limits to continued downscaling were encountered. In order to overcome these limits, the industry experimented --- and continues to experiment --- with many new materials and architectures. Non-invasive, in-line methods of characterizing critical properties of these structures are in demand. This dissertation develops optical second-harmonic generation (SHG) to characterize performance-limiting defects, band alignment or strain distribution in four advanced electronic material systems of current interest: (1) Hot carrier injection (HCI) is a key determinant of the reliability of ultrathin silicon-on-insulator (SOI) devices. We show that time-dependent electrostatic-field-induced SHG probes HCI from SOI films into both native and buried oxides without device fabrication. (2) Band offsets between advanced high-k gate dielectrics and their substrates govern performance-limiting leakage currents, and elucidate interfacial bond structure. We evaluate band offsets of as-deposited and annealed Al_2O_3, HfO_2 and BeO films with Si using internal photoemission techniques. (3) Epi-GaAs films grown on Si combine the high carrier mobility and superior optical properties of III-V semiconductors with the established Si platform, but are susceptible to formation of anti-phase boundary (APB) defects. We show that SHG in reflection from APB-laden epi-films is dramatically

weaker than from control layers without APBs. Moreover, scanning SHG images of APB-rich layers reveal microstructure lacking in APB-free layers. These findings are attributed to the reversal in sign of the second-order nonlinear optical susceptibility $\chi^{(2)}$ between neighboring anti-phase domains, and demonstrate that SHG characterizes APBs sensitively, selectively and non-invasively. (4) 3D integration --- *i.e.* connecting vertically stacked chips with metal through-Si-vias (TSVs) --- is an important new approach for improving performance at the inter-chip level, but thermal stress of the TSVs on surrounding Si can compromise reliability. We present scanning SHG images for different polarization combinations and azimuthal orientations that reveal the sensitivity of SHG to strain fields surrounding TSVs. Taken together, these results demonstrate that SHG can identify performance-limiting defects and important material properties quickly and non-invasively for advanced MOSFET device applications.

Table of Contents

Chapter 1: INTRODUCTION

1.1 CHALLENGES AND CORRESPONDING SOLUTIONS FOR SEMICONDUCTOR DEVICE SCALING

For the past few decades, successful downscaling of Si-based metal-oxide-semiconductor field effect transistors (MOSFETs) has improved circuit functionality and performance, while increasing on-chip package density [1]. Channel length --- *i.e.* the distance between source (S) and drain (D) regions --- has been continuously shortened for each technology node, as shown in Figure 1. This may lead, however, to an undesirable side effect: the threshold voltage becomes channnel-length-dependent, which is called the short-chanel effect, or charge sharing effect [2].

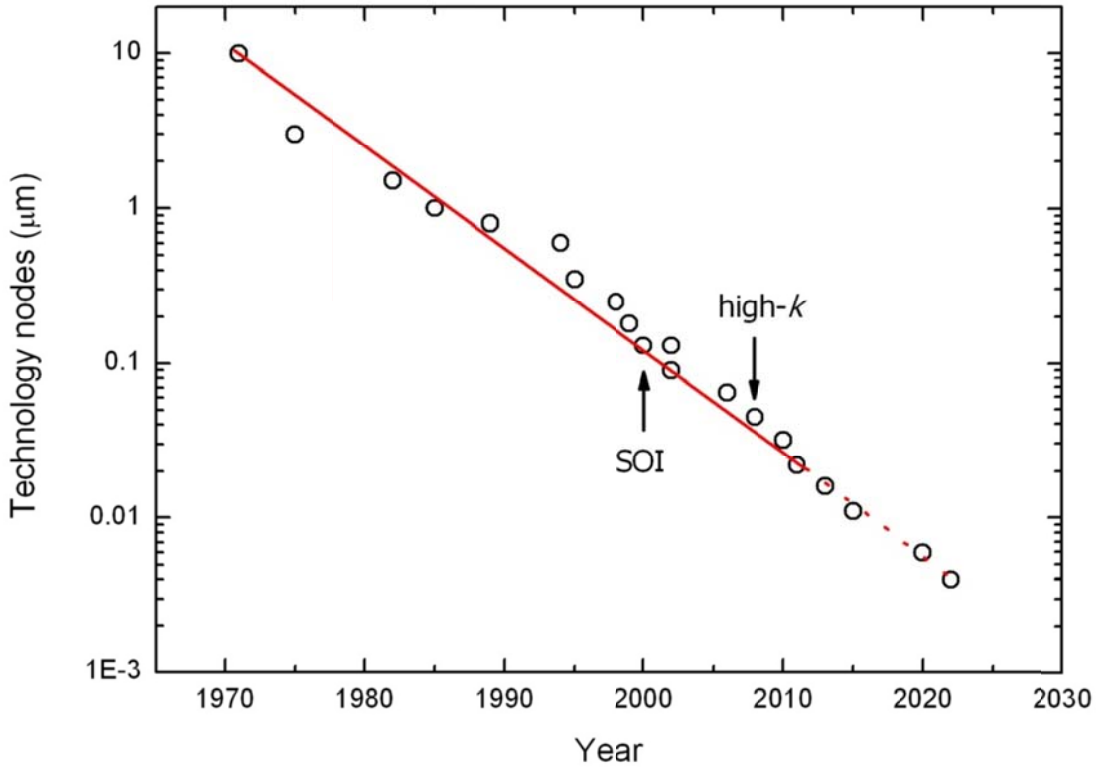

Figure 1: Technology nodes of microprocessor scaling. Arrows indicate the times when a new material/architecture was first introduced into the market. Data is from the International Technology Roadmap for Semiconductors (ITRS).

In general the threshold voltage of a MOSFET can been written as [2]:

$$V_{TH} = V_{FB} + 2\Phi_F - \frac{Q_D}{C_{OX}} \ , \qquad (1)$$

where V_{FB} is the flatband voltage, Φ_F is the Fermi potential, Q_D is the depletion charge density and C_{OX} is the gate capacitance density. Ideally the depletion charge is only controlled by the gate which results in a uniform rectangular field profile along the channel. However due to the extension of S/D electric field towards the channel, some field lines will terminate at S/D rather than gate, resulting in less charge controlled by the gate. This channel length dependence may pose serious manufacturing reproducibility issues due to processing-related statistical variations. One simple solution to solve this issue without sacrificing other device performance requirements is to geometrically confine the depletion region within a crystalline Si film. Vulnerability to charge sharing at the S/D region is then significantly reduced. This is the reason why silicon-on-insulator (SOI) architectures have been widely used in low power consumption and high performance devices [3]. At the same time reliability of short-channel SOI devices is sensitive to hot carrier injection (HCI), which can occur into both gate and buried oxides (BOX) depending on doping, bias condition and oxide quality.[4] Thus accurate characterization of HCI has become a priority of SOI metrology. Recently, several investigators introduced optical second-harmonic generation (SHG) to characterize SOI films thicker than 50 nm.[5-7] These studies demonstrated sensitivity of time-dependent electrostatic field-induced second-harmonic (TD-EFISH) generation to charge injection across the critical interface between the active Si layer and the BOX, which is not easily characterized by conventional electrical techniques. However, competing TD-EFISH contributions of unknown relative phase from simultaneous HCI across the

substrate/BOX interface complicated interpretation of the results, allowing only qualitative measurements of HCI from the SOI layer.

In the work presented in Chapter 2, we employed internal multiphoton photoemission (IMPE) to inject hot carriers optically from *ultrathin* (≤ 10 nm) SOI films into trap sites in the BOX and native oxide (NOX), and TD-EFISH generation to probe subsequent charge trapping kinetics. In addition, through improvements in measurement technique, we demonstrated that HCI across the critical SOI/BOX interface can be measured completely independently of competing charge trapping processes, enabling extraction of its *quantitative* kinetic parameters. IMPE-EFISH complements conventional electrical tests in two ways. First, it requires no device fabrication. Second, as shown below, it straightforwardly distinguishes HCI into BOX from HCI into NOX. Such characterization is especially important for ultrathin SOI because the density of performance-limiting defects near the SOI/BOX interface increases as the SOI layer is chemically thinned. Additionally due to the geometry of SOI wafer, perfect isolation between transistors fabricated on the Si film can be achieved which can prevent CMOS latch-up [3].

As the channel length shortens, gate insulator thickness is reduced commensurately to maintain strong capacitive coupling between the channel and gate terminal. At equivalent oxide thickness less than 10Å, however, this scaling encountered fundamental physical limits. On-state tunnelling leakage current became so large that transistor power consumption and performance was compromised [8-11]. Thus for the sub-65nm technology node, the conventional native thermal gate oxide was replaced by thicker deposited high-*k* dielectrics to prevent tunnelling while maintain the required capacitance density [12]. Meanwhile the required permittivity of advanced gate dielectrics must be balanced against the barrier height for tunneling and thermionic

emission leakage currents, which are governed by the offsets of their conduction and valence bands from those of the substrate [12]. These offsets reflect the atomic structure of the substrate-oxide interface, which is not in general the same for ultrathin oxides deposited at low temperature as for thermodynamically stable thicker oxides. Moreover, post-deposition anneals (PDA), required for device processing, can profoundly alter interfacial structure and band offsets, potentially affecting the electronic properties of the insulator. For these reasons, reliable characterization of interface band alignment for a wide range of oxide thicknesses and annealing treatments is needed.

In the work presented in Chapter 3, we use optical characterization of band offsets at various high-*k* dielectric/semiconductor interfaces using linear internal photoemission (IPE), combined with direct detection of DC photocurrent from a biased metal-oxide-semiconductor (MOS) capacitor under monochromatic illumination, and IMPE, combined with detection of internal space charge fields by EFISH [13] generation. IPE has been the standard method for determining relative electron energy states at solid-solid interfaces for more than 40 years [14]. The oxide (or "collector") must have high dielectric quality and must be sufficiently thick (typically ~10 nm or more) to suppress background leakage current under bias. Because of leakage currents, S/N ratio rapidly degrades for oxides thinner than ~10 nm, which are increasingly prevalent in modern devices. On the other hand, IMPE-EFISH is well suited for characterizing sub-10 nm oxides. Since no bias is applied and no current detected, leakage currents are not an issue. Moreover, no device fabrication is required. Instead charge injected across the oxide barrier by multi-photon absorption is probed in the as-grown Si/oxide structures by EFISH [13] generation, which detects the DC field that develops across the interface as injected charges are trapped at the free oxide surface [15-20]. Because diffusion of photo-injected carriers *without* bias becomes inefficient for thick oxides, IMPE-EFISH is

generally restricted to oxides *thinner* than ~ 10 nm [15]. Thus IPE and IMPE-SHG complement each other. Previous studies have investigated either IPE or IMPE-EFISH separately. As part of the study presented in Chapter 3, we applied both methods to similar samples, enabling direct comparison of the complementary results.

However as the device performances are pushed further forward, some fundamental limits of Si will still obstruct the scaling. Thus both electronic industry and academia are currently experimenting with many new semiconductor materials for postsilicon technology. III-V compound semiconductors have once again drawn great attention mainly because of the two recent developments in the integrated circuit (IC) industry. First, the native thermal silicon oxide has been replaced by high-k dielectrics in the mainstream Si IC manufacturing, which means that the key material advantage of silicon has disappeared. This strongly motivates the integration of III-V semiconductors with their superior carrier mobility and optical properties. Second, the increased gate capacitance corresponding to the aggressive scaling relaxes some of the requirements on interface trap density D_{it}. Transistors now can still function very well even though D_{it} is at high levels previously considered unacceptable. One promising approach to III-V compound semiconductor is hetero-epitaxial growth on Si substrates, because this hetero-epitaxy system could potentially yield a highly optimized overall system by combining the superior individual properties of the constituent materials: high mobility and unique optical properties of compound semiconductor; the excellent mechanical and thermal properties of Si as listed in Table 1, especially the much lower cost for larger size Si wafer. Although the cost for epitaxial growth is expensive, since the regrowth of epilayer is inevitable for device applications based on III-V semiconductors, the extra effort involved in this initial growth of epilayer is insignificant.

	Electron mobility (cm^2/V-s)	Direct bandgap	thermal conductivity (W/cm-^oC)	Modulus (dyn/cm^2)
Si	1300	No	1.3	9.8×10^{11}
GaAs	8500	Yes	0.55	7.5×10^{11}

Table 1: Comparison of physical properties of Si and GaAs.

This hetero-epitaxy system has already successfully led to monolithic integration of electro-optic devices with interchip Si based signal processing elements, high power/weight ratio solar cells for space application and electronic devices with comparable or even better performance compared than their homo-epitaxial counterparts [21-28]. Nevertheless, high defect density in the polar epi-films continues to limit the performance of such devices. In addition to the threaded dislocations (TDs) that can propagate from any hetero-interface in the presence of a large lattice mismatch, polar-on-nonpolar hetero-epitaxial films are uniquely susceptible to formation of anti-phase domains (APDs) because of the unavoidable presence of single-atomic-height steps at the (001) surface of elemental semiconductors. Because of these steps, the locations of cation and anion interchange in neighboring APDs, resulting in undesirable Ga-Ga and/or As-As

bonds at the anti-phase boundaries (APBs). The APBs can propagate through the epilayer and degrade device performance by serving as strong scattering centers for carriers.[29, 30] APB density can be reduced by mis-orienting the substrate, rendering double-atomic-height steps energetically favorable,[4] although competing defects can then increase in density. To evaluate this and other strategies for reducing APB density, a need exists for fast, non-invasive methods of detecting APBs that distinguish them from other type of defects.

In the work presented in Chapter 4, we use optical SHG to characterize APBs, exploiting the selective sensitivity of 2nd order nonlinear optical susceptibility to the reversed sublattice symmetry between different domains. This results in 1000 times degradation of the SH intensity compared to a homo-epitaxial GaAs control sample. The results show that SHG can identify APBs quickly and non-invasively for advanced MOSFET device applications compared to defect selective etching and transmission electron microscopy (TEM) techniques.

All the above mentioned scaling strategies are focused on the enhancement of device performance by reduction of gate delay. However, performance in a semiconductor chip also relies on several other factors: the interconnect delay at the device level; the bandwidth/legacy at the die level. As the scaling continues, the conventional 2D back-end-of-line wiring design imposes significant challenges to the chip performance and power consumption due to the difficulty of corresponding operation voltage scaling, since the *RC* delay (signal propagation time between transistors) related to the metal wire resistance (*R*) and interlevel dielectric capacitance (*C*) becomes dominant for deep sub-micron devices. One possible way to solve all these obstacles is 3D integration --- *i.e.* connecting vertically stacked chips to achieve much higher package form factor, smaller inter-chip RC delay as well as power consumption

due to the shorter interconnect line length. The through-silicon via (TSV) is a promising 3D integration layout that can provide the highest energy and space efficiency. However the thermal-mechanical reliability has become a big concern for the implementation of TSV, because of dissimilar coefficient of thermal expansion (CTE). The thermal stress induced during the processing of TSV fabrication can induce detrimental effects on the performance and reliability of devices, for example, degradation of mobility of transistors within the strain field, debonding/lamination at the interface between metal wire and Si wafer, voiding formation within the metal interconnect line, and even cracking of Si wafer under severe strain. Thus this situation urges implementation of physically reliable and especially *in-situ* characterization of process induced strain.

In the work presented in Chapter 5, we show preliminary SHG imaging results to characterize the strain distribution around TSV patterns.

1.2 OUTLINE

This dissertation aims to prove that SHG is a powerful metrology for advanced semiconductor material systems of current market relevance. Its ability to identify and characterize specific dielectric and structural defects distinguishes SHG as a potential in-line, non-invasive diagnostic for advanced device applications.

Chapter 2 presents the study of SOI by SHG. It focuses on characterizing process-induced structural defects at the buried SOI/BOX interface by both amplitude- and phase-sensitive SHG measurement, which is critical to extracting charge trapping kinetics.

Chapter 3 covers the band alignment study of the interface between high-k dielectrics and semiconductor substrates by complementary methods: linear IPE and IMPE. Post-deposition anneal (PDA) effects on band offsets are also discussed.

Chapter 4 demonstrates the detection of APB defects on the top surface of epitaxial GaAs grown on elemental semiconductor substrates. Scanning SH microscopy is also used to map the spatial distribution of APB defects on various hetero-epitaxy systems.

Chapter 5 presents a preliminary study of strain field distribution by scanning SHG imaging.

Chapter 6 summarizes the various applications of optical SHG in characterizing novel materials for state-of-art advanced MOSFET technology, and suggests directions the future work.

Chapter 2: STUDY OF ULTRATHIN SOI BY SHG

SOI structures consisting of a single crystalline Si film separated by a buried oxide (BOX) layer from a bulk Si substrate provide a flexible platform for modern ultra large scale integrated (ULSI) circuits with better device isolation, speed, density and scalability than bulk Si circuits [3]. As devices scale down to deep submicrometer dimensions, SOI-based architectures with ultrathin (<10 nm) Si films have drawn increasing attention because of their high carrier mobility, low power consumption, and low vulnerability to short-channel and parasitic MOS effects.[3] The first half of this chapter discusses the study of ultrathin SOI wafers by time-independent SHG, with focus on rotational anisotropy. The second half presents amplitude- and phase-sensitive time-dependent SHG from ultrathin SOI samples in order to non-invasively characterize the process-induced structural defects within the crystalline Si films.

2.1 PHENOMENOLOGICAL MODEL OF TIME-INDEPENDENT SHG FROM SOI STRUCTURE

The lowest order SHG from centrosymmetric nonlinear crystals, like Si, includes two parts: the dipolar response from the interface where inversion symmetry is broken, and the non-local quadrupolar response from the bulk. SOI structures, consisting of a single crystalline Si film separated by a BOX layer from a bulk Si substrate provide a model system for studying SHG from various multi-layer structures. Since multi-layer structures are prevalent in advanced microelectronics, we first develop a phenomenological theory of SHG from them in some detail. For this multi-layered structure, the major challenge to describing SHG analytically comes from multiple reflections at internal interfaces. The solution can be obtained following three steps:

1. Construct the total fundamental field within the Si layer after multiple inernal reflections;
2. Calculate SHG produced from the above fundamental field;
3. Calculate total output SHG from the above source after multiple reflections.

Step 1 and 3 are only linear optic processes, which can be solved by a transfer matrix technique [31]. For the second step, the phenomenological model developed in reference [32] is used to describe the SHG response from interface and bulk sources. A unique feature of this model is the spatial separation of the excitation field and the SH polarization density

$$P_i^{(2\omega)}(z) = \sum_{j,k} \chi_{ijk}^{(2)} E_j(z_0^-) E_k(z_0^-) \delta(z - z_0^+) \ , \qquad (2)$$

for the localized surface dipole response, where z_0 is the location of interface, as indicated in Figure 2, $z_0^{\pm} = z_0 \pm \varepsilon \ (\varepsilon \to 0)$.

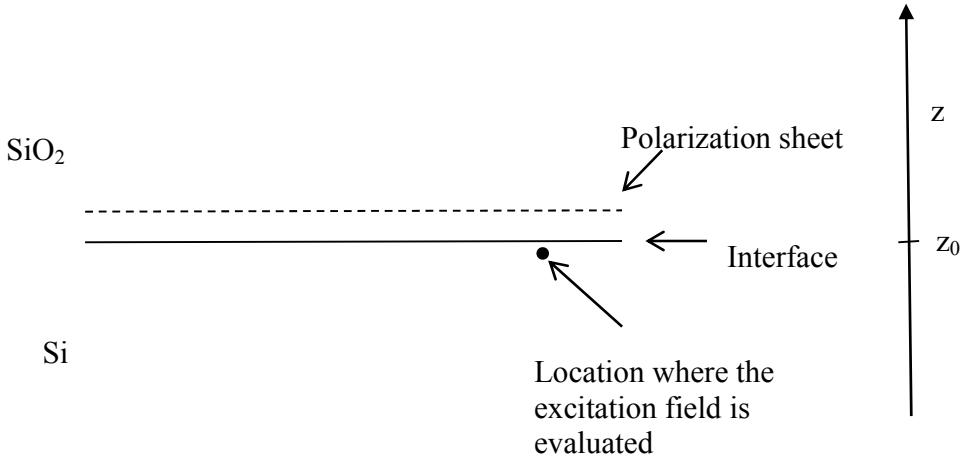

Figure 2: Phenomenological model for SHG at localized interfacial source.

The reason the localized SH source is treated this way is the ambiguity when considering the conventional boundary condition at an interface as presented in Figure 3:

$$E_T^{(2\omega)} \propto \frac{-4\pi P}{\varepsilon(2\omega)-\varepsilon(\omega)} \propto P$$

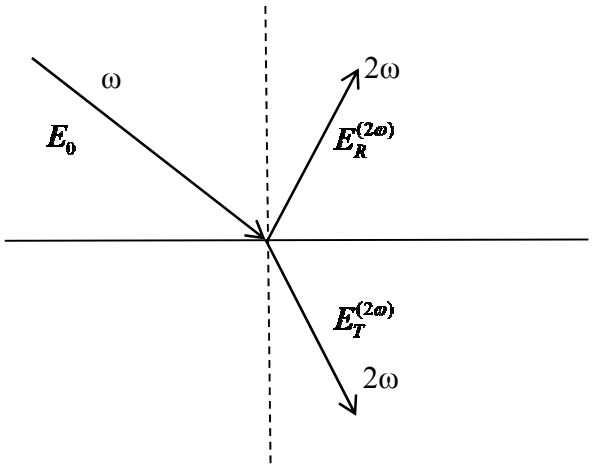

Figure 3: The boundary condition for reflected and transmitted SHG at interface

A polarization density localized at the interface cannot satisfy this boundary condition, and thus cannot generate propagating SH radiation. So the polarization density and excitation field are infinitesimally displaced away as described in Equation (2) in order to solve this ambiguity by separating SHG from the boundary condition.

The total SHG from this complex multi-layer structure can be obtained following three steps. The detailed derivation can be found in Appendix A. Here we only list the final results, and some conventions for the notations used in the above results:

1. any lower case letter represents a physical quantity of the fundamental wave (ω), a capital letter of the SH wave (2ω);
2. subscript 1 indicates that the physical quantity is evaluated inside SiO_2, subscript 2 in Si, and subscript 0 in air;
3. a superscript represents polarization state;

4. for convenience, different media domains are named o, a, b, c, d as listed in Figure 4.

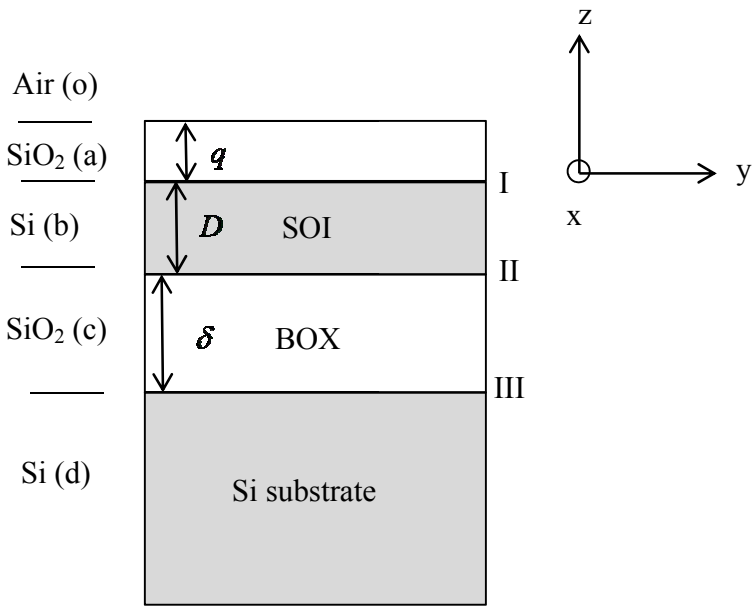

Figure 4: Geometric layout for the cross section of SOI structure.

Thus r_{bd}^{p} denotes the total reflectivity from an effective interface formed by *b*-*c*-*d* layer for *p*-polarized fundamental wave. The total SHG from this SOI structure is composed of the SH radiation from each interface as well as Si bulks (including SOI film and substrate):

$$E_{Total}^{p} = E_{I}^{p} + E_{II}^{p} + E_{III}^{p} + E_{SOI}^{p} + E_{sub}^{p}, \tag{3}$$

where the analytic solution for each term is derived in Appendix A. Thus the azimuthal angle-dependent SHG intensity can be written as:

$$I^{(2\omega)}(\phi) = \left|a + b\cos 4\phi\right|^{2}, \tag{4}$$

where *b* is chosen to be real and positive, so a is in general a complex number.

2.2 EXPERIMENTAL PROCEDURE

Commercial grade plasma-activated bonded (PAB) (Ref. 34) (100) SOI wafers with initial p-type (lightly B doped) SOI layers of thickness t_{SOI} ~ 50 nm separated from the Si(100) substrate by a BOX of nominal thickness t_{BOX} ~ 160 nm are used as starting material. In order to obtain ultrathin SOI layers of various thickness, the starting wafer was thermally oxidized for different times and the thermal oxide was stripped away by buffered oxide etch (BOE) to reduce t_{SOI} to ~10, 7, 4 and 2 nm with native oxide (NOX) on top. Precise layer thicknesses measured by spectroscopic ellipsometry (SE) are shown in Table 2. Three extra subsets of reference samples were then fabricated as follows: (1) a ~70 nm oxide was deposited (hereafter DOX ≡ deposited oxide) on top of one subset by plasma-enhanced chemical vapor deposition to suppress carrier trapping at the free surface by making the resultant oxide thickness larger than the scattering length of electrons in the oxide [15]; (2) the SOI layer of another subset was selectively etched away by tetramethylammonium hydroxide (TMAH) (25% WT) solution at 85 ^{o}C to expose the SOI/BOX interface for rms roughness measurement by atomic force microscopy (less than 0.4 nm for all SOI thicknesses) and for direct SHG probing without the SOI layer; (3) the last subset was dipped into HF (50%) solution for 5min to reveal HF defects [35].

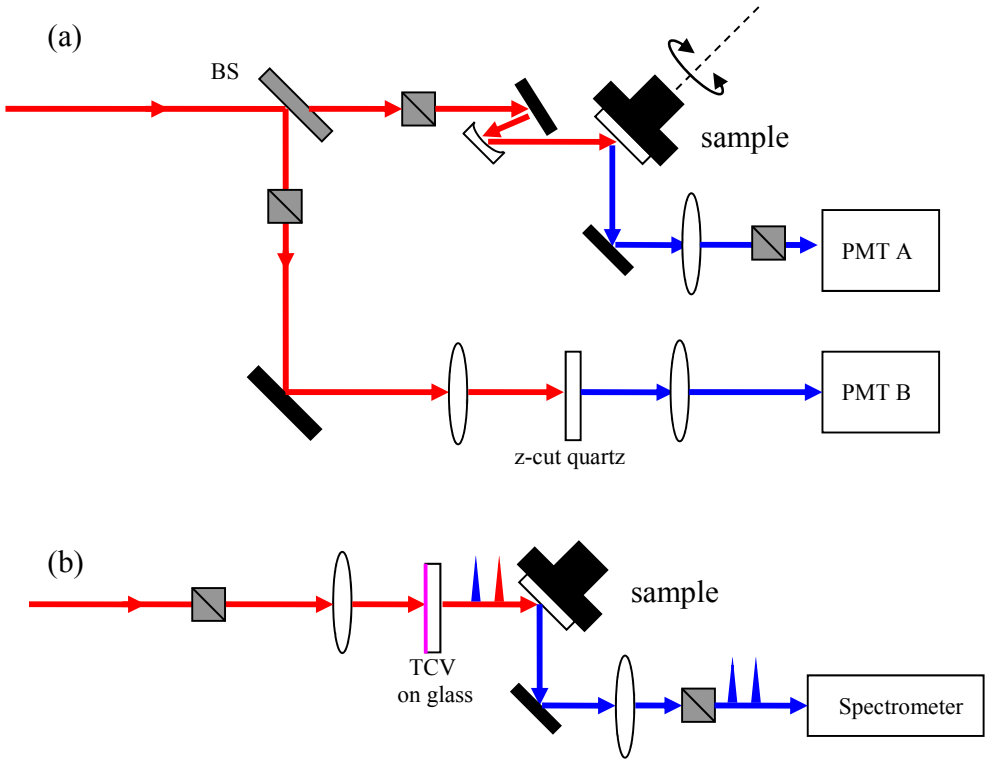

Figure 5: Schematic experiment setup for SHG intensity measurement (a) and phase measurement by FDISH (b).

Figure 5 shows the experimental setup for SHG. P-polarized optical pulses (~150 fs, 150 mW-300 mW average power, 76 MHz repetition rate) from a 10W Verdi-pumped Ti:sapphire oscillator with wavelength λ tunable over the range 710 nm~840 nm were focused at 45^{o} incident angle to a ~30 μm diameter spot on the sample mounted on an azimuthal rotational stage to acquire rotationally anisotropic (RA)-SHG. Reflected p-polarized SHG signal was detected by a photomultiplier tube and normalized over the reference SHG from a z-cut quartz crystal in order to eliminate the signal variation due to laser power fluctuation. The TD-SHG was taken at the azimuthal angle corresponding to a maximum of RA-SHG. The optical phase of reflected SH radiation was measured by a

frequency-domain interferometric second-harmonic (FDISH) technique,[36], using a temporally delayed reference SH pulse generated in a poled tri-cyano-vinylaniline(TCV) film coated on a glass slide [37].

Materials	t_{NOX} (Å)	t_{SOI} (Å)	t_{BOX} (Å)
2 nm SOI	24.12±0.52	25.46±0.04	1609.86±0.49
4 nm SOI	25.10±0.35	34.08±0.04	1618.02±0.38
7 nm SOI	24.93±0.16	67.82±0.05	1610.97±0.28
10 nm SOI	24.92±0.13	104.83±0.06	1597.71±0.39
50 nm SOI	24.45±0.20	473.22±0.13	1626.21±0.72

Table 2: NOX, SOI and BOX film thicknesses measured by SE.

2.3 EXPERIMENTAL RESULTS AND DISCUSSION

2.3.1 Time-independent SHG results

From the phenomenological model in Section 2.1, the SOI structure exhibits three Si/SiO_2 interfaces I thru III which contribute azimuthally isotropic interfacial dipole SH radiation, while the bulk of the SOI film and Si substrate produce 4-fold anisotropic

quadrupolar SHG. The resultant azimuthal-angle-dependent SH intensity was expressed by Equation (4). RA-SHG results from all SOI samples are listed in Figure 6(a)-(d).

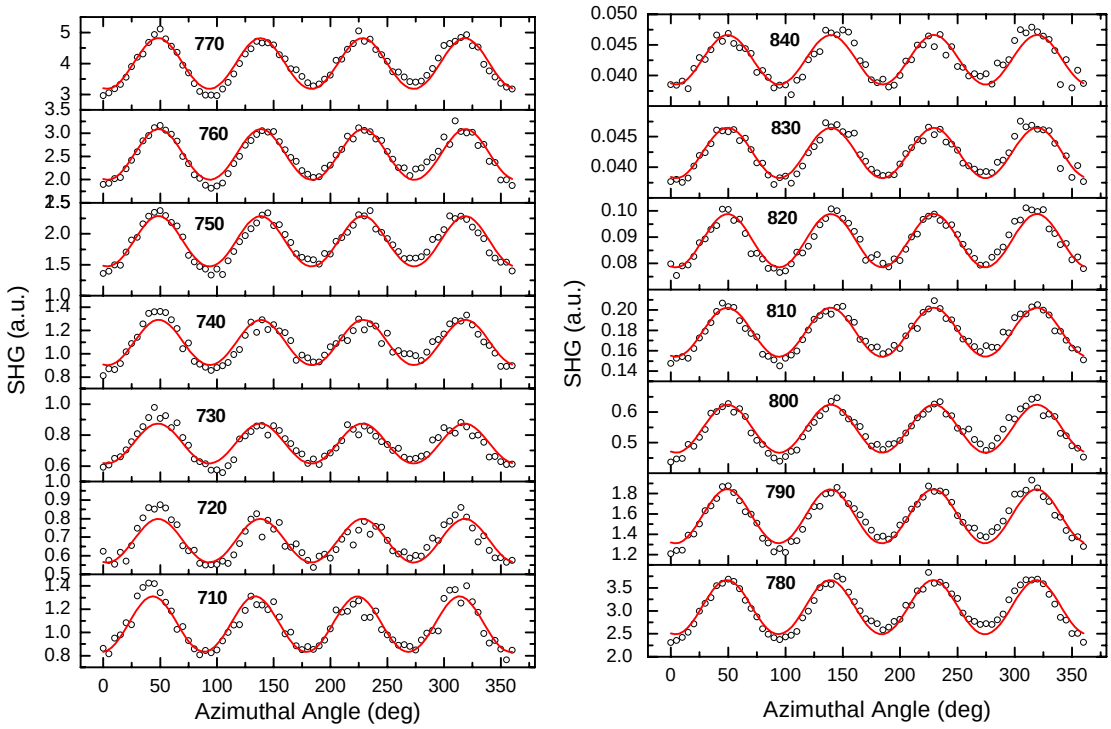

Figure 6(a): RA-SHG data (empty circles) from 2 nm SOI with 70 nm DOX at different fundamental wavelengths (710 < λ <840 nm). The red line is the fitting curve from the phenomenological model described by Equation (4). $\phi = 0$ means incident plane is along the <100> direction.

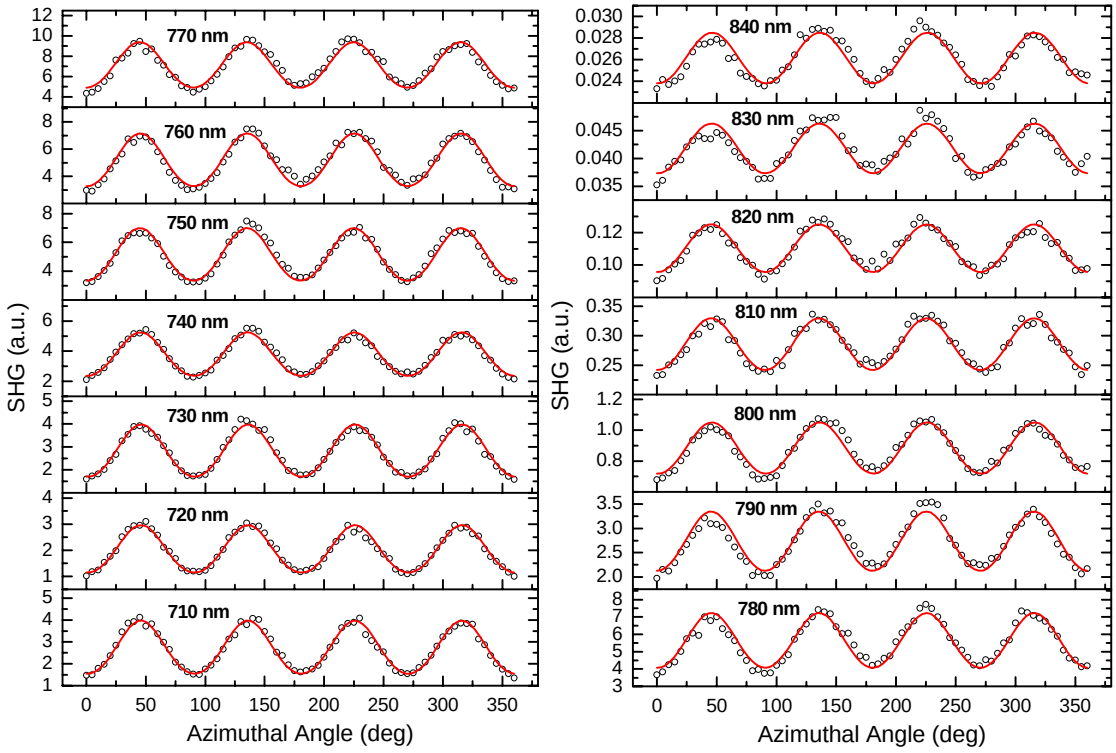

Figure 6(b): RA-SHG data (empty circles) from 4 nm SOI with 70 nm DOX at different fundamental wavelengths ($710 < \lambda < 840$ nm). The red line is the fitting curve from the phenomenological model described by Equation (4).

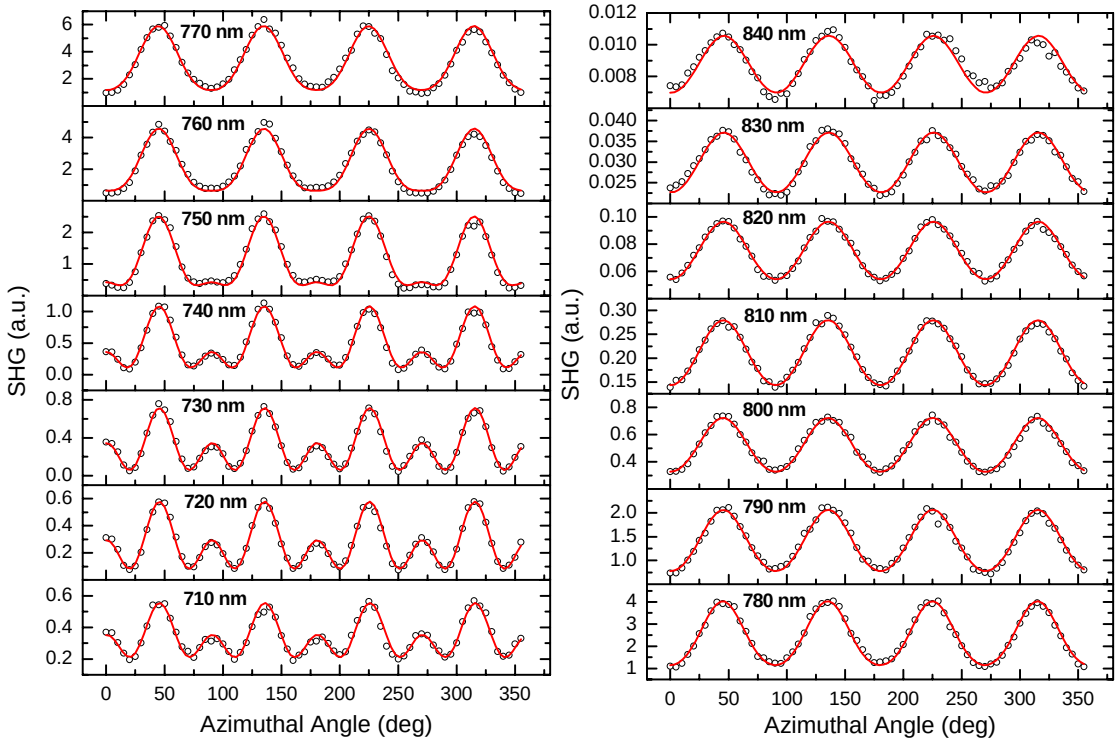

Figure 6(c): RA-SHG data (empty circles) from 7 nm SOI with 70 nm DOX at different fundamental wavelengths ($710 < \lambda < 840$ nm). The red line is the fitting curve from the phenomenological model described by Equation (4).

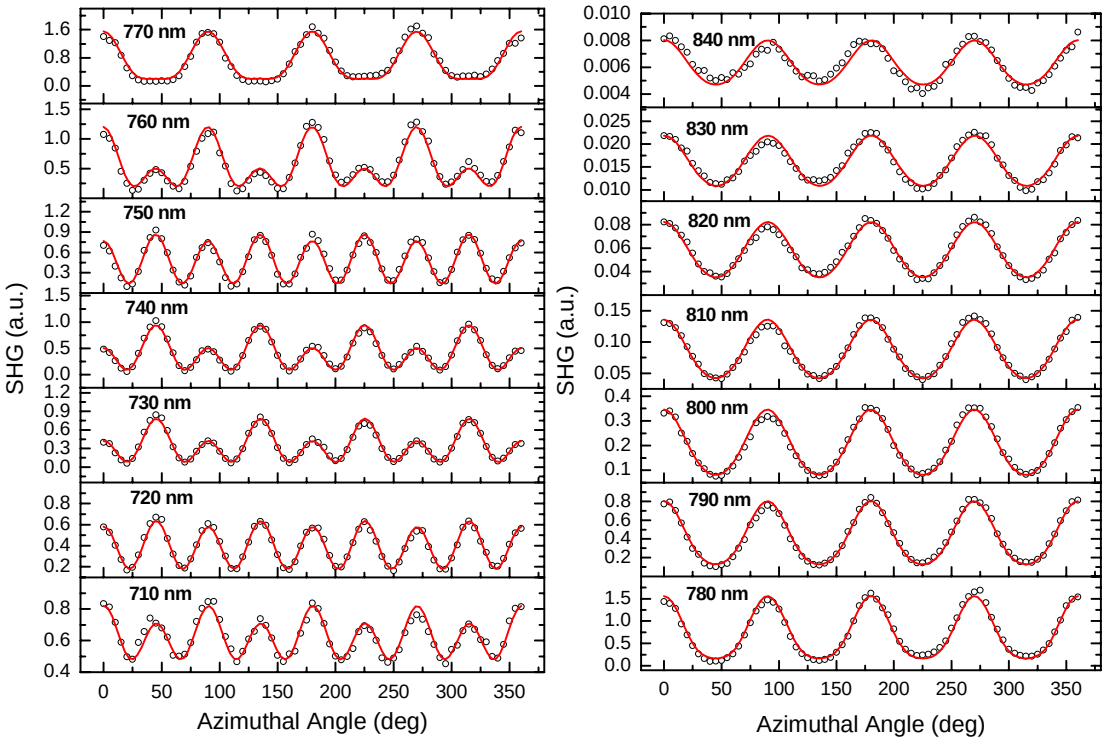

Figure 6(d): RA-SHG data (empty circles) from 10 nm SOI with 70 nm DOX at different fundamental wavelengths ($710 < \lambda < 840$ nm) The red line is the fitting curve from the phenomenological model described by Equation (4).

For this data, the incident laser focal spot was displaced slightly from the sample rotation axis, so there was no time for build-up of charge as the sample moved. All responses are consistent with the expression in Equation (4), indicating that crystallographic axes of SOI film and substrate are mutually aligned. This agrees with the X-ray diffraction pattern shown in Figure 7 taken from 50 nm SOI with NOX, where only one set of diffraction pattern can been seen from both SOI film and Si substrate.

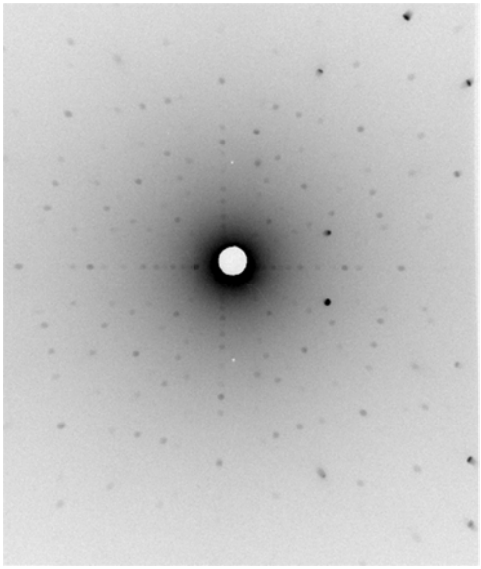

Figure 7: X-ray diffraction pattern from 50 nm SOI with NOX

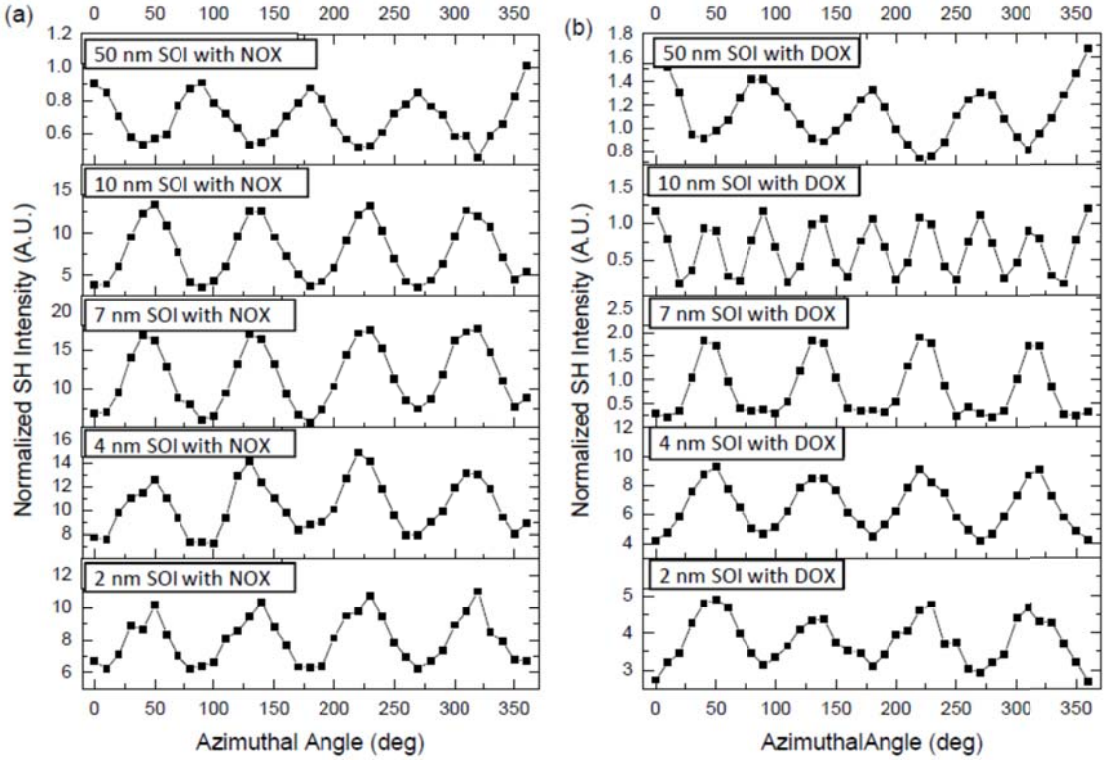

Figure 8: Anisotropic SHG with fundamental center wavelength 750 nm ($h\nu_{SH}$ = 3.3 eV) incident power 150 mW for samples with different t_{SOI}.

The variations in azimuthal anisotropy evident in Figure 8 are attributable to variations in the parameter *a*. For the 50 nm SOI samples, we observe a 4-fold oscillations on an isotropic background, with the first maximum at $\phi = 0$, which indicates the real part of *a* is also positive, *i.e. Re(a) > 0*. On the other hand, for most of the ≤ 10 nm SOI samples, we observe 4-fold oscillations with the maxima and minima reversed, indicating that *Re(a) < 0*. Uniquely for the 10 nm SOI sample with DOX, we observe 8-fold oscillations, indicating $a \approx 0$, leaving only the weak bulk quadrupolar contribution $b^2 \cos^2 4\phi$. These variations in *a* can be related qualitatively to varying relative contributions of interfaces I thru III to *a*. For the 50 nm SOI samples, the interface I makes the strongest contribution to *a*. This is because for $\lambda = 750$ nm, the absorption depth α^{-1} of SH radiation at $\lambda/2 = 375$ nm is $\alpha^{-1} = 24$ nm [38]. SH radiation generated at interfaces II and III is thus mostly absorbed. For samples with SOI layers of thickness $t_{SOI} < \alpha^{-1}$ (2nd thu 5th panels in Figure 8 (a) and (b)), on the other hand, interfaces II and III contribute strongly to *a*. A simple interpretation is that the opposite orientation of interface II with respect to interfaces I and III changes the sign of *a* when interface II dominates *a*. For the 10 nm DOX sample, the contribution of interface II to *a* evidently cancels that of interfaces I and III almost exactly. The above argument proves the validity of the model described by Equation (4).

Figure 9 present the fitted parameters |*a*| and *b* according to Equation (4) from the data shown in Figure 6 under P_{in}/P_{out} configuration. Here 'in' denotes the incident field, and 'out' represents the SH field. Thus 'P_{in}/P_{out}' indicates that the polarization state of the incident fundamental field is *p* and the measured SH field is also *p*-polarized. The blue shift of |*a*| may be an indication of quantum confinement effect and the red shift of b may be due to the in-plane compressive stress within the Si films.

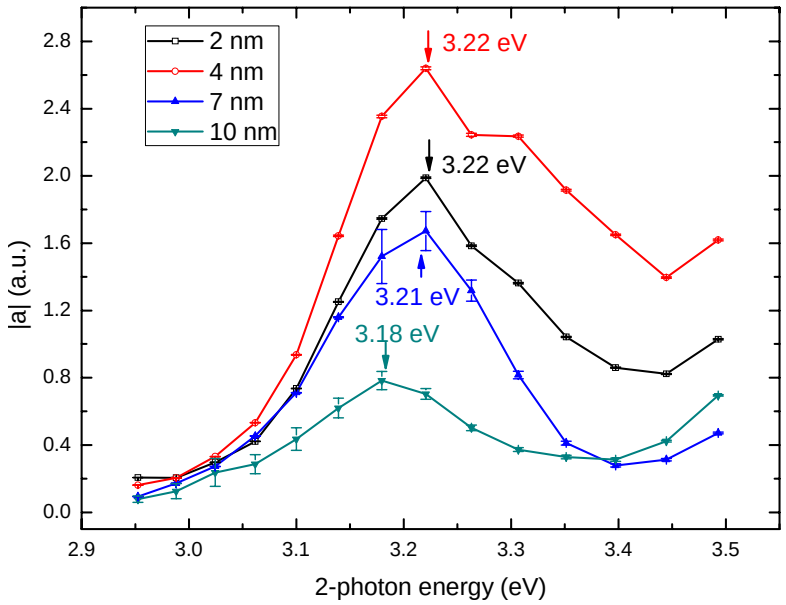

Figure 9(a): Spectra of $|a|$ from samples with different SOI thickness

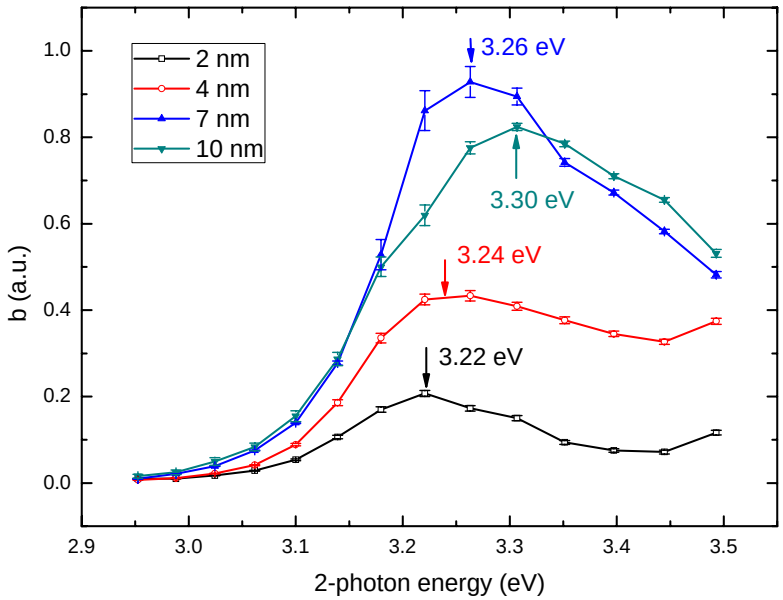

Figure 9(b): Spectra of b from samples with different SOI thickness

2.3.1 Time-dependent SHG results

As mentioned before, the absorption depth of SH radiation at $\lambda/2 = 375$ nm is $\alpha^{-1} = 24$ nm, so for ultrathin SOI charge injection at all three Si/SiO_2 interfaces could be measurable by SHG. TD-SHG data are not affected by preirradiating the photo-excited spot with a continuous-wave laser of the same fluence, ruling out a thermal origin of the dynamical behavior. For the sample with no SOI layer [top panel in Figure 10(b)], negligible time-dependence is observed indicating negligible charge injection at the substrate/BOX interface, in contrast to the results of Ref. 5. The time dependence in the previous study may have come from trapping sites created during wet bonding, [39] whereas PAB performed at low temperature creates fewer defects at both substrate/BOX and SOI/BOX interfaces. Upon initial irradiation, all ultrathin SOI samples with NOX exhibit similar TD-SHG behavior shown in Figure 10(a): an initial rise followed by a subsequent decay. After blocking the laser for a few min or wiping the surface with methanol, a repeat scan on the same spot yields only a rising TD-EFISH signal [Figure 11(a) red data]. This behavior is explained by competition between the two optical HCI processes shown in Figure 12. Rising SHG comes from electrostatic field $E_1(t)$ built up by electrons injected from SOI into the NOX conduction band (CB) via three-photon absorption, initiating their diffusion to surface trap sites catalyzed by ambient oxygen.[15] The decay results from oppositely directed electrostatic field $E_2(t)$ established by injecting electrons from SOI into BOX traps. Since the latter are long lived and not removed by surface wiping, re-growth of $E_1(t)$ by free surface charging dominates the repeat scan. This interpretation is confirmed by samples with DOX, which, because charge trapping at the free surface is suppressed, exhibit only a falling TD-EFISH signal that reflects SOI/BOX charge dynamics alone [bottom 4 panels of Figure 10(b)].Thus charge injection at the SOI/BOX interface is isolated for samples with DOX.

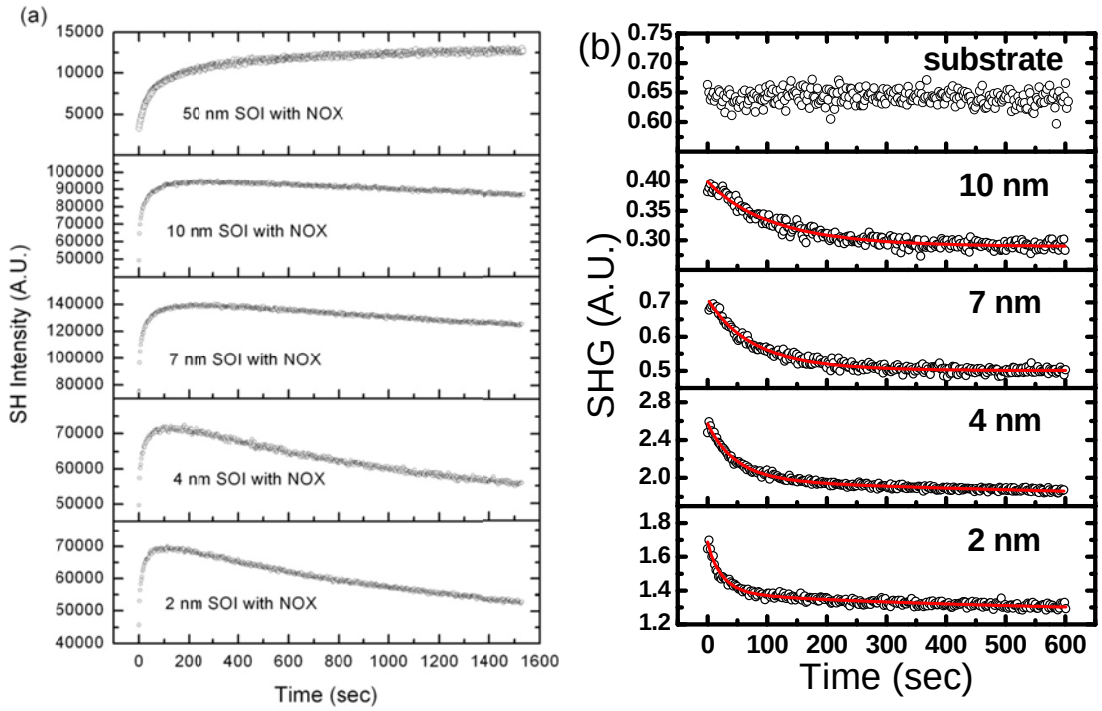

Figure 10: TD-SHG data (open black circle) and fitting (red curves) SOI samples with NOX(a) and DOX(b) with fundamental center wavelength 750 nm incident laser power 200 mW. Substrate is fabricated by stripping the top SOI layer using TMAH from 2 nm SOI leaving a bulk Si and ~160 nm oxide on top.

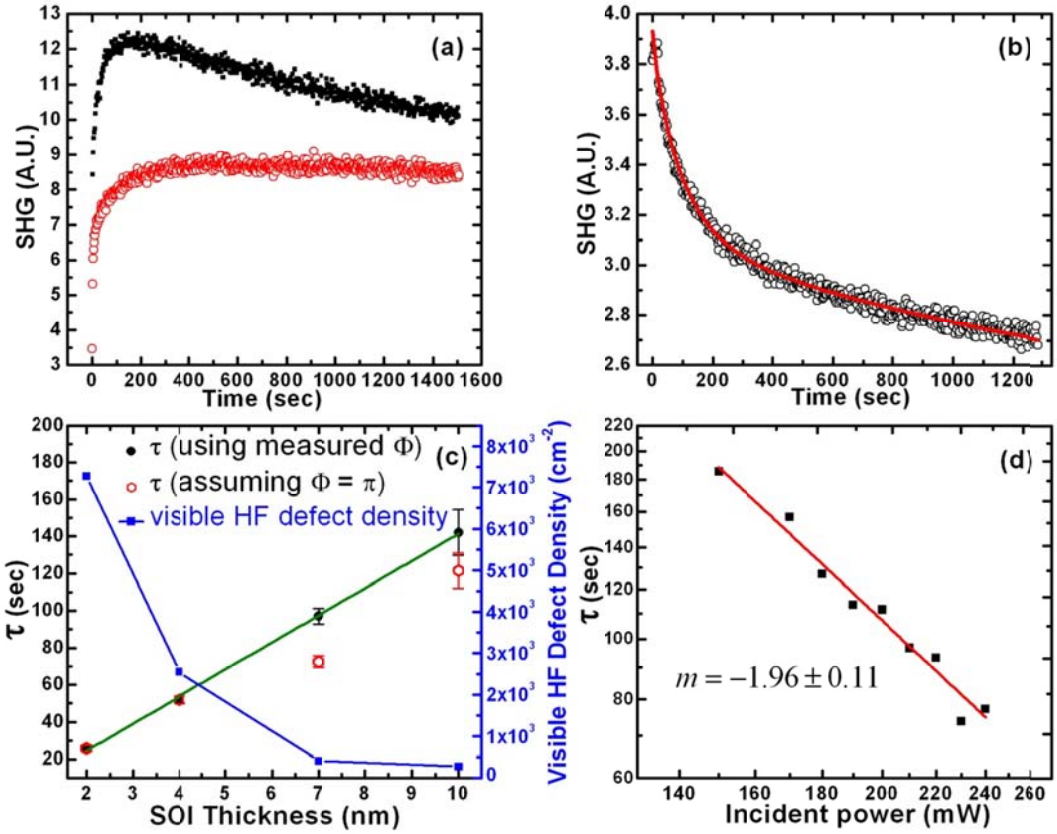

Figure 11: (a) Comparison of TD-SHG from 2 nm SOI with NOX (filled black square) with that after wiping the free surface or blocking the laser for a few minutes (empty red circle). (b) Fitting of the data (black circles) according to Eq. (2) (red curves) for 4 nm SOI with DOX at incident laser power 150 mW. (c) Scaling of time constant and visible HF defect density with t_{SOI}. (d) Laser power dependence of time constant from the TD-SHG data for 4 nm SOI with DOX.

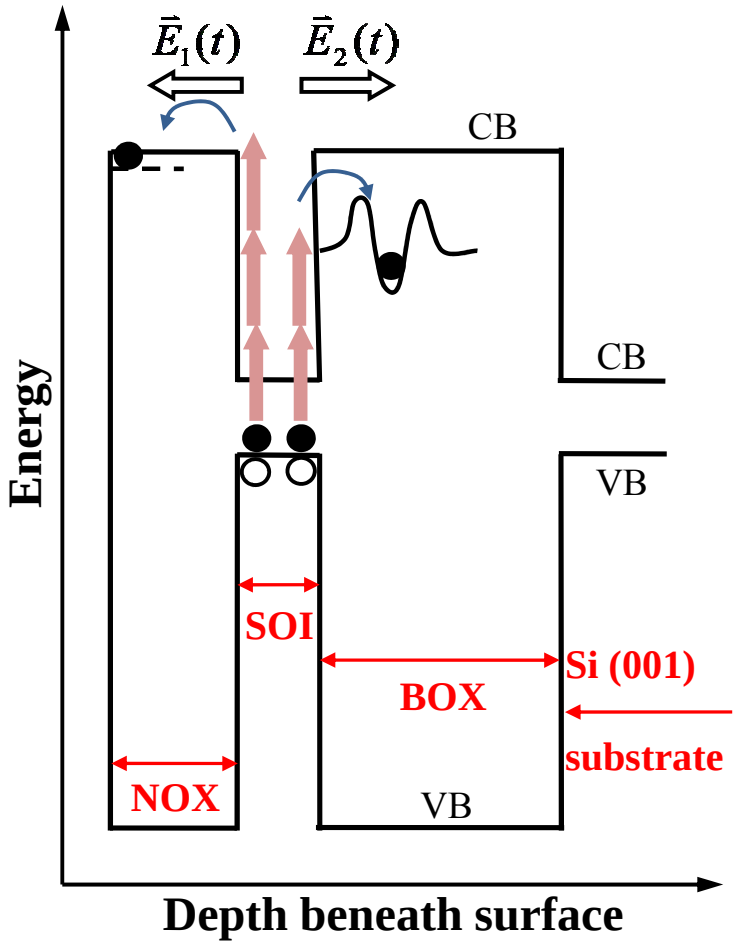

Figure 12: Schematic diagram of CB and VB edges of SOI with NOX (band bending is neglected), showing competing multi-photon HCI processes.

Quantitative investigation of the isolated TD-EFISH data indicates a two-stage decay before saturation, as shown in Fig. 11(b) for t_{SOI} = 4 nm. Electrostatic field growth which is proportional to charge density *n(t)* by HCI before saturation can be modeled by:

$$E_2(t) \propto n(t) = \alpha_1 \times (1 - e^{-t/\tau}) + \alpha_2 \times t^n , \qquad (5)$$

where the first term represents the initial fast filling of preexisting trap sites (with strength factor α_1) and the second term denotes much slower creation of new interface

traps (with strength factor α_2) by energetic carriers created by photo-excitation and/or Auger recombination. The generation rate of those traps is presumed much smaller than their charge filling rate. TD-SHG intensity $I^{(2\omega)}(t)$ then takes the form:

$$I^{2\omega}(t) \propto \left|\chi^{(2)} + \chi^{(3)}E^{DC}(t)\right|^2 \propto \left|p_0 + (1 - e^{-t/\tau} + f \times t^n)e^{i\Phi}\right|^2, \quad (6)$$

where p_0 represents the time-independent contribution, chosen to be real, f is a relative strength factor and Φ is the relative phase of the time-dependent terms, which is measured by FDISH. The power index n of the last term of Equation (6) obtained from the fitting [see *e.g.* red curve in Figure 10(b) and 11(b)] varies between 0.43 and 0.56, consistent with low gate voltage stressed electrical measurements based on metal-oxide-semiconductor field-effect transistor [4], the closest electrical analog of optical HCI measurements. For small t, we can neglect HCI-induced trap generation to simplify the analysis and fitting, and Equation (6) reduces to

$$I^{2\omega}(t) \propto \left|p_0 + (1 - e^{-t/\tau})e^{i\Phi}\right|^2 \quad (7).$$

General TD-EFISH can be described by a phasor diagram as in Figure 13, where $\widetilde{\mathrm{P}}_0$ and $\widetilde{p}(t)$ represent complex time-independent and time-dependent SH polarization densities, and correspond to the first and second terms, respectively, inside the absolute value bracket in Equation (7). The dynamics of interest is contained in the amplitude $\widetilde{p}(t)$, which increases with time while maintaining phase angle Φ, here assumed constant in time, with respect to $\widetilde{p}(t)$. SH intensity $I^{2\omega}(t) \propto \left|\widetilde{\mathrm{P}}(t)\right|^2 = \left|\widetilde{\mathrm{P}}_0 + \widetilde{p}(t)\right|^2$ alone is insufficient to retrieve the time-dependent polarization density $\widetilde{p}(t)$ because of the unknown phase angle Φ as indicated in Figure 13. Thus an FDISH measurement was employed to extract the phase by fast Fourier transform [40]. Figure 14(a) and (b) show the FDISH interferograms and extracted phase angles Φ corresponding to the SOI samples with DOX in Figure 10(b).

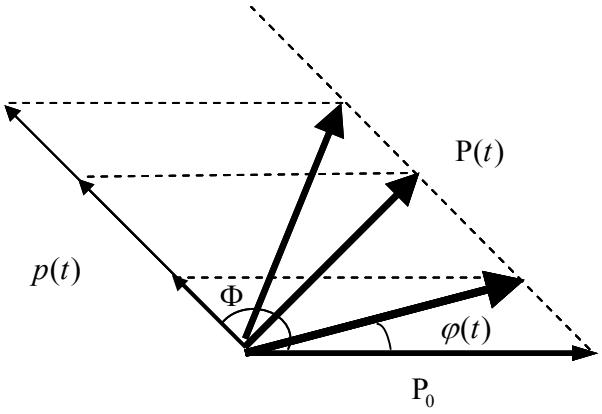

Figure 13: Phasor diagram of time dependent behavior for thin SOI samples with DOX.

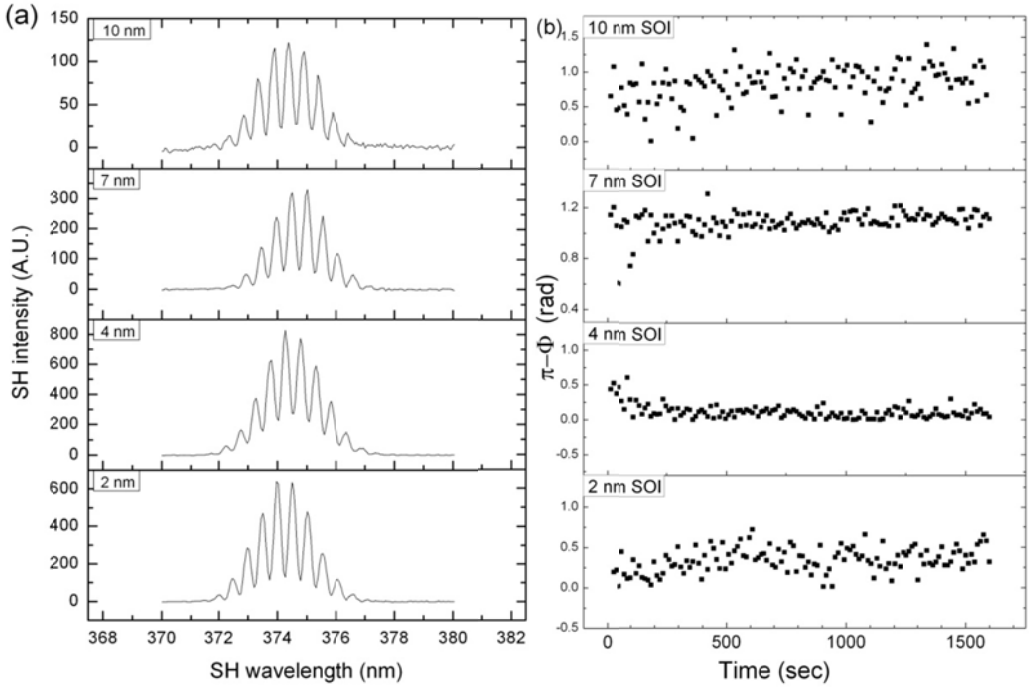

Figure 14: Interferogram patterns at t=0 (a) and extracted phase angles (b) for thin SOI samples with DOX.

FDISH measurements yield constant phase angles $\pi - \Phi \sim 0.32 \pm 0.22$, 0.11 ± 0.18, 1.08 ± 0.13 and 0.79 ± 0.34 rad respectively for 2, 4, 7 and 10 nm SOI with DOX. With these Φ the TD-SHG data for small t of samples with DOX measured under identical conditions were fitted using Equation (7). The fitted time constants τ, plotted as black data points in Figure 11(c), scale almost exactly linearly with SOI thickness [green curve in Figure 11(c)]. Accurate measurement of Φ was essential to establishing the linear relationship between τ and t_{SOI}. If we neglect the variation of Φ with t_{SOI} (*e.g.* by assuming $\Phi = \pi$ for all samples), a nonlinear relationship [*e.g.* red data points in Figure 11(c)] invariably results.

The linear relationship suggests that the initial fast exponential trapping is associated with defects formed during thermal oxidation thinning of the SOI [35], the duration of which is the only difference among these samples. During thermal oxidation, structural defects (such as Si vacancies and O precipitates) are created at the external Si/SiO_2 interface, then gettered near the SOI/BOX interface.[35] The density of these defects can be approximated as $N(t_{SOI}) \approx \eta(D - t_{SOI}) + N_0$, where N_0 is the intrinsic defect density, D the starting SOI thickness and η the density of defects created per unit thickness of Si consumed. Carrier trapping rate $1/\tau$ is proportional to trap density $N(t_{SOI})$ at the SOI/BOX interface: $1/\tau \propto N(t_{SOI})$. Thus we obtain the linear relationship $\tau \propto \frac{1}{N_0 + \eta D - \eta t_{SOI}} \approx \frac{1}{N_0 + \eta D} \times (1 + \frac{\eta t_{SOI}}{N_0 + \eta D})$ when ηt_{SOI} is much smaller than the other terms in the denominator, which is reasonable for ultrathin SOI.

To confirm the $N(t_{SOI})$ relation qualitatively, we revealed a portion of the SOI/BOX interface defects by HF dipping.[35] Defects larger than t_{SOI} provide a channel for HF penetration, resulting in an etched BOX region large enough to be observed under an optical microscope,[35] as shown in Figure 15. Scanning electron microscope images

shown in Figure 16 reveal the pinhole shape defects topology after HF soaking in the SOI layer, as reported previously.[35] A plot of *visible* HF defect density $N_{VIS}(t_{SOI})$ [Figure 11(c), blue squares] derived from the images in Figure 15 shows that N_{VIS} increases super-linearly with decreasing t_{SOI}. This is consistent with a linear increase in $N(t_{SOI})$ combined with increasing defect visibility as t_{SOI} decreases.

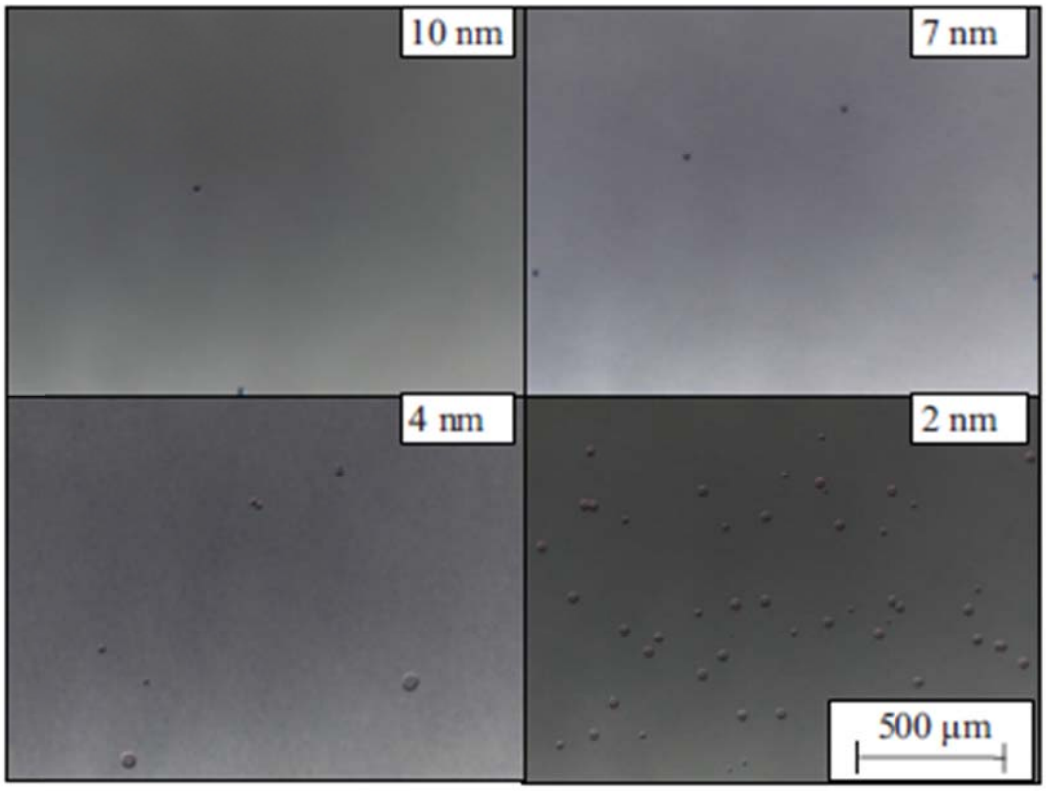

Figure 15: Optical microscope images of HF defects from samples with different SOI thickness after HF soaking.

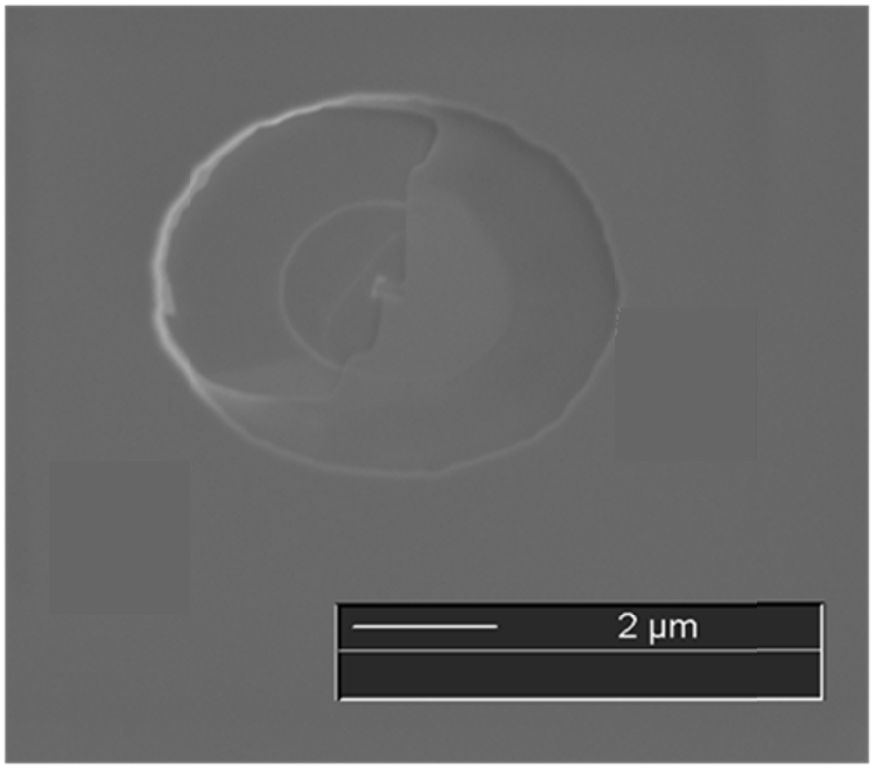

Figure 16: SEM micrograph show surface morphology of HF defects after HF soaking.

We measured the dependence of trapping rate τ^{-1} on incident laser intensity $I^{(\omega)}$ to gain insight into the energy level of the trapping states relative to SiO_2 band edges. Results for t_{SOI} = 4 nm, shown in Figure 11(d), yield a quadratic power-law dependence $\tau^{-1} \propto (I^{(\omega)})^{1.96\pm0.11}$ that suggests two-photon absorption initiates the trapping process at the the SOI/BOX interface. A similar dependence is found for other t_{SOI}. For electrons two-photon-excited from near the Si valence band (VB), this places the trap level roughly 1 eV below SiO_2 CB edge as shown in Figure 11, much deeper than ambient-oxygen-catalyzed traps at the free oxide surface, which are accessed by three-photon excitation

and lie close to the SiO_2 CB edge. This contrast may explain the much longer lifetime of the SOI/BOX traps compared to surface traps revealed by the hysteresis behavior in Figure 11(a).

2.4 SUMMARY

In this chapter, we have derived a phenomenological model for time-independent SHG from SOI structure and explained the experimental observations based on this model. Additionally, in order to study charge injection at a specific interface, we have isolated the trapping dynamics of optically excited carriers at the buried Si/SiO_2 interface of ultrathin SOI layers, and measured their variation with SOI thickness and laser intensity. The results reveal that the dominant trapping sites are induced by thermal oxidation thinning of the SOI layer, and are thus denser for thinner films. The energy level of these trapping sites lie at least 1 eV below the SiO_2 CB edge, and are thus long lived. The results demonstrate that SHG can noninvasively characterize defects critical to SOI device performance without device fabrication, and far more efficiently than decorative etching techniques, to reveal process-induced structural defects.

Chapter 3: STUDY OF BAND OFFSETS BETWEEN HIGH-*k* DIELECTRICS AND SEMICONDUCTORS BY LINEAR AND NONLINEAR INTERNAL PHOTONEMISSION

The replacement of the conventional native thermal oxide by the deposited high-*k* dielectrics has enabled the scalability of gate insulator for effective oxide thickness smaller than 1 nm. In addition to the requirement on dielectric constant and thermal compatibility with Si substrate, the band offsets (conduction band offset and valance band offset) should also be considered together due to the exponential influence of this barrier height on the thermionic emission leakage current. In this chapter, we present measurements of conduction band offsets of three high-*k* dielectrics on Si(001) substrates using linear internal photoemission (IPE), detected by measuring photocurrent from a biased MOS capacitor, and internal multi-photon photoemission (IMPE), detected by SHG. Post deposition annealing effects on the band alignment will also be demonstrated.

3.1 PRINCIPLES OF INTERNAL PHOTOEMISSION SPECTROSCOPY

In short, IPE can be considered as a process of optically induced transition of photo-excited mobile carriers form one medium into another one across the interface between them. IPE spectroscopy has been the standard method to characterize the relative energies of electron states at interface of condensed phase materials for more than 40 years. Such studies are of great importance for modern advanced MOS devices which utilize non-native metal oxide with high dielectric constant as gate insulator. Application of high-*k* dielectric materials poses a number of fundamental physical questions and concerns. For instance the atomic structure of a thin oxide at low temperature is not expected to be exactly the same as that of the stoichiometric thermodynamically stable

bulk phase. Thus reliable quantification of band alignment at the interface becomes one of the priorities for high-*k* dielectric implementation.

3.1.1 Basic physics of MOS capacitor

Since the IPE involves the measurement of photocurrent from a biased MOS capacitor, we need to understand some fundamental MOS device physics. An MOS capacitor, which is comprised of a metal gate, an insulating oxide layer and a semiconductor, is incorporated in the surface of most semiconductor devices.

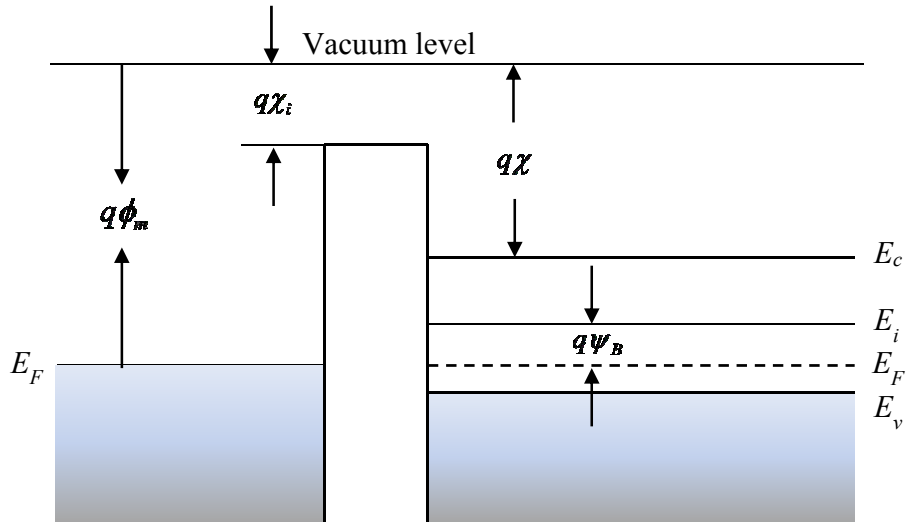

Figure 17: Band alignment of an ideal MOS capacitor at equilibrium for *p*-type semiconductor.

The band alignment of an ideal MOS capacitor is depicted in Figure 17, where ϕ_m is the work function of the metal electrode, χ_i is the electron affinity of the insulator, and the Fermi potential is defined by the substrate doping concentration $\psi_B = \frac{kT}{q}\ln(\frac{N_A}{n_i})$. The total capacitance is composed of oxide capacitance in series with the substrate capacitance $1/C = 1/C_{OX} + 1/C_s$ which varies with the gate voltage due to the band bending influenced by external bias. The flatband condition occurs when the bands within the semiconductor substrate are flat, *i.e.* there is no charge in the substrate. The gate bias in this circumstance is called flatband voltage, which in general equals the work function difference between the metal gate and semiconductor substrate, *i.e.* $V_{FB} = \phi_m - \phi_s$. This flatband voltage is usually extracted from a C-V measurement, where $C_s\Big|_{FB} = \sqrt{\frac{q^2 \varepsilon_s N_A}{kT}}$ [41].

At all ranges of operation, a simple relation of voltage drop across the MOS capacitor is satisfied:

$$V_g = V_{FB} + V_{OX} + \psi_s, \tag{8}$$

where V_{OX} is the voltage drop across the oxide and ψ_s is the surface potential of semiconductor substrate (surface band bending). Thus the electric field at the semiconuctor/oxide interface yields:

$$F = \frac{V_{OX}}{t_{OX}} = \frac{V_g - V_{FB} - \psi_s}{t_{OX}} \approx \frac{V_g - V_{FB}}{t_{OX}} \tag{9}.$$

The latter is true when the doping level is not very high, thus the surface band bending is negligible.

3.1.2 Quantum yield of internal photoemission transition

The physical process of IPE transition can be divided into three major steps: (1) photo-excitation of carriers inside emitting solid (emitter); (2) transport of the photo-

excited carriers towards the interface of emitter; (3) escape of the injected carrier over the potential barrier. This photoemission process is usually quantified by the quantum yield which is defined as the average number of injected charge carriers per one absorbed photon, *i.e.*

$$Y = \frac{n_e}{n_{ph}} = \frac{I \times h\nu}{P \times T \times A}, \tag{10}$$

where I is the photocurrent, P is the total incident light intensity, T is the transmission coefficient of the gate window, and A the sample surface area under illumination, which are all measurable quantities.

The general form of quantum yield can be described by Powell's model [46]:

$$Y = C(h\nu)[h\nu - \Phi(F)]^p \exp[-\frac{x_m(F)}{l}], \tag{11}$$

where $C(hv)$ is a photon-energy-dependent proportionality constant, l is the phonon scattering mean free path, $\Phi(F)$ is the field-dependent barrier height and $x_m(F)$ is the location of the potential maximum due to the image force barrier lowering effect discussed below. The last term describes the transport within the image potential well which corresponds to step (3). The power exponent p is determined by the emitter material or the initial density of states. Especially for electron injection from semiconductor VB, $p = 3$; for metal, $p = 2$. Thus the field-dependent barrier height can be obtained from the threshold of quantum yield spectrum.

3.1.3 Image force barrier lowering effect

At the injecting interface for electron emission, the barrier shape is usually distorted due to the Coulomb interaction between the escaped electron and the unscreened hole it left behind in the semiconductor or the image charge it induces at the metal gate. This effect is called image force barrier lowering, and results in a field

dependence of both the magnitude and position of the barrier top as suggested in Figure 18.

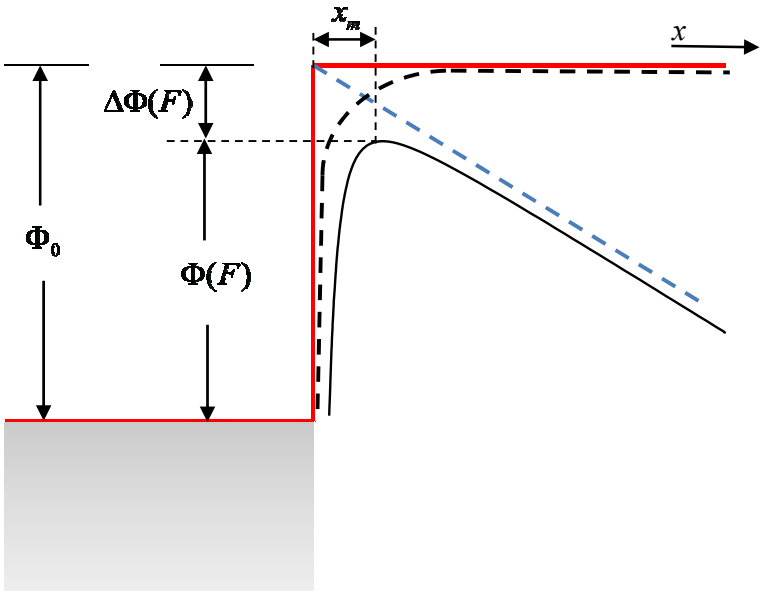

Figure 18: Potential profile for image force barrier lower effect.

The red line represents the step-wise intrinsic batter height, the blue dotted line is due to the external DC bias, and the Coulomb potential profile is denoted by the black dotted line. Thus the potential profile at injecting interface can be written as:

$$\Phi(x) = \Phi_0 - qFx - \frac{q^2}{16\pi\varepsilon_i\varepsilon_0 x}, \tag{12}$$

where ε_i is the dielectric constant of gate insulator. The field-dependent barrier height is:

$$\Phi(F) = \Phi_0 - \Delta\Phi(F) = \Phi_0 - q\sqrt{\frac{qF}{4\pi\varepsilon_i\varepsilon_0}}, \tag{13a}$$

and the position of the potential top is

$$x_m(F) = \sqrt{\frac{q}{16\pi\varepsilon_i\varepsilon_0 F}} \tag{13b}.$$

Image force barrier lowering effect is essentially due to the screening properties of materials. The transport time of injected carrier across the interface is typically on the order of 10^{-15} s. The dielectric relaxation time which describes the response time of screening charges to an electric field for semiconductor at moderately doping is on the order of 10^{-12} s, while this response time for metal is 10^{-16} s. Thus at the interface of a metal, an image charge is induced immediately at the metal surface, while at the surface of a semiconductor, an unscreened hole plays the role of the image charge. So in order to extract the zero field barrier height, a linear extrapolation is usually used in the $\Phi(F) - \sqrt{1/F}$ plot (Schottky plot), where each field dependent barrier height is obtained from the threshold of quantum yield spectrum according to the photon energy dependence described in Equation (11).

3.2 EXPERIMENTAL PROCEDURE

Thin films (3 nm or 10 nm) of high-*k* oxides (Al_2O_3, BeO or HfO_2) were deposited on clean p type ($n_a \approx 10^{15}$ cm^{-3}) Si(100) substrates. Si wafers were pre-cleaned by HF dipping before transfer to a Cambridge Nanotech^{TM} atomic layer deposition (ALD) module. Oxide film depositions were carried out at 200 °C using trimethyl aluminum (TMA) + H_2O pulses for Al_2O_3 deposition, $Be(CH_3)_2$ + H_2O as precursors for BeO, and tetrakis ethylmethylamino hafnium (TEMAHf) + H_2O for HfO_2. Some samples were then subjected to post-deposition anneal (PDA) in N_2 atmosphere at 600 °C (for 1 min) or 900 °C (for 30 s). Samples for IPE measurement had ~ 10 nm thick oxides (11.1nm for Al_2O_3, 10nm for BeO and 8.8nm for HfO_2). In order to apply bias and detect photocurrent, MOS capacitors were fabricated. 15nm reactively sputtering TaN (for BeO) or e-beam evaporated Au (for Al_2O_3 and HfO_2) was deposited on the ALD oxides, then patterned by photo-lithography to form 540 X 540 μm^2 top gate electrodes, which

functioned simultaneously as semi-transparent optical input windows. The backside of the Si substrate was scribed before bonding with melted indium to form a good ohmic contact. The flat band voltage, which takes into account the work function difference between the metal electrode and Si substrate, was measured by C-V for each MOS capacitor. Samples for IMPE-EFISH measurement had ~3 nm thick oxides to enable efficient transport of injected carriers to the free oxide surface [15]. The physical thicknesses of the deposited oxide layers were determined by spectroscopic ellipsometry and confirmed with transmission electron microscopy (TEM).

For IPE measurement, bias voltages were applied to the metal electrodes via tungsten contact probe needles (5μm tip diameter). The MOS structure was illuminated through the semi-transparent metal electrode by continuous wave radiation from a 75W Xeon lamp source dispersed with a computer controlled monochromator (blazed at 300nm, 4nm spectral resolution) at normal incidence. The entire setup as depicted in Figure 19 is immersed in a purged dry N_2 ambient to avoid ultraviolet absorption in air. Yield spectra were determined from dc-photocurrent (typically pA) across the biased MOS structure measured with a Keithley 6514 electrometer, and normalized to the incident photon flux detected by a calibrated photodiode.

For IMPE-EFISH, p-polarized ~150 fs optical pulses from a mode-locked Ti:sapphire laser with wavelength tunable from 780nm to 840nm (~10 nm bandwidth), average power varied from 70 mW to 300 mW with ND filters, and 76 MHz repetition rate were focused at 45^o incident angle to a ~30 μm diameter focal spot on the sample similar to the one shown in Figure 5. A photomultiplier tube detected reflected p-polarized SHG as a function of time over a period of 1 to 2 minutes, during which photo-injected carriers accumulated at the free oxide surface.

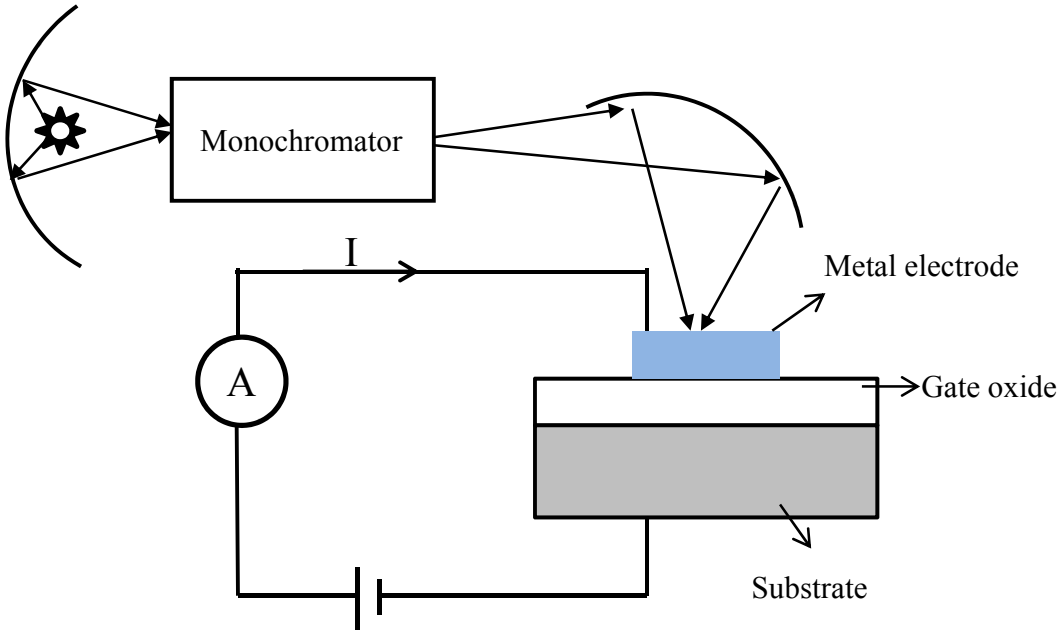

Figure 19: Schematic experiment setup for IPE measurement.

3.3 EXPERIMENTAL RESULTS AND DISCUSSION

3.3.1 Al_2O_3/Si

Both IMPE-EFISH and IPE were applied to as-deposited Si/Al_2O_3 samples with no PDA. This enabled direct comparison of the results with previous IMPE-EFISH [17] and IPE [43,44] measurements of *annealed* Si/Al_2O_3 samples.

Figure 20 presents IMPE-EFISH data for mode-locked pulsed illumination at (a) 810 nm and (b) 800 nm at various powers. The initial time-dependent rate of increase of the SHG signal is significantly faster for 800 nm than for 810 nm at an equivalent power. Moreover, for wavelengths longer than 810 nm, the initial rate of increase is similar to that shown in panel (a), whereas for wavelengths shorter than 800 nm, it is similar to that shown in panel (b). Discontinuous change at 805 ± 5 nm suggests that the order of multi-photon photoemission decreased from *n* to *n*-1 in going from 810 to 800 nm illumination,

thereby increasing the charge generation rate. The IMPE-EFISH dynamics were unaffected by simultaneous irradiation of the same photo-excited spot by a continuous-wave of the same wavelength and average power, ruling out a thermal origin of the dynamic behaviour. The electrostatic origin of the dynamics was confirmed by grounding the free surface after mode-locked laser irradiation, which quenched the accumulated increase in SHG signal. This demonstrated that the electrostatic field built up by electrons injected from the Si substrate into the Al_2O_3 conduction band and trapped at the free surface was responsible for the increased signal.

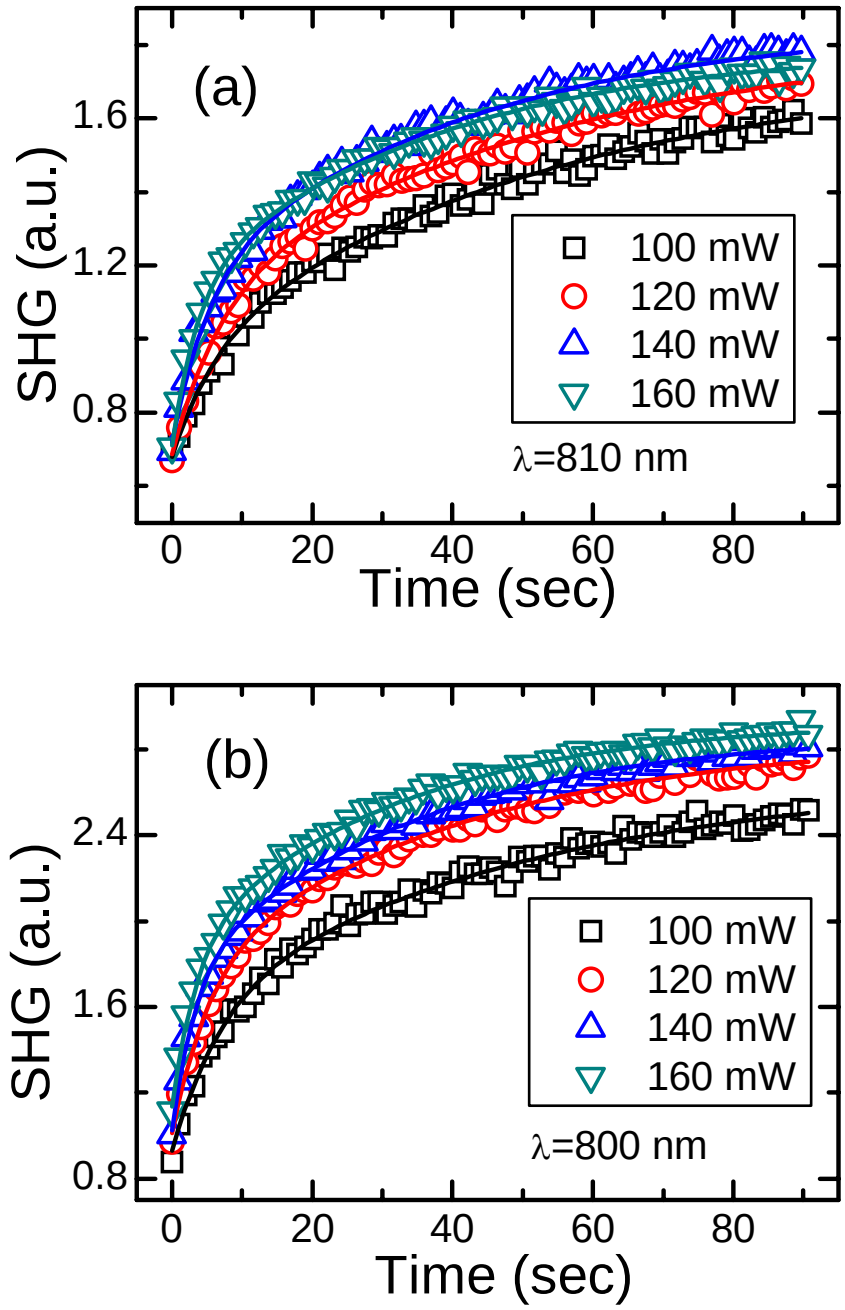

Figure 20: IMPE-EFISH data at various incident powers for 810nm (a) and 800nm (b) laser pulse illumination. Curves are fits to the data using a single-trap model (see Equation (14)).

To obtain quantitative results, the time-dependent IMPE-EFISH data was fit to a single trap charge kinetics model [16-20, 45] in which the electrostatic field grows as $E^{DC}(t) \propto n(t) = n_0(1-e^{-t/\tau})$, where *n(t)* is the trapped charge density at surface and *1/τ* is the trapping rate. The time-dependent SHG intensity $I^{(2\omega)}(t)$ then takes the form

$$I^{(2\omega)}(t) \propto \left|\chi^{(2)} + \chi^{(3)}E^{DC}(t)\right|^2 \propto \left|a + (1-e^{-t/\tau})\right|^2, \qquad (14)$$

where $\chi^{(2)}$ is the second-order nonlinear susceptibility of the Si/Al_2O_3 interface, which is responsible for background time-independent SHG, and $\chi^{(3)}$ is the third-order nonlinear susceptibility of bulk Si in the substrate space-charge region, from which time-dependent SHG arises. The multi-photon carrier injection rate, and thus the trapping rate, depend on incident laser intensity *I* as $1/\tau \propto \left[I^{(\omega)}\right]^n$, where *n* is the number of photons required to promote electrons from the Si valence band (VB) to the oxide conduction band (CB).

Figure 21 presents a semi-log plot of trapping constant τ obtained from fits to the IMPE-EFISH data vs. incident laser power. Multi-photon order *n* is obtained from the slope of the lines fitted to the data points. At λ = 810nm (*hv* = 1.53 eV), the slope is -3, indicating 3 photons are needed to inject electrons, whereas at λ = 800nm (*hv* = 1.55 eV), the slope is -2, signifying 2-photon photoemission. As photon energy varies, a step-wise transition from 3-photon to 2-photon photoemission is observed, as illustrated in Figure 22. We can therefore identify the barrier height for charge injection by $\Phi_e = 2h\nu_t = 3.08 \pm 0.04\,eV$, where $h\nu_t$ = 1.54 ± 0.02 *eV* is the single photon energy at the transition point [16,17]. The conduction band offset (CBO) is then obtained by subtracting the Si band gap E_g = 1.1 eV, yielding $\Delta\Phi_c = \Phi_e - E_g = 1.98 \pm 0.04\ eV$. This result is an excellent agreement with the value $\Delta\Phi_c$ = 2.02 ± 0.04 eV reported by Gielis *et al*. based on IMPE-EFISH measurements of Si/Al_2O_3 structures after PDA in N_2 at 425 ^oC, indicating the CBO is insensitive to 425 ^oC PDA.

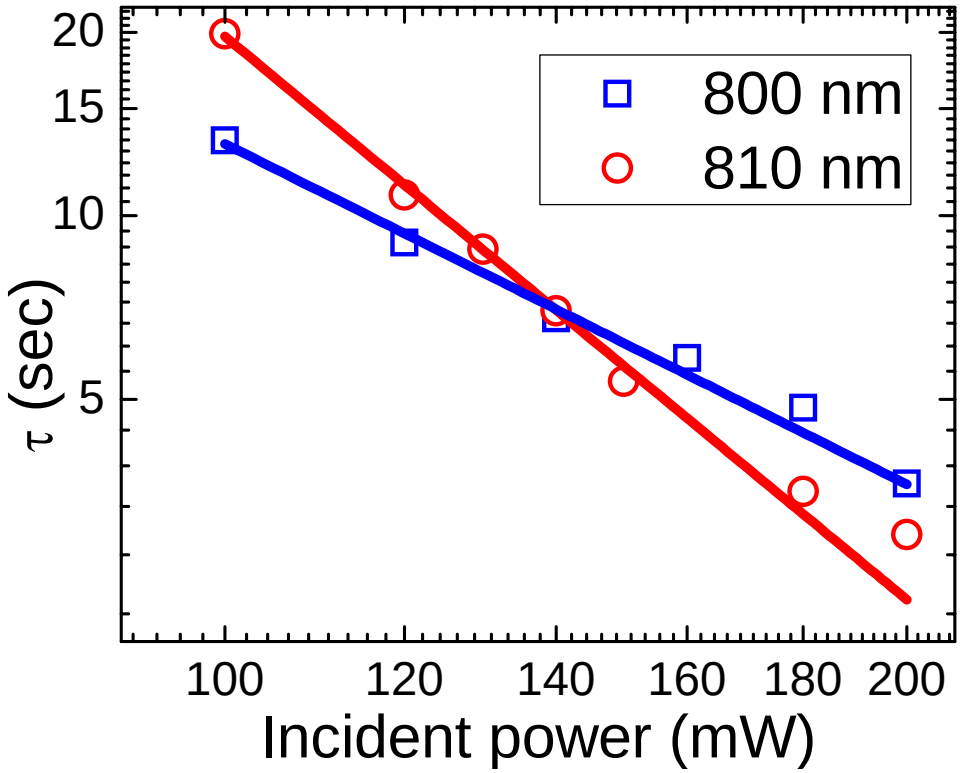

Figure 21: Laser power dependence of time constants from the IMPE-EFISH data in Figure 20 at two different wavelengths.

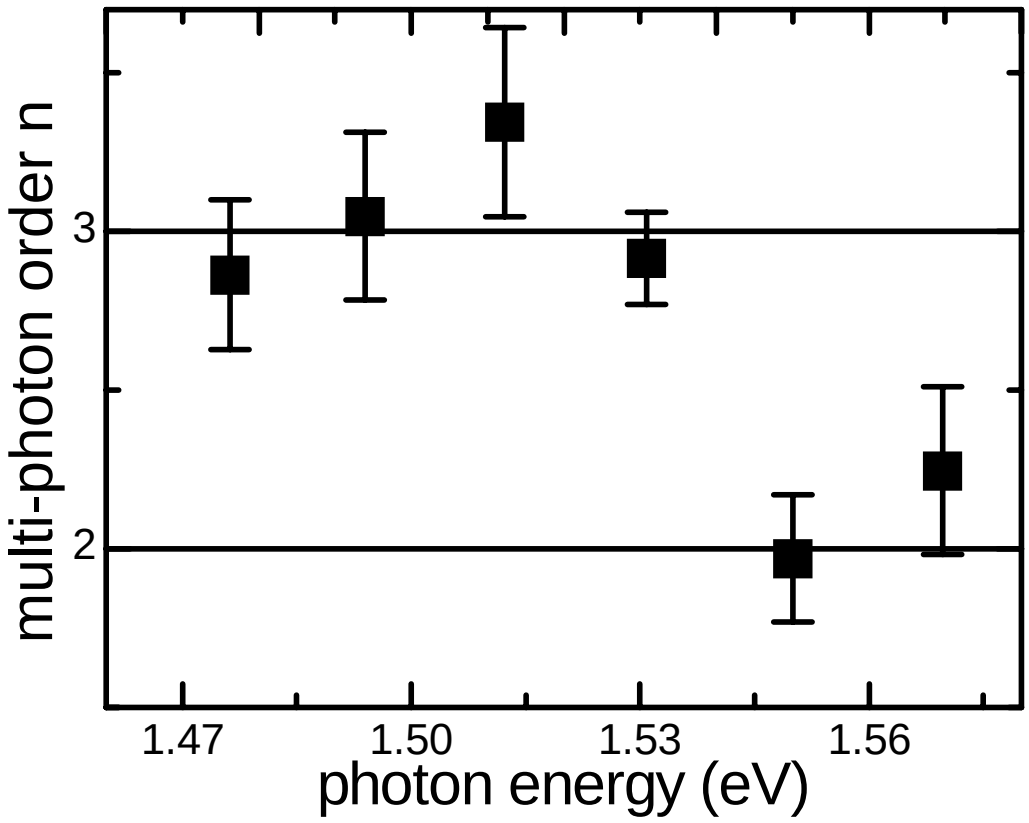

Figure 22: Order of multi-photon absorption process as a function of fundamental photon energy.

Figure 23 shows the IPE yield spectrum of the $Au/Al_2O_3/Si$ MOS capacitor under positive bias. The strong E_1 and E_2 features are *prima facie* evidence that the IPE photon current originates from electrons photo-excited from the Si VB to Si CB, prior to injection into the Al_2O_3 CB. Thus the threshold near 3 *eV* corresponds to the barrier height Φ_e between Si VB edge and Al_2O_3 CB edge.

The electrostatic field *F* was calculated from the gate voltage V_g and the measured flatband voltage V_{FB} according to Equation (9). According to the Powell model [42], the yield near the threshold varies with photon energy $h\nu$ as $Y(h\nu) \propto [h\nu - \Phi_e(F)]^3$,

enabling extraction of barrier height $\Phi_e(F)$ by plotting $Y^{1/3}$ vs. $h\nu$ near threshold. Under bias, however, the barrier height $\Phi_e(F)$ depends on the electrostatic field F because of the Schottky effect [42]. So the potential barrier scales linearly with square root of field as $\Phi(F) = \Phi_0 - q\sqrt{\frac{qF}{4\pi\varepsilon_i\varepsilon_0}}$ [46].

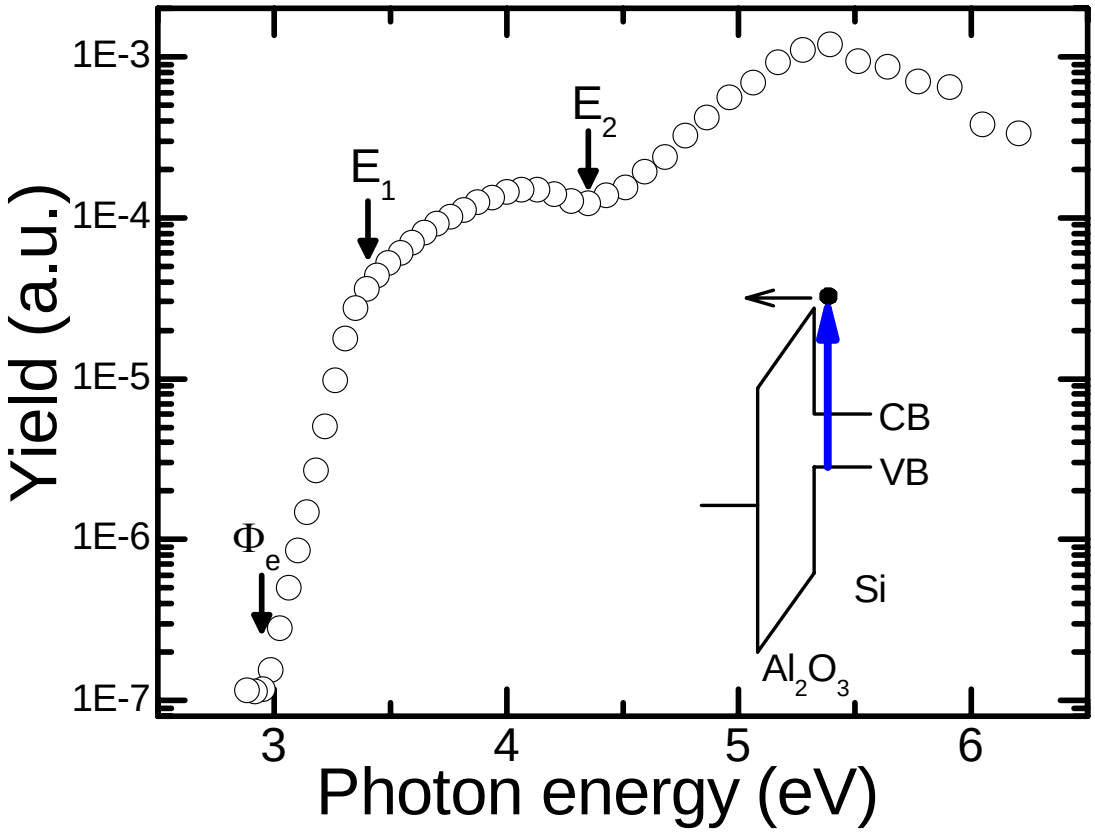

Figure 23: IPE yield spectra vs. photon energy measured with +1.4V bias on the Au electrode in (100)Si/Al_2O_3/Au capacitors. Inset shows the schematic band diagram for charge injection.

The field-*dependent* threshold is obtained by linearly extrapolating a Schottky plot of $\Phi_e(F)$ vs. $F^{1/2}$ to $F = 0$, as shown in Figure 24. This plot yields zero-field barrier height of $\Phi_e(0) = 3.13 \pm 0.04$ *eV* for electron injection from the Si VB maximum to the Al_2O_3 CB minimum. This in turn yields a CBO of $\Delta\Phi_c = 2.03 \pm 0.04$ eV, which agrees within experimental error with the results obtained from IMPE-EFISH on a sample with an oxide nearly 4 times thinner. It is also consistent with the value $\Delta\Phi_c = 2.13 \pm 0.08$ eV reported by Afanas'ev et al. [43] based on IPE measurements of $Si/Al_2O_3/Au$ structures after PDA in O_2 at 500 ^oC.

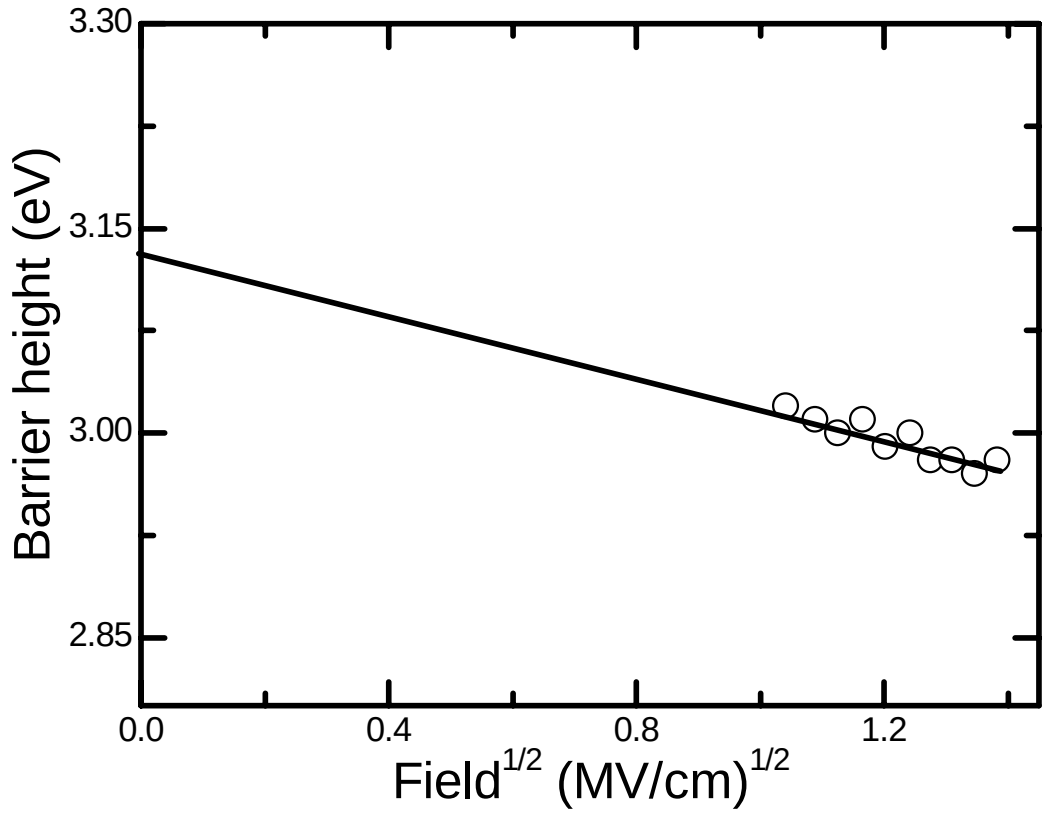

Figure 24: Schottky plot of the yield spectra thresholds to determine the intrinsic zero-field barrier height of $(100)Si/Al_2O_3/Au$ capacitors by linear extrapolation.

The cited error of ±0.04 eV in our IPE threshold determination reflects uncertainties arising from monochromator resolution, photodiode calibration inaccuracy and random error due to fluctuation of dark current, photocurrent and light intensity. There can, however, be additional systematic error related to the choice of model describing the photon energy dependence of quantum yield near threshold, *i.e.* the exponent in the expression for yield $Y(h\nu) \propto \left[h\nu - \Phi_e(F)\right]^3$ in Powell's model [42]. This choice is affected by material and interface properties including density of states in the electrode, mean free path of injected carriers, optical transition strengths in the semiconductor emitter, and interface barrier non-uniformity [14]. Error from this model choice generally does not exceed 0.1eV [14, 47, 48]. Some authors attempt to include this systematic error by citing a larger uncertainty, as in the Afanas'ev *et al.* [43] result cited above.

The above measurements determine only the CBO of Si/Al_2O_3, and indicate that it is insensitive to oxide thickness in the range 3 to 11 nm or to PDA at $\leq$ 500 ^oC. In principle IMPE-EFISH and IPE can also determine the valence-band offset (VBO). One way of doing this is to detect electrostatic fields (IMPE-EFISH) or DC photocurrents (IPE) resulting from direct excitation of carriers across the oxide band gap. The gap thus determined, combined with the CBO, yields the VBO. Unfortunately, our current light sources do not tune far enough into the UV to excite carriers across the Al_2O_3 gap of 6 – 7 eV. Some previous IPE studies have reported a widening of the Al_2O_3 gap, and an accompanying increase in VBO, accompanying PDA at > 800 ^oC [49]. On the other hand, a recent spectroscopic ellipsometry study reported a decrease in the Al_2O_3 gap accompanying similar PDA [50]. Extension of the tuning ranges of our IMPE-EFISH and IPE measurements may therefore be a fruitful area for future research on Al_2O_3 and other

wide gap oxides. In the next section we report measurements on a smaller gap oxide, for which both CBO and VBO can be determined.

3.3.2 HfO_2/Si

IMPE-EFISH measurements of Si(001)/HfO_2 structures with 4 nm ALD HfO_2 films have been reported before [18]. One result of that study was that the kinetics of charges excited near the Si VB/HfO_2 CB barrier was complicated by simultaneous ionization of oxygen vacancy point defects in the HfO_2 layer. Here, therefore, we present band-offset measurements based purely on IPE.

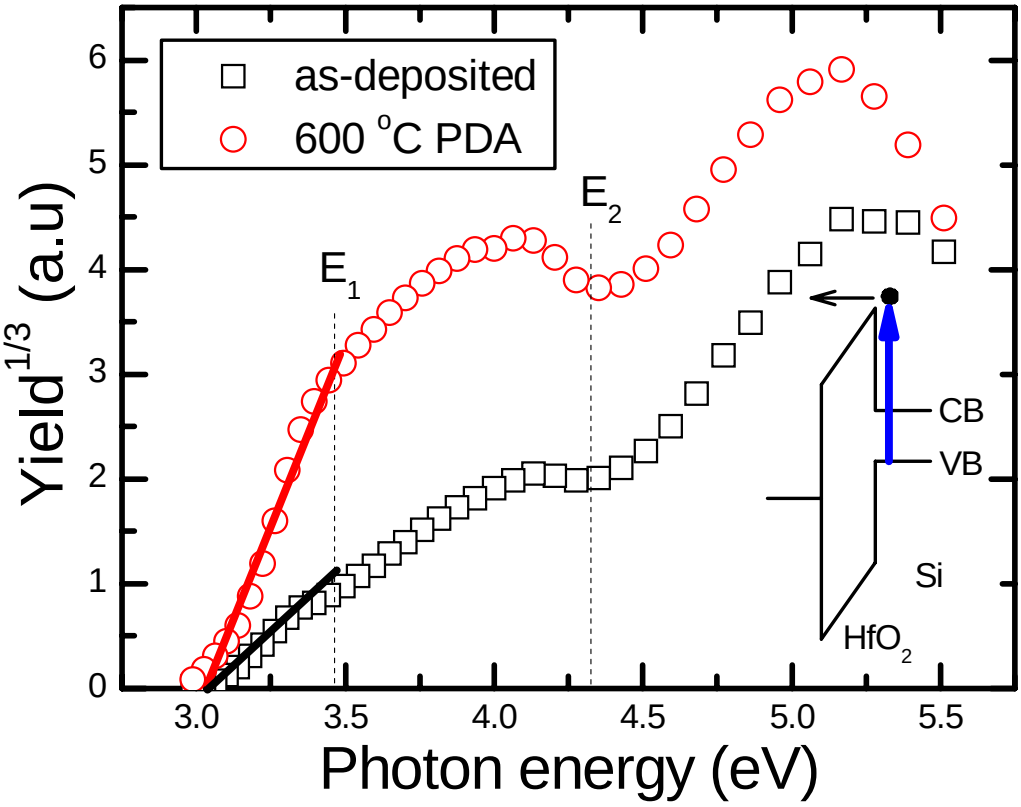

Figure 25: Cubed root of IPE yield spectra as a function of photon energy measured with +1.6V bias on the Au electrode for capacitors with as-deposited and annealed HfO_2 and the inset shows the schematic band diagram for charge injection.

Figure 25 presents spectra of the cubed root $Y^{1/3}(h\nu)$ of IPE yield under forward bias +1.6 V for as-deposited structures (black open squares) and after PDA at 600 ^{o}C (red open circles). Strong modulation of both spectra at E_1 and E_2 critical points again shows that the photocurrents originate from optical transitions within the Si substrate. The solid lines indicate fits of the near-threshold $Y^{1/3}(h\nu)^{1/3}$ to a Powell model to determine $\Phi_e(F)$ at this bias. Although as noted earlier deviations of the measured $Y^{1/3}$ from linear dependence on $h\nu$ create some uncertainty, the fits indicate identical $\Phi_e(F)$ for the as-deposited and annealed samples, despite strong PDA-induced changes in the overall shape of $Y^{1/3}(h\nu)$ evident in Figure 25.

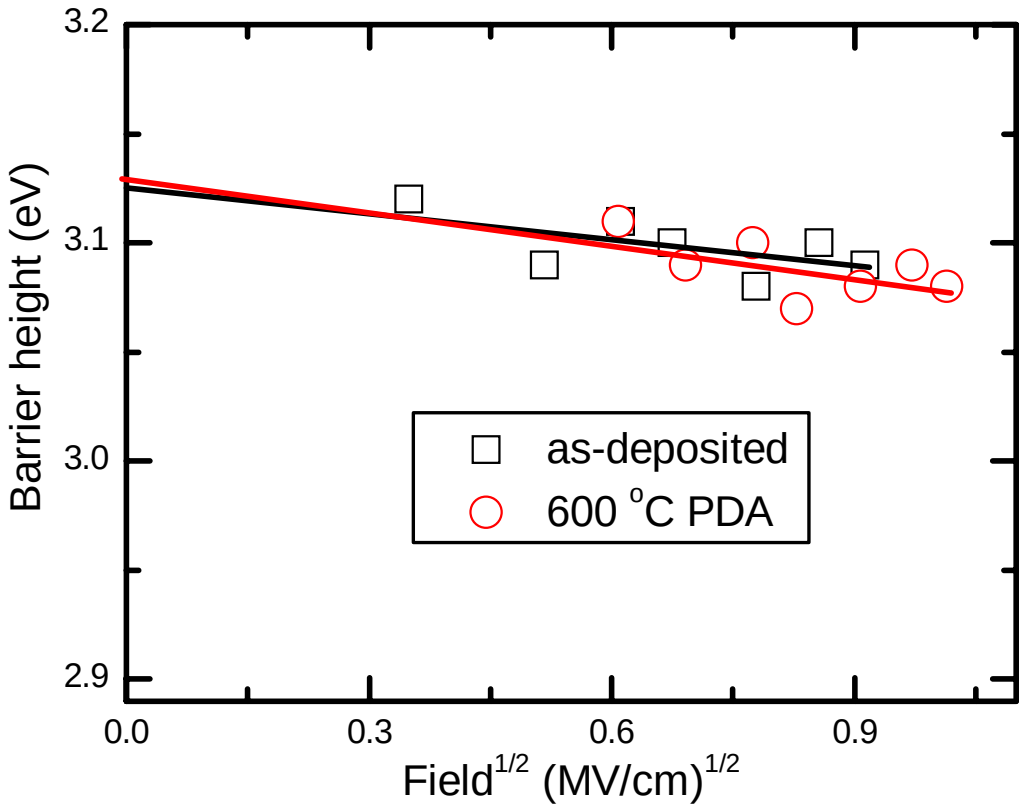

Figure 26: Schottky plot of the MOS capacitors with as-deposited and annealed HfO_2 gate oxides.

Figure 26 presents a Schottky plot for the two samples. Within measurement error, $\Phi_e(F)$ remains the same for both samples at all biases. By extrapolation to $F = 0$, we thus obtain the PDA-independent CBO of $\Delta\Phi_c = 2.02 \pm 0.04$ eV, coincidentally nearly identical to the CBO of Si/Al_2O_3.

Because of the band gap of HfO_2 is less than 6 eV, our light source can excite direct transitions across this gap. The gap is then most readily determined by measuring photocurrent with the sample under *reverse* bias, as illustrated in the inset of Figure 27. The main panel of Figure 27 presents spectra of the square root $Y^{1/2}(hv)$ of IPE yield with the as-deposited (black open squares) or annealed (red open circles) sample under reverse bias -1.6 V. At photon energies $hv < 5.5$ eV, the spectrum is featureless (no E_1 or E_2 features) since the photocurrent now originates from optical transitions in the metal gate electrode rather than the Si substrate. At higher photon energies, a discontinuous linear rise in $Y^{1/2}(hv)$ is observed as the incoming light begins to excite electron-hole pairs within the oxide. The linear rise in $Y^{1/2}(hv)$ above E_g is consistent with experimental observations that photocurrent yield, and thus density of states, is approximately proportional to $(hv - E_g)^2$ just above the band edge of many insulators [51, 52]. The photo-excited electron-hole pairs experience no image force barrier lowering [53]. Thus band gap energy can be directly determined by extrapolating $Y^{1/2}(hv > 5.5\ eV)$ to zero yield, as illustrated by the solid red and black lines in Figure 27, without the need to extrapolate to zero field. This is the motivation for determining oxide band bap in a reverse bias configuration.

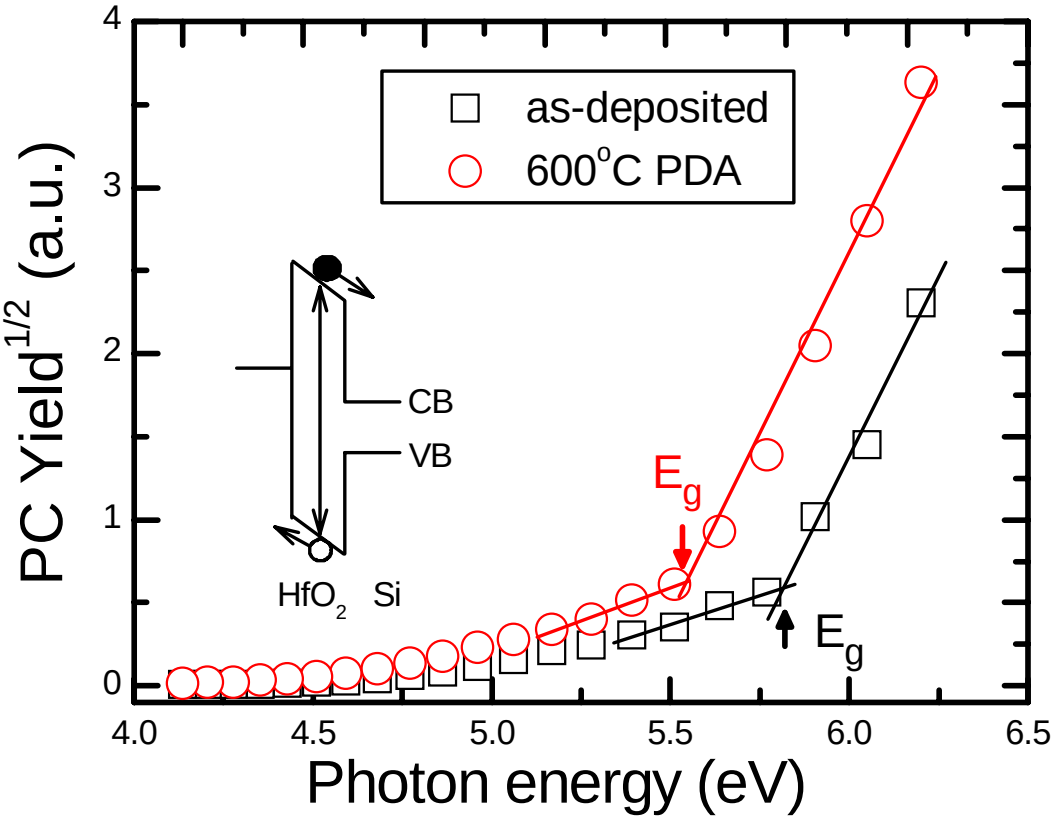

Figure 27: PC spectra of (100)Si/HfO_2/Au for as-deposited and annealed samples with the Au electrode biased at -1.6V. The inset shows the schematic band diagram for PC process.

The results in Figure 27 indicate that the band gap of HfO_2 shrank from 5.82 eV for as-deposited to 5.53 eV for annealed samples. In view of the absence of an accompanying CBO shift, this 0.3 eV decrease in band gap implies a corresponding decrease of 0.3 eV up-lift of the VB edge of HfO_2, as illustrated in Figure 28.

The annealing temperature of 600 ^oC is well below the crystallization temperature (700 ^oC) [54] of as-deposited polycrystalline HfO_2 subjected to rapid thermal annealing. Thus crystallization cannot explain the change in VBO. This shift in VB edge may be caused by the diffusion of atomic oxygen away from the interfacial layer to passivate the

intrinsic O-vacancy defects in HfO_2 during PDA which have been identified by electron spin resonance (ESR), X-ray photoelectron spectroscopy (XPS) and electron energy loss spectroscopy (EELS) [55-57]. A localized molecular orbital (LMO) model predicts that the VB maximum states of transition metal oxide like HfO2 are composed mostly by the O 2p orbital [58-60]. The shift of the VBM may be caused by the change in the local electronic states related to O bonding, as investigated by XPS and EESL [61]. Compared to other methods of band alignment characterization, IPE uniquely excels by requiring no ultra-high vacuum (UHV) systems.

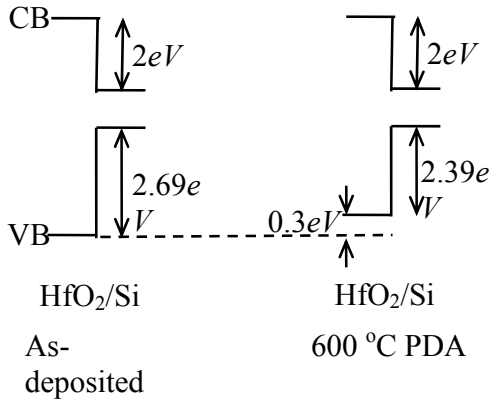

Figure 28: Schematic band diagrams for as-deposited and annealed HfO_2 on Si determined from IPE measurement.

3.3.3 BeO/Si

Hafnium-based high-*k* dielectrics recently replaced SiO_2 as gate oxide in high performance devices in order to counteract gate leakage currents while continuing scaling

of MOSFETs. However, research continues to further reduce the effective electrical thickness of the high-*k* gate stacks. One of the options is to suppress the growth of the SiO_2 film at the interface between the high-*k* dielectric and Si substrate and, possibly, replace it with a dielectric of a higher *k* value. Recently ALD BeO has emerged as a promising interfacial passivation layer (IPL) for both Si and III-V devices [50, 62]. BeO is thermodynamically stable in contact with Si, in accord with the calculated Gibbs free energy [63], and provides a good diffusion barrier because of the small interstitial size. One of the key criteria in evaluating an IPL is the offset of its conduction and valence bands from those of the substrate, since this governs the barrier height for tunneling and thermionic emission leakage currents, and provides insight into interfacial bonding [12]. Thus here we present optical characterization of the conduction and valence band offsets of ALD BeO/Si(100). As in the previous sections, we measure the conduction band offset (CBO) using IPE and IMPE. We measure valence band offset (VBO) by synchrotron X-ray photoelectron spectroscopy (XPS).

IMPE-EFISH measurements are shown for the as-deposited BeO/Si(100) sample for various incident powers in Figure 29(a). As before, the electrostatic origin of this TD-SHG dynamics was confirmed by grounding the free surface after irradiation, and thereby quenching the accumulated increase in SH signal. As for the control Al_2O_3/Si(100) sample, the kinetics of charge trapping are well described by a single trap model: $E^{DC}(t) \propto n(t) = n_0(1 - e^{-t/\tau})$, and TD-SHG intensity $I^{(2\omega)}(t)$ can be described by Equation (14). Following the same analysis used for Al_2O_3/Si, the multi-photon carrier injection rate, and thus the trapping rate, depends on incident laser intensity I as $1/\tau \propto \left[I^{(\omega)}\right]^n$, where n is the number of photons required to promote electrons from Si VB to oxide CB, as shown in the inset of Figure 29(b). The log-log plot of $1/\tau$ vs. $I^{(\omega)}$ in the main panel of Figure 29(b) shows that n = 3 at 780 nm ($h\nu$ = 1.60 eV). When the photon energy $h\nu$

varies, a transition from *n*-photon to (*n-1*)-photon photoemission occurs when the multi-photon energy (*n* - 1)*hv* sweeps across the barrier of height Φ_e for charge injection, as shown in Figure 31(b). The CBO between BeO and Si is then given by $\Delta\Phi_c = \Phi_e - E_g$, where E_g = 1.12 eV is the band gap of Si, which yields the CBO $\Delta\Phi_c$ = 2.21 ± .03 eV. Valence band spectra were measured on samples with 3 nm BeO film mounted in an ultrahigh vacuum chamber under irradiation of the National Institute of Standards and Technology (NIST) beam line X24A at the National Synchrotron Light Source with 4.36 *keV* beam energy at 10^{12} ph/sec flux focused on ~1 mm diameter spot. The result of this measurement will be discussed below.

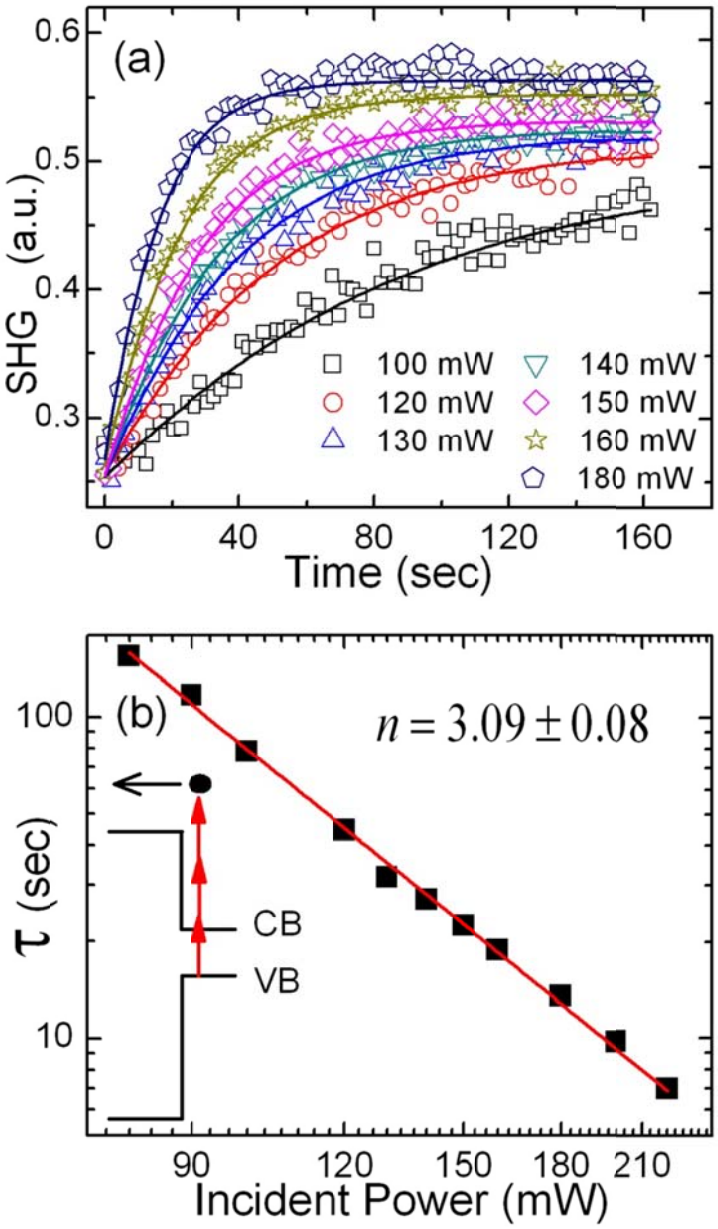

Figure 29: (a) TD-SHG data (open symbols) for ALD BeO/Si(100) at various incident powers of 780 nm laser pulses illumination; the lines are fitting curves based on Equation (14). (b) Laser power dependence of time constant from the TD-SHG data in (a). The insert shows the schematic band diagram for multi-photon injection.

Figure 30 shows IPE yield spectra of a TaN/BeO (10 nm)/Si MOS capacitor under positive bias. As before, the presence of E_1 and E_2 spectral features shows that electrons are injected from the Si substrate, although the optical modulation depth at E_1 and E_2 singularities is much weaker than for amorphous or polycrystalline ALD oxides, like Al_2O_3 and HfO_2 [45]. A high-resolution TEM image [64] shows that ALD BeO, unlike Al_2O_3 and HfO_2 , forms a single crystal oxide film. The suppression of the E_1 and E_2 features may be explained by lowering of crystalline symmetry at the interface due to stress from lattice mismatch between the two crystals, since IPE is inherently surface sensitive due to the strong in-elastic electron-electron scattering at the interface with a wide bandgap insulator [65]. PDA further suppresses the E_2 feature, as illustrated in Figure 30. Evidently thermally induced stress further lowers Si surface crystalline symmetry, consistent with observations on thermal oxidized Si surfaces [65].

Field dependent barrier height $\Phi_e(F)$ is determined from the spectral threshold of IPE yield according to the Powell model, *i.e.* $Y(h\nu) \propto [h\nu - \Phi(F)]^3$, which occurs between 3.0 and 3.5 eV for the data in Figure 30. The intrinsic zero-field barrier height $\Phi_e(0)$ for electron injection from Si VB maximum to BeO CB minimum (or possibly CB tail states) is obtained from the Schottky plots in Figure 31(a), which yield $\Phi_e(0)$ = 3.43 eV ± 0.1 eV for the as-deposited sample, and 3.66 ± 0.1 eV and 3.73 ± 0.1 eV, respectively, for samples subjected to PDA at 600 °C and 900 °C. The corresponding CBO values are therefore $\Delta\Phi_c$ = 2.31 ± 0.1 *eV* for the as-deposited sample and 2.54 ± 0.1 *eV* and 2.61 ± 0.1 *eV*, respectively, for the annealed samples. The increasing CBO may indicate the formation of interfacial oxide/silicate during PDA, as suggested by the observation of increased Si-O peak with PDA temperature from the XPS results performed with Al K_α X-ray source [50]. Another possibility is that PDA drives the as-

deposited oxide structure closer to that of bulk BeO, which has a larger band gap (10.6 *eV*) [66].

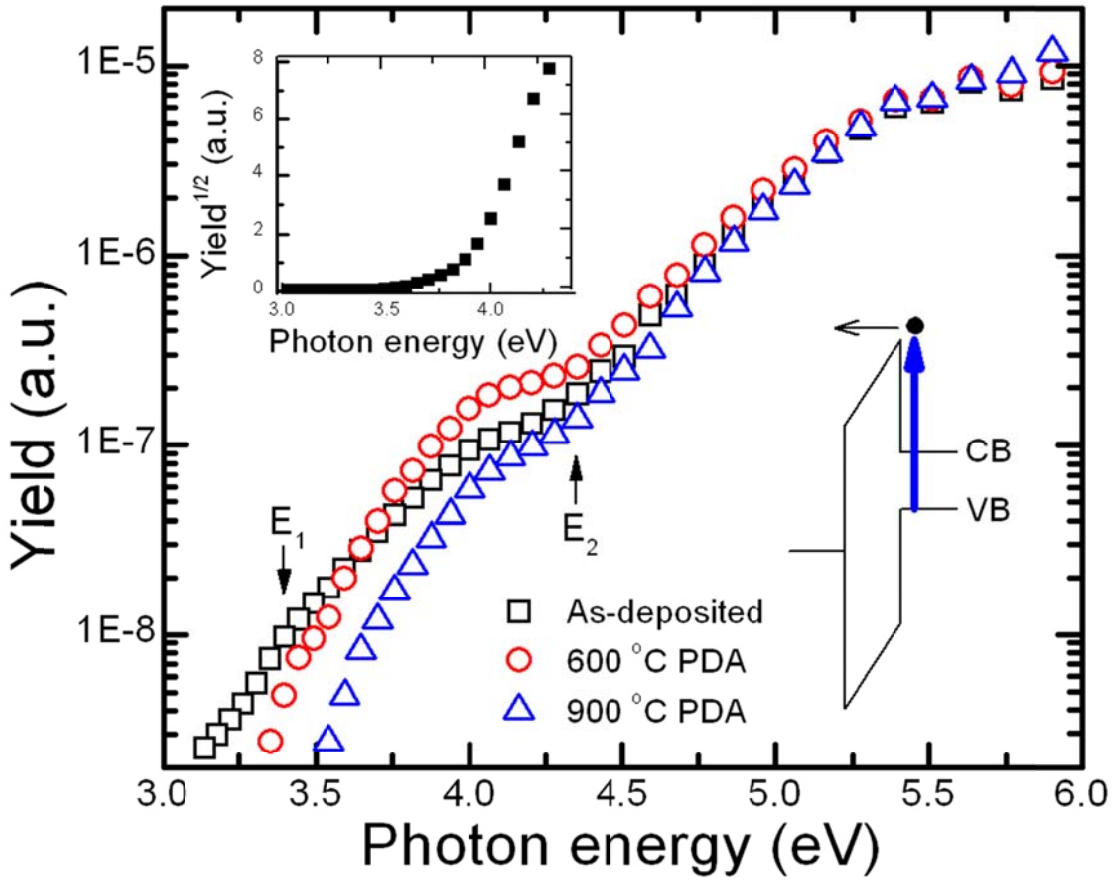

Figure 30: IPE yield spectra as a function of photon energy measured with +2.5V bias on the TaN electrode in (100)Si/BeO/TaN capacitors and the insert on the right bottom corner shows the schematic band diagram for charge injection. The insert on the left top corner shows the square root of yield from as-deposited sample with TaN biased -2.5V.

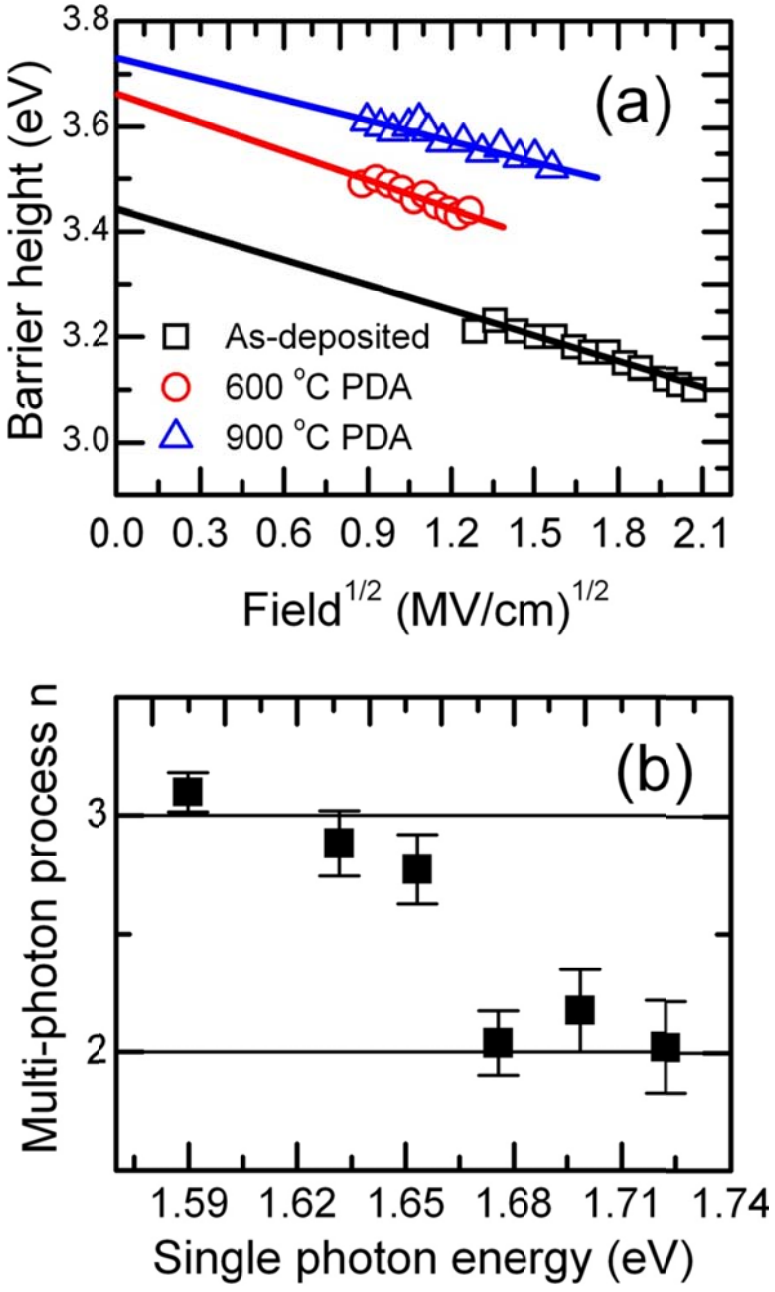

Figure 31: (a) Schottky plot of the yield spectral thresholds for ALD BeO/Si(100) to determine the intrinsic zero-field barrier height by a linear extrapolation. (b) Order of

electron injection process as a function of fundamental photon energy for as-deposited sample.

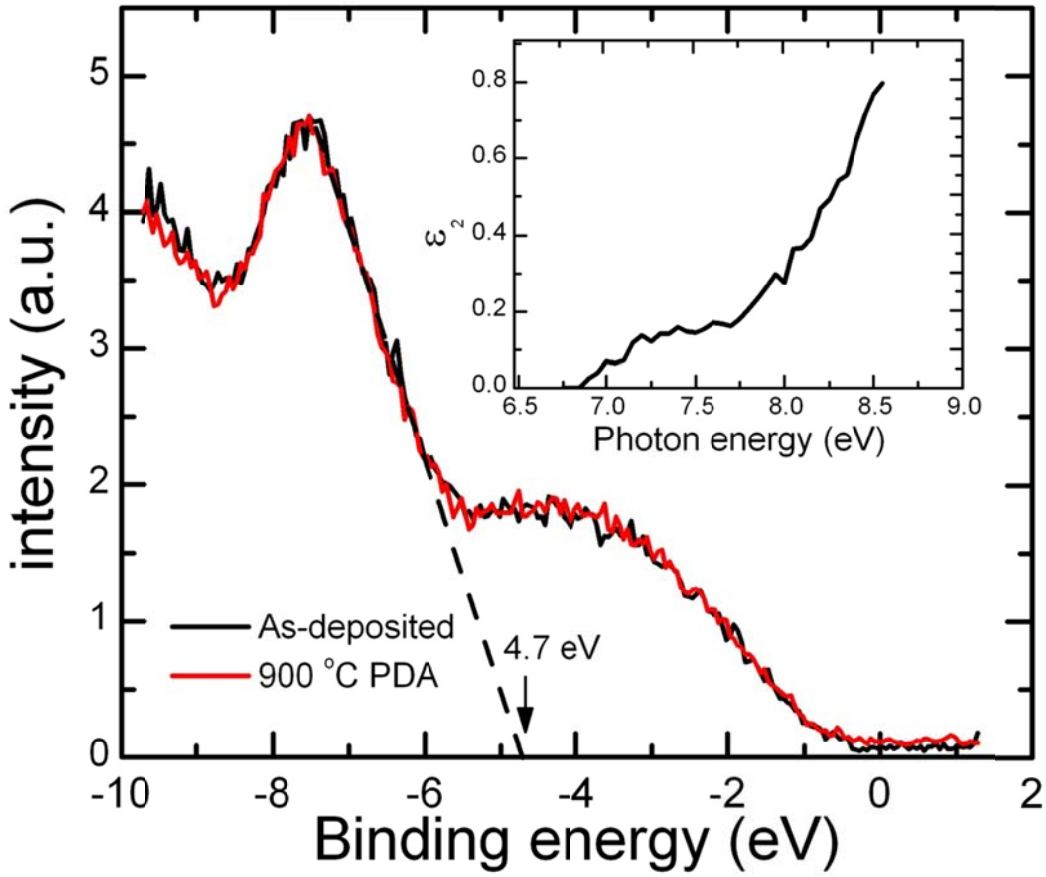

Figure 32: XPS spectra of the as-deposited and annealed BeO VB structure. The inset shows the absorption spectrum of the as-deposited sample measured by SE.

Figure 32 shows the synchrotron XPS spectra of the BeO VB region. To correct for instability in the synchrotron beam energy over time, each VB spectrum was simultaneously measured, then aligned, with the Si $2p_{3/2}$ core level (binding energy = 99.42 eV). The zero of energy of Figure 29 is referenced to the midgap of the silicon substrate. The VB edge is obtained by linear extrapolation of the absorption onset and

found to be 4.7 *eV* below the midgap of Si, which yields VBO = 4.14 ± 0.2 *eV*. Combining the results of IPE and synchrotron XPS measurements, the energy gap separating the BeO VB edge and the states at the IPE/IMPE threshold can be estimated to be ~ 7.57 *eV* for the as-deposited sample. To corroborate this value, absorption was measured by VUV SE of the as-deposited BeO sample (see Figure 32 inset). From the limited absorption spectrum shown, we estimate an absorption edge of 7.75 eV ± 0.25 eV, which is consistent with the gap obtained from IPE and XPS. The SE value, however, is less precise because the weakness of absorption just above threshold introduced considerable uncertainty into proper placement of a linear extrapolation of the absorption onset.

The obtained results show that Si/BeO exhibits a higher barrier to tunneling and thermionic leakage currents than that of Al_2O_3 or HfO_2 [45], thereby complementing the favorable electrical characteristics of Si/BeO MOS devices presented elsewhere [50, 62]. These results also provide a basis for first-principles calculations of the structure of the Si/BeO interface. The BeO gap of ~ 7.57 eV obtained from by IPE/IMPE is considerably smaller than the bulk BeO band gap of ~10.6 eV [66], suggesting that the IPE/IMPE threshold may be governed by a high density of band tail states just below the intrinsic CB minimum. Indeed tail states as much as 4 eV above the VB maximum are evident in the XPS spectrum of Figure 32. Moreover, near-edge x-ray absorption fine structure (NEXAFS) spectra of the present samples measured by Jimmy Price at Brookhaven National Lab, to be presented elsewhere, provide direct evidence of CB tail states as much as 3 eV below the intrinsic CB minimum. This suggests that the absorption edge depicted in the inset of Figure 32 arises from transitions between VB and CB tail states. Figure 33 summarizes the results of the present band offset measurements, with the suspected band tail states indicated by shaded gray areas. These band edge distortions

may contribute to the apparent weakness of critical point features in IPE spectra, in addition to lattice mismatch and/or thermal induced strain [67] as suggested earlier. It will be of interest in the future to apply the present methods to band alignment measurements of BeO on III-V substrates.

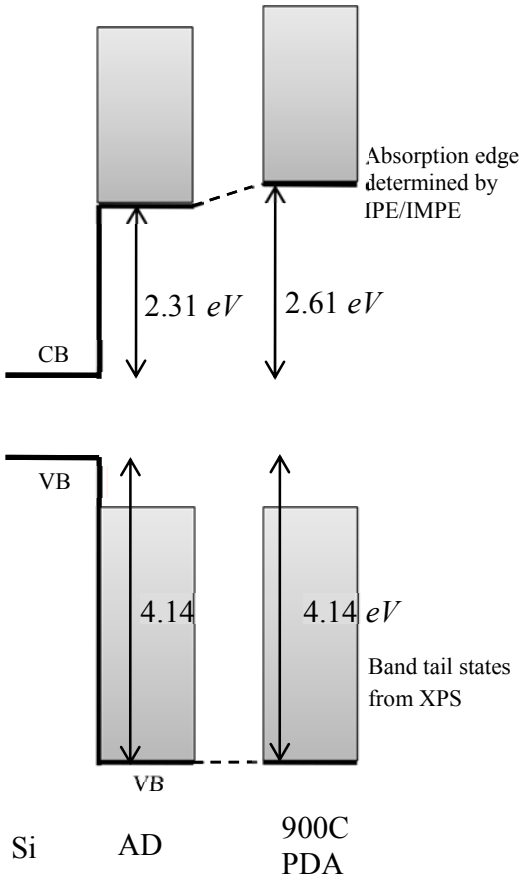

Figure 33: Schematic band diagram of the interface between Si and as-deposited (AD) and annealed BeO. The shaded grey area in the CB denotes possible band tail states above the absorption edge probed by IPE/IMPE.

3.4 SUMMARY

In this chapter, we presented measurements of the CBO and VBO of ALD Al_2O_3/Si(100), HfO_2/Si(100), and BeO/Si(100) before and after annealing using IPE (for films thicker than 10 nm), IMPE-EFISH (for films thinner than 10 nm), and XPS. Al_2O_3/Si(100) serves as a control sample for which previous band offset measuremtns were available. We compared the CBO of ALD Al_2O_3/Si(100) determined by IPE and IMPE, and found that they agree consistently with each other and with previous measurements for annealed samples. For Si/HfO_2, we found a PDA-induced valence band offset variation due to gettering of atomic oxygen away from the interfacial oxide region to passivate intrinsic O-vacancy defects in bulk HfO_2. Finally, we measured band alignment of ALD BeO on Si by internal photoemission and XPS. IPE and IMPE both yielded consistent results for the CBO of as-deposited BeO/Si(100) samples, although the IPE/IMPE threshold may be determined by CB tail states. The CBO increased with PDA temperature, indicating a change in the interfacial atomic structure during thermal treatment. The VBO, as determined by synchrotron XPS, is consistent with the CBO measured by IPE/IMPE and the optical absorption edge measured by SE.

Chapter 4: CHARACTERIZATION OF ANTI-PHASE BOUNDARIES IN HETERO-EPITAXIAL POLAR-ON-NONPOLAR SEMICONDUCTOR FILMS

Compound semiconductor layers (*e.g.* GaAs) grown on elemental semiconductor substrates (*e.g.* Si, Ge) are vulnerable to formation of anti-phase boundary (APB) defects. Optical second-harmonic generation (SHG) in reflection from polar epi-layers with APBs is shown to be as much as 1000 times weaker than from control layers without APBs. Moreover, scanning SHG images of APB-rich layers reveal microstructure lacking in APB-free layers. These findings are attributed to the reversal in sign of the second-order nonlinear optical susceptibility $\chi^{(2)}$ between neighboring anti-phase domains. Thus contributions to SHG from neighboring domains within the incident laser spot interfere destructively, weakening the SHG signal and making it sensitive to lateral position. The results are correlated with other metrologies[1], which show that SHG can identify APBs quickly and non-invasively for advanced MOSFET device applications.

4.1 EXPERIMENTAL PROCEDURE

Several hetero-epitaxial III-V compound semiconductors are examined by SHG and correlated with other metrologies in order to identify the contribution of specific defects to SHG signal. Two sets of samples were thoroughly studied: Sample set 1) $In_xGa_{(1-x)}As$ films with different In molar ratios epitaxially grown on GaAs substrates, to study the threading dislocations (TDs); Sample set 2) GaAs films gown hetero-epitaxially on various elemental substrates in order to investigate anti-phase boundaries (APBs). The result from each sample was compared to a control consisting of a GaAs film grown

[1]Due to the extra lengthy clearance requirement of public disclosure of data measured by SEMATECH, the data is not shown in this treatise. For more info regarding III-V Epi samples and XRD results, please contact Jimmy Price (jimmy.price@sematech.org). For TEM data, please contact P. Y. Hung (PY.Hung@sematech.org).

homo-epitaxially on GaAs. All epitaxial growths were carried out by molecular beam epitaxy (MBE) by Man Hoi Wong from SEMATECH. The specifications of epi-$In_xGa_{(1-x)}As$ samples are listed in Table 3. The indium content is varied in order to introduce lattice mismatch between the epi-film and the GaAs substrate. This lattice mismatch will result in dislocations within the epi film in proportion to the larger lattice constant with increased indium mole fraction. TDs are the only type of structural defect in these samples.

2043	2044	2045	2046	2068	2069
1 μm GaAs on GaAs	1 μm InGaAs (30% In)on GaAs	1 μm InGaAs (8~9% In) on GaAs	1 μm InGaAs (10~11% In) on GaAs	1 μm InGaAs (6.4% In) on GaAs	1 μm InGaAs (5.4% In) on GaAs

Table 3: Specifications for Sample Set 1 --- $In_xGa_{(1-x)}As$ on GaAs.

#1	#2	#3	#4	#5	#6
500 nm Epi GaAs/(001)Si substrate with 4^o off-cut angle	500 nm Epi GaAs/on-axis (001)Si substrate	500 nm Epi GaAs/(001) GaAs substrate	500 nm Epi GaAs/(001) Ge substrate with 6^o off-cut angle	500 nmEpi GaAs/on-axis (001) Ge substrate	500 nm HT-GaAs/100 nm LT-GaAs/1 nm AlAs/(001) Si substrate

Table 4: Specifications of Sample Set 2 --- GaAs on various elemental semiconductor substrates

The specifications of epi GaAs films on various elemental semiconductor substrates are listed in Table 4. For these samples, both TDs and APBs are present for on-axis substrates.

RA-SHG measurements were carried out by irradiating sample with *p*-polarized ~150 fs optical pulses (200mW incident power, 76 MHz repetition rate) from a mode-locked Ti:sapphire laser with wavelength λ = 775 nm focused at 45^o incident angle to a 30 μm diameter spot on the sample mounted on an azimuthal rotational stage. The reflected *p* or *s*-polarized SH signal was detected as the sample rotated around the surface normal. In order to provide more spatial distribution information of APBs, scanning SHG mapping of the surface were acquired with the same laser focused to a smaller spot (~2 μm in diameter, 45^o incident) while the sample raster-scanned in 1 μm steps within a plane perpendicular to the surface normal, with azimuth fixed a maximum of RA-SHG. The surface morphology was evaluated by SEM from a FEI Strata DB235 electron microscope operated at 3 kV.

4.2 DISLOCATIONS

When two crystalline materials with dissimilar lattice constants bond, their lattice mismatch must be accommodated by strain (deformation of crystal structure), dislocation formation or a combination of both in order to minimize the system energy. Since the strain energy builds up with increased film thickness, below the critical thickness --- *i.e.* the maximum thickness for which pseudomorphic growth occurs (10~20 nm for InGaAs on GaAs [72], and ~2 nm for GaAs on Si [73]) ---, the deposited crystalline film is stretched (when the lattice constant of the film is smaller than the substrate, *i.e.* $a_f < a_s$) or compressed (if $a_f > a_s$), as shown in Figure 34. This deformation causes displacements of atoms within the solid volume. According to linear elasticity theory [68], the strain

energy density (energy per unit volume) u associated with this lattice deformation scales approximately quadratically with stress: $u \propto E\varepsilon^2$, where E is the modulus.

Beyond the critical thickness, dislocations can occur to relax strain. An edge dislocation at the hetero-interface is depicted in Figure 35.

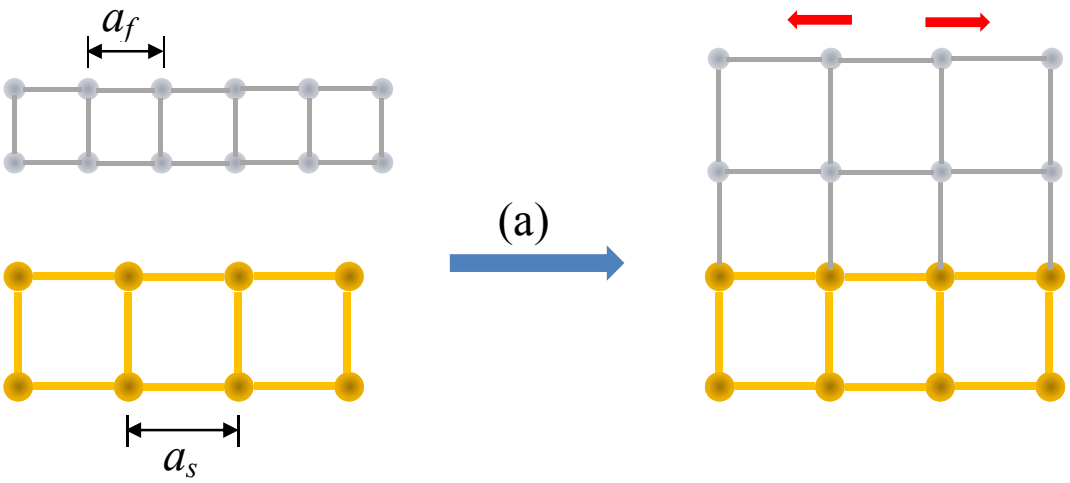

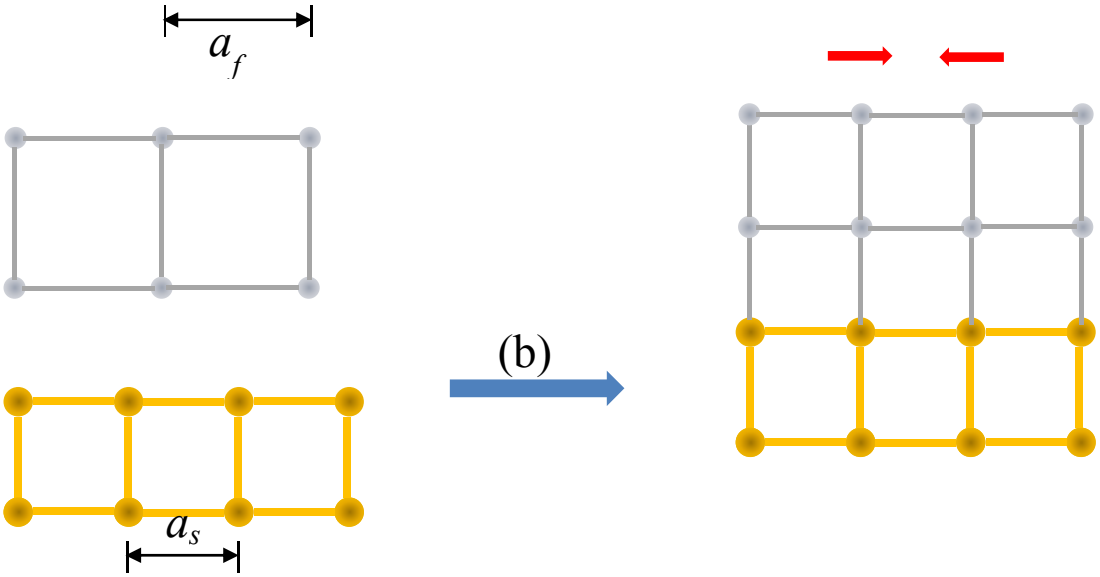

Figure 34: Deformation of the crystal structure of the film under critical thickness when the lattice constant is distinct from the substrate.

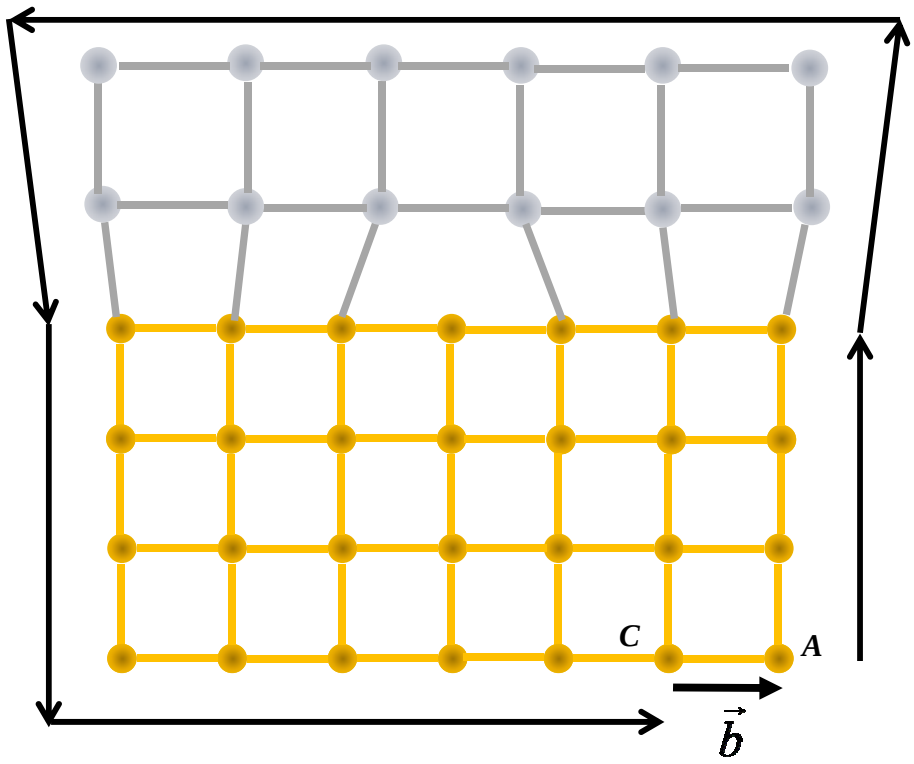

Figure 35: Edge dislocation and the corresponding Burger's verctor.

Dislocations can be characterized topologically by a Burger's vector, defined as follows: consider a loop encompassing the dislocation site, then traverse the same sequence of Bravais lattice displacements in opposite directions. If the endpoint doesn't coincide with the starting point, the vector joining these two points is called the Burger's vector associated with the dislocation encompassed within this loop. As illustrated in Figure 35, the loop starts from site point *A*, and ends at point *C* which fails to return to the starting point, so the Burger's vector corresponding to the edge dislocation within this

loop is defined by the vector joining point *C* and *A*. For a perfect crystal without any dislocation, a closed loop is expected.

Dislocations can be helpful for the growth of lattice mismatched materials. Edge dislocations are especially preferred because they are localized at the hetero-interface, and are most energetically efficient for strain relaxation. The commonly occurring dislocations can be classified into two groups according to the angle between Burger's vector and growth interface: parallel and non-parallel. The first one is called Type I dislocation (an edge dislocation is an example). And the other one is called Type II. Type II dislocaitons are detrimental, because they can propagate towards the top surface and degrade the overlaying device performance and reliability. One example is the threading dislocation with dislocation line inclined to the growth interface (60° for the case of hetero-epitaxy of GaAs on Si). Higher resolution X-ray diffraction (HRXRD) is usually used to characterize dislocations within a crystalline material. The full width at half maximum intensity (FWHM) of the rocking curve --- where the detector is fixed at the center of the expected Bragg reflection and the sample is independently rotated or rocked ---, is directly related to the dislocation density by $D = \frac{\beta^2}{4.36b^2}$, where β is the FWHM (radian) and b is the magnitude of Burger's vector: $b = a/2 \langle 110 \rangle$ for diamond structure crystals [69].

For $In_xGa_{(1-x)}As$ alloy, the lattice constant *a* is known to obey Vegard's law [70] well, *i.e.* to vary linearly with the composition[71]. Thus the lattice constant of the ternary alloy is $a_{In_xGa_{1-x}As} = x \times a_{InAs} + (1-x) \times a_{GaAs}$, where for the compositional binary $a_{InAs} = 6.0584\text{Å}$, $a_{GaAs} = 5.6533\text{Å}$. For sample set I listed in Table 3, up to 2% lattice mismatch can be achieved. So the dislocation density can be controlled by changing the composition of In. A 4- to 5-fold broadening of the XRD rocking curve was observed:

~200 to 900 arc sec (results measured by Jimmy Price from SEMATECH will published elsewhere), as In content which indicates the existence of significant amount of dislocation within these samples (10^8~10^9 cm^{-2}). This was confirmed by a recent HRTEM measured by Kathy Dunn and P. Y. Hung from SEMATECH. On the other hand, there is very minor differences among the SHG responses of sample with widely varying TDDs, as indicated in Figure 36 and 37 and via the integrated SH intensities ($\int I^{(2\omega)}(\phi)d\phi$) listed in Table 5.

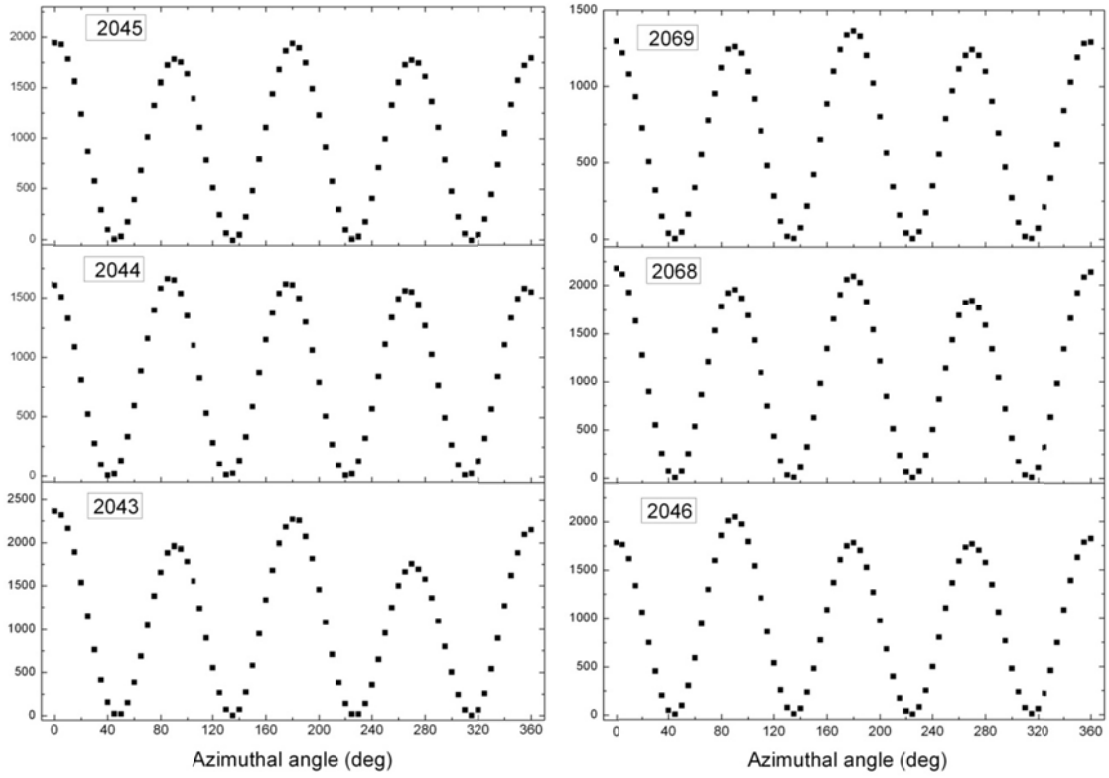

Figure 36: RA-SH results from sample set I under P_{in}/P_{out} configuration with fundamental center wavelength 775 nm, incident power 200 mW.

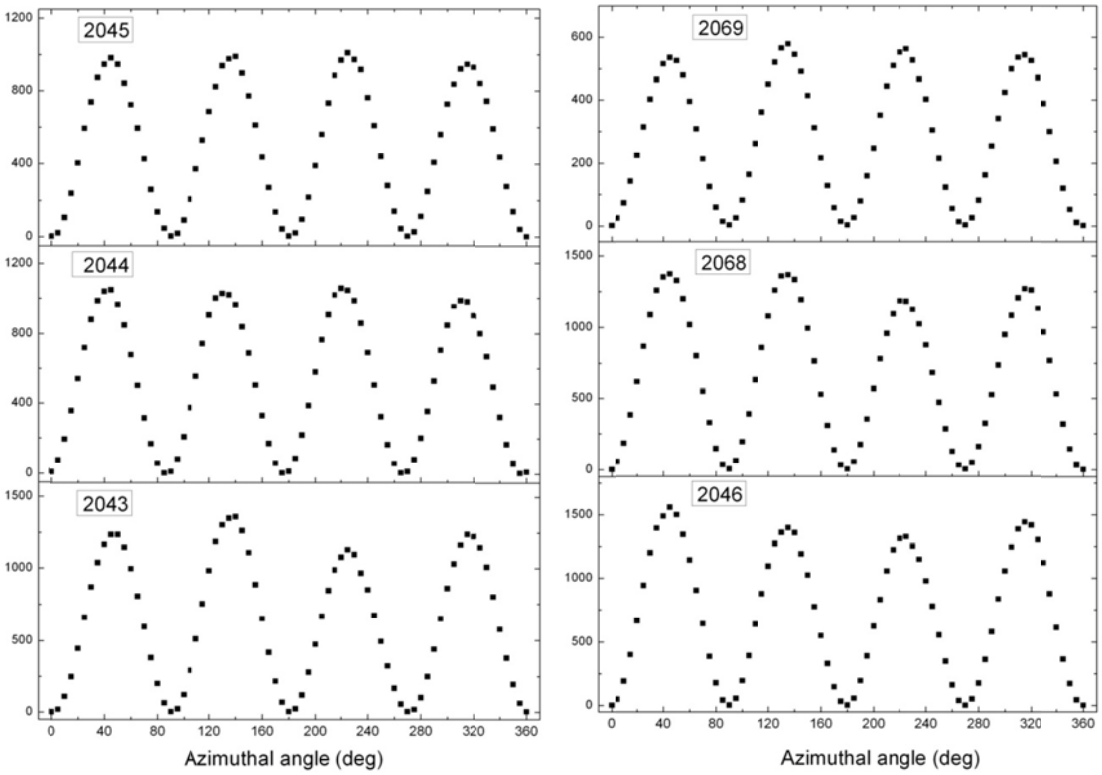

Figure 37: RA-SH results from sample set I under P_{in}/S_{out} configuration with fundamental center wavelength 775 nm, incident power 200 mW.

	2043	2044	2045	2046	2068	2069
	1 μm GaAs on GaAs	1 μm InGaAs (30% In)on GaAs	1 μm InGaAs (8~9% In) on GaAs	1 μm InGaAs (10~11% In) on GaAs	1 μm InGaAs (6.4% In) on GaAs	1 μm InGaAs (5.4% In) on GaAs
Integrated SH signal (P_{in}/P_{out})	7.58×10^4	5.91×10^4	6.78×10^4	6.77×10^4	7.38×10^4	4.73×10^4
Integrated SH signal (P_{in}/S_{out})	4.53×10^4	3.77×10^4	3.55×10^4	5.20×10^4	4.74×10^4	2.00×10^4
TDD (cm^{-2})	N/A	2.89×10^9	3.77×10^8	5.4×10^8	3.9×10^8	1.8×10^8

Table 4: Summary of SHG results for $In_xGa_{(1-x)}As$ on GaAs.

This result suggests that SHG is insensitive to dislocations. Thus we can rule out the any substantial contribution to SHG from TDs in the study of APB defects.

4.3 ANTI-PHASE BOUNDARIES

Sample set II --- *i.e.* epi GaAs on various elemental substrates (see Table 4) --- was used to study the effect of APBs on SHG. APBs owe their origin to the unavoidable presence of single-atomic-height steps at the (001) surfaces of elemental (nonpolar) semiconductors (Si, Ge). Hence when a polar semiconductor is grown hetero-epitaxially on a nonpolar semiconductor substrate, the positions of cation and anion interchange in neighboring anti-phase domains (APDs) originating on opposite sides of a single-atom step, as shown in Figure 38, resulting in undesirable Ga-Ga and As-As bonds at the APBs. Although APB-free growth can be achieved by mis-orienting the substrate, in

which case double-atomic-height steps are energetically favored[74], growth on exact (001) planes is of the greatest technological importance.

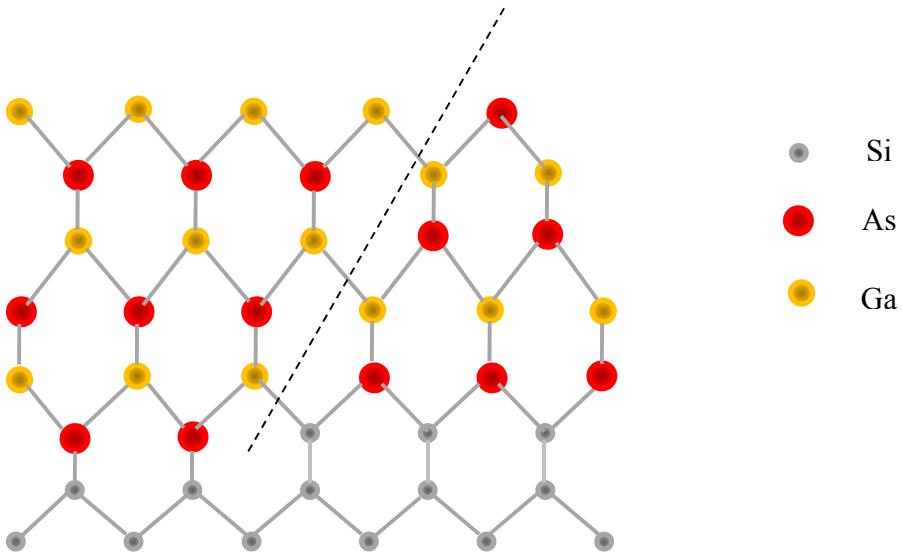

Figure 38: Schematic bonding diagram for the formation of APB defect.

Thus one type of domain is the spatial inverse of the other. For crystals like GaAs, which does not lack centrosymmetry, this will change the sign of the 2nd order nonlinear optical susceptibility between the two types of domains. For noncentrosymmetric cubic crystals, the only nonzero dipolar susceptibility is $\chi_{ijk}^{(2)}$, $i \neq j \neq k$.[75] The absorption coefficients α^{-1} of fundamental (775 nm) and SH (387.5 nm) radiation in GaAs are 677 nm and 13 nm, respectively [38], so SHG only probes the very top of typical micro-thick GaAs epilayer. Within an area defined by the laser spot size S, suppose there are N_1 of one type of domain with average size $\langle S_1 \rangle$, and N_2 sublattice reversed domains with average size $\langle S_2 \rangle$, *i.e.* $S = N_1\langle S_1 \rangle + N_2\langle S_2 \rangle$. The SHG signal is a coherent

superposition of signals from each individual domain enclosed in this area, so the effective nonlinear susceptibility can be written as:

$$\tilde{\chi}_{ijk}^{(2)} = \frac{\chi_{ijk}^{(2)}}{S}(N_1\langle S_1\rangle - N_2\langle S_2\rangle) = \chi_{ijk}^{(2)}(1-2\frac{N_1}{S}\langle S_1\rangle) = \chi_{ijk}^{(2)}(1-2n_1\langle S_1\rangle) \qquad (15).$$

For P_{in}/S_{out} configuration, the reflected SH intensity from an arbitrarily oriented GaAs surface can be written as[76] :

$$I^{(2\omega)}(\phi) \propto \left|\sum_{n=1}^{4} \tilde{\chi}_{ijk}^{(2)} F_n^{(2\omega)}[\Phi_{n,1}^{(2\omega)}(\alpha,\beta)\cos(n\phi) + \Phi_{n,2}^{(2\omega)}(\alpha,\beta)\sin(n\phi)]\right|^2, \qquad (16)$$

where $F_n^{(2\omega)}$ are the Fresnel factors specific to each Fourier coefficient and $\Phi_{n,1}^{(2\omega)}$ and $\Phi_{n,2}^{(2\omega)}$ are the geometric factors associated with the mis-orientation of the surface. The latter are all real for 775 nm fundamental radiation[76]. The integrated intensity from the RA-SHG pattern as depicted in Figure 39, gives an azimuthal angle independent quantity $\bar{I}^{(2\omega)} = \int_0^{2\pi} I^{(2\omega)}(\phi)d\phi$. For off-cut angle up to 6°, the effect of mis-orientation on this integral value is less than 3%, so $\bar{I}^{(2\omega)} \propto |\tilde{\chi}_{ijk}^{(2)}|^2$ for all samples. Compared to SHG from control sample (GaAs/GaAs) from which the signal is generated from one single domain, the normalized SH signal gives:

$$\bar{I}^{(2\omega)} / \bar{I}_0^{(2\omega)} = (1-2n_1\langle S_1\rangle)^2. \qquad (17)$$

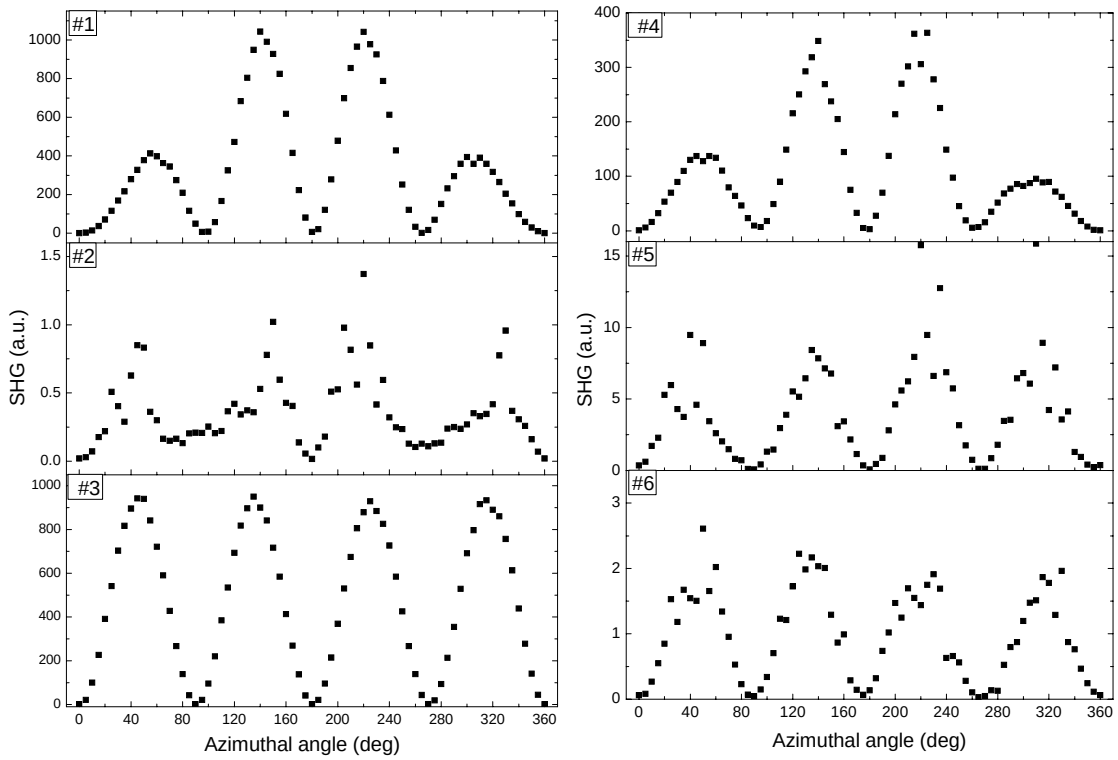

Figure 39: RA-SHG from all Epi GaAs samples listed in Tables 4 and 5 under P_{in}/S_{out} configuration.

	#1	#2	#3	#4	#5	#6
Normalized integrated SHG intensity	0.74	7.8×10^{-4}	1	0.24	7.7×10^{-3}	2.4×10^{-3}
Roughness/nm	1.8	1.7	0.90	16	5.8	1.0
TDD /cm^{-2}	5.5×10^{9}	10^{9}	N/A	2.4×10^{7}	2.5×10^{8}	8×10^{9}

Table 5: Integrated intensity of RA-SHG from Figure 38 for six GaAs epi-films on various elemental substrates, as-specified in Table 4, showing that integrated SHG intensity is uncorrelated with roughness and TDD.

As indicated by the normalized SH intensity in Table 5, GaAs grown on exactly (001) plane yields roughly 3 order of magnitude weaker signal compared to the control sample. This indicates the existence of APB with comparable total area share, *i.e.* $n_1\langle S_1\rangle \to 0.5$, which leads to the significant degradation of SHG signal. Dislocations contribute negligibly to this weakness of SHG based on cross sectional TDD density measured by HRTEM. The effect of surface roughness can also be ruled out, especially for sample #6 with very smooth surface.

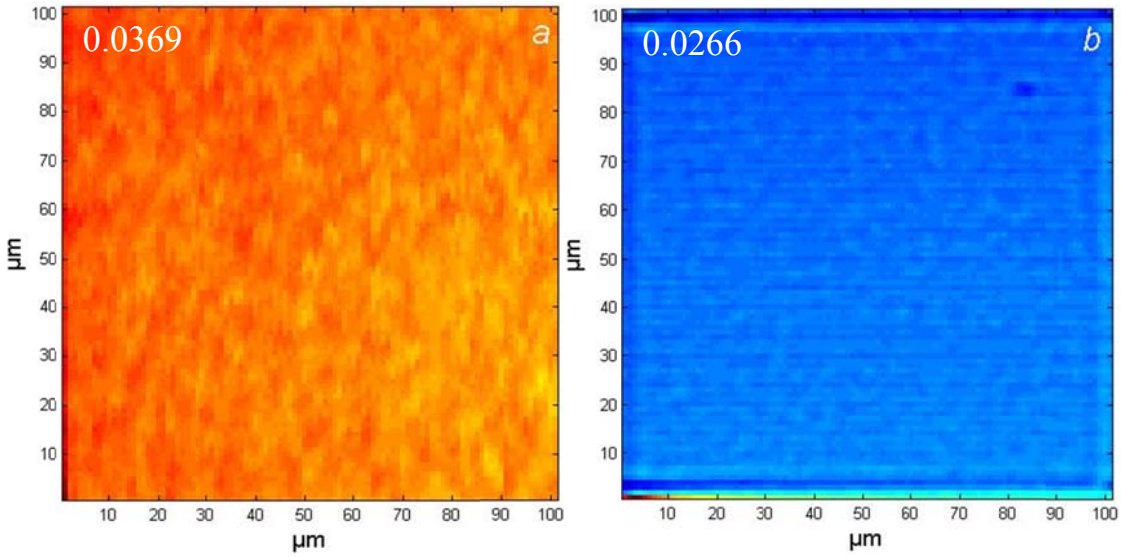

Figure 40: Scanning SH images from sample #1(a), #3 (b), #5 (c) and #6 (d), as specified in Table 4. The number on the top left corner is the normalized standard deviation of SHG intensity. The horizontal axis is along <100> direction.

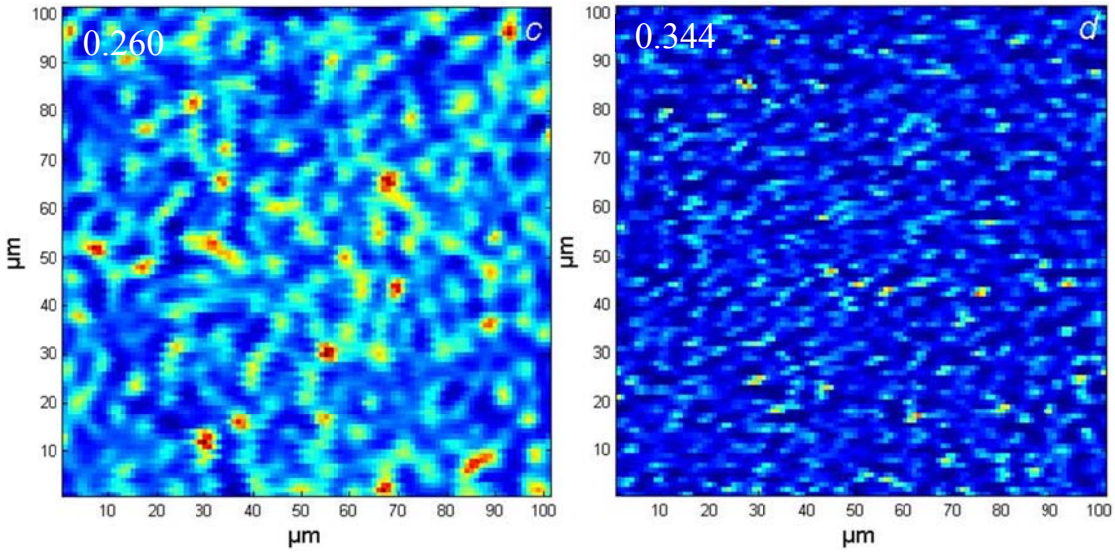

Figure 40 (continued): Scanning SH images from sample #1(a), #3 (b), #5 (c) and #6 (d), as specified in Table 4. The number on the top left corner is the normalized standard deviation of SHG intensity. The horizontal axis is along <100> direction.

To obtain more physical insight about APB distribution, scanning SH images were taken as presented in Figure 40. Compared to almost featureless images from control sample and GaAs/off-cut Si (panels (a) and (b)), the prominent features in (c) and (d) are associated with APBs. The contrast is due to the mutual annihilation of SH signal from different types of domains. The degree of contrast is quantified by the normalized standard deviation, indicated in the upper left corner of each panel of Figure 39, which is larger for images with higher contrast and thus worse crystalline quality. Thus the 'bright' regions indicate the dominance of one type of domain, and the 'dark' regions suggest comparable area of both types of domains.

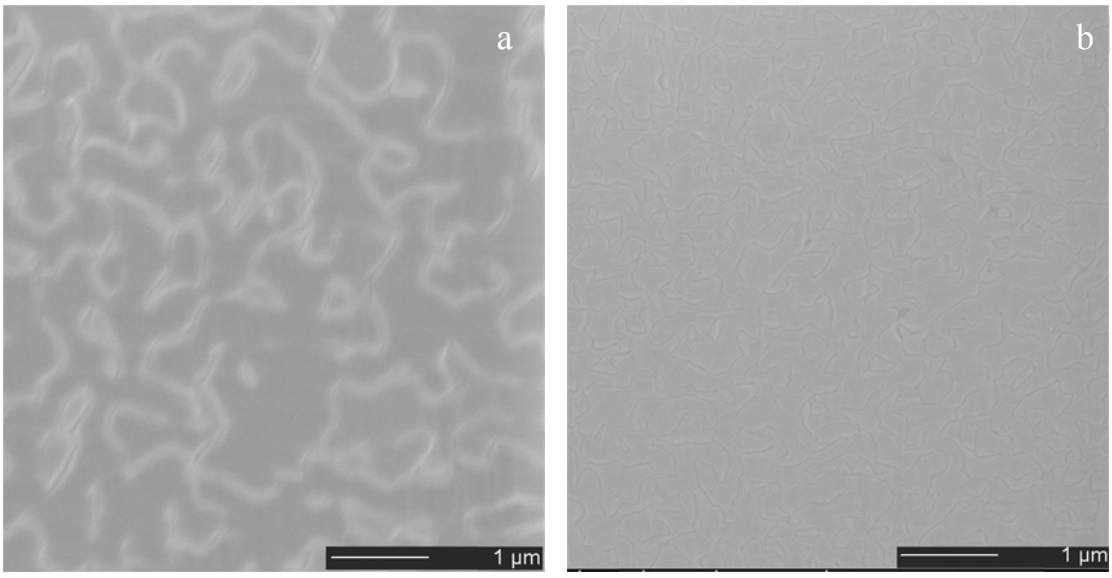

Figure 41: SEM micrograph of surface morphology of APB defects from sample #5 (a) and #6 (b). See Table 4 for the structures of these samples.

Further correlation between SHG and APB can be inferred from the correspondence of structures in the SHG images with domain size by comparing SEM micrographs in Figure 41. The irregular features in the latter are signatures of APB morphology [77, 78]. The control sample and GaAs on off-cut substrate yield featureless images, as did scanning SHG.

The correlation of SHG with the presence of APBs is further confirmed by data from commercial grade high electron mobility transistors (HEMTs) fabricated on (001)Si substrate with either 0° and 4° off-cut angle. Figure 42 shows the compositional cross section of these samples, which were fabricated by IntelliEpi Inc.

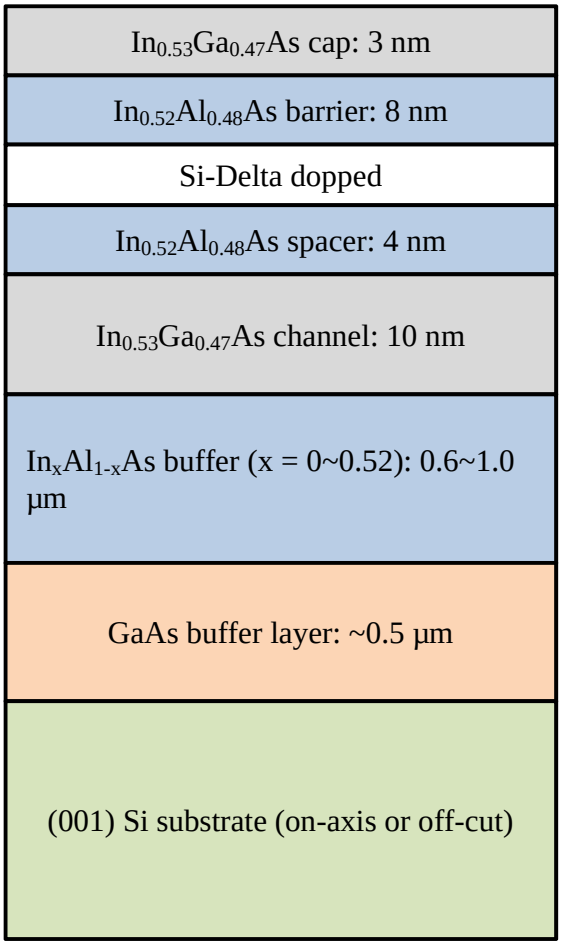

Figure 42: Schematic cross section of commercial grade HEMT structure purchased from IntelliEpi Inc for SHG studies.

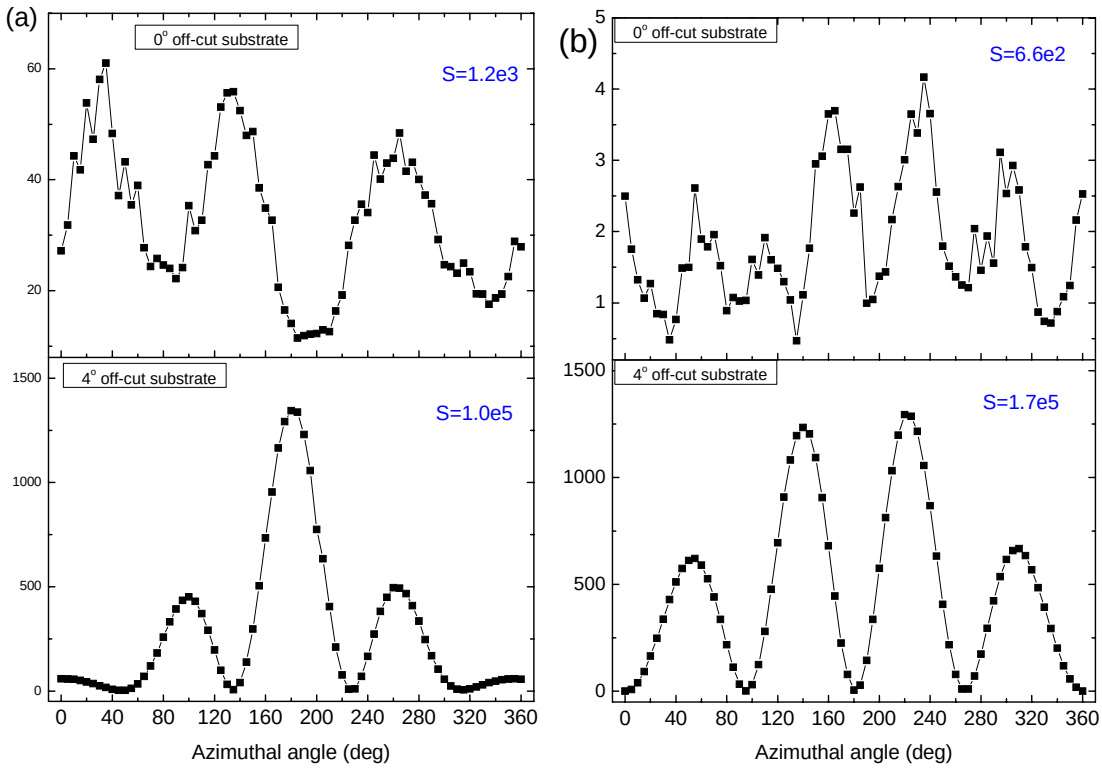

Figure 43: RA-SHG from HEMT samples defined in Figure 42 P_{in}/P_{out} (a) and P_{in}/S_{out} (b) configuration. The number in blue indicates the integrated SH intensity.

The HEMTs have much higher electron mobility than the conventional FETs because of the undoped channel region where electrons can move very fast without collision with the ionized impurities. Conductive electrons are supplied by the neighboring highly doped larger bandgap layer ($In_{0.52}Al_{0.48}As$ in this case). The SH intensity from the on-axis substrate behaves similarly to that for simpler GaAs epi-film in Figure 39 and Table 5 --- about 3 order of magnitude weaker than for the off-cut substrate. This result is also consistent with the SEM micrographs which suggest the presence of APB defects on the on-axis sample, as shown in Figure 44. The RA-SHG patterns for the off-cut substrate for P_{in}/S_{out} polarization (Figure 43b, lower panel) closely

resembles that observed for corresponding samples #1 and #4 in the earlier data (see Figure 39). However the P_{in}/S_{out} data for the oriented substrate (Figure 43b, upper panel) shows a 6-fold symmetry rather than 4-fold symmetry from previous data (see samples #2 and #5 in Figure 39).

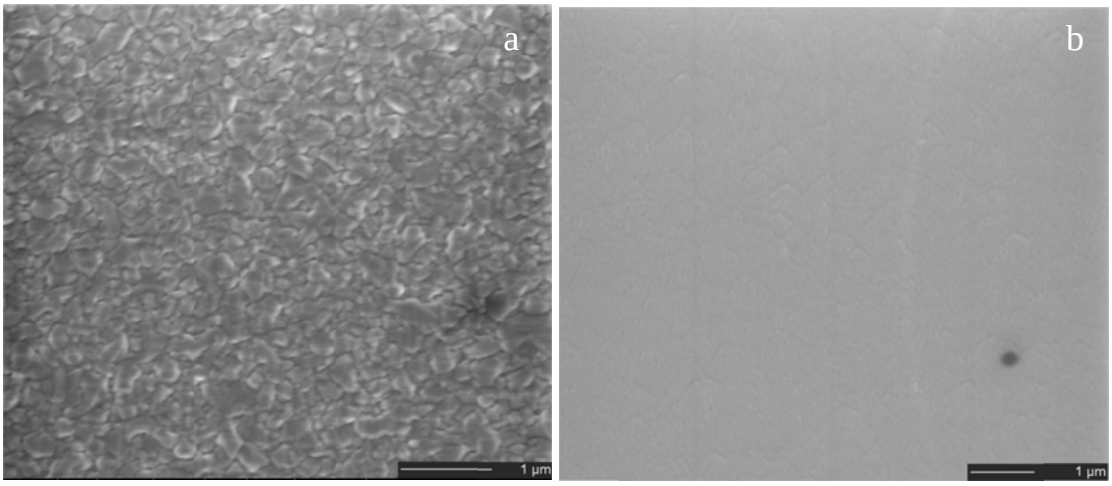

Figure 44: SEM micrograph of APB defects from HEMT samples with 0° (a) and 4° (b) off-cut substrate.

4.4 SUMMARY

In this chapter, we have demonstrated SHG as an efficient and non-invasive metrology to evaluate the crystalline quality of epitaxial GaAs layers grown on different substrates. A significant degradation of SHG signal is attributed to the APB structural defects which are detrimental to the performance of devices fabricated on the top epilayer. Thus SHG distinguishes itself as a non-destructive, *in-situ* and potentially in-line diagnostic for those performance limiting defects for advanced FET device application.

Chapter 5: CHARACTERIZATION OF STRAIN FIELD IN TSV BY OPTICAL SHG

The ITRS has announced 3D integration to be a key technique for higher transistor integration density. Among all the 3D integration designs, TSV is considered as the most promising technology for interconnecting stacked devices. In addition to the current effort focused on the system design and processing development, thermal mechanic reliability challenges due to the large CTE mismatch between TSV filled metal and Si, need to be investigated thoroughly. In this chapter, we show preliminary SHG results to probe the strain distribution around TSV patterns. Different SH imaging techniques are used to explore optimal sensitivity to strain field, and the oblique incident angle scanning SH images suggest a strong correlation to strain distribution.

5.1 EXPRIMENTAL PROCEDURE

The test sample was fabricated by the standard TSV process [84]. Deep trenches (~60 μm) inside the Si wafer were fabricated by reactive ion etch (RIE), then an insulation layer (SiO_2) was deposited on the side walls by PECVD. Electro-plating of circular Cu wires with radius ~10 μm was used to fill the hole followed by chemical mechanical polish (CMP). The geometry of the resultant TSV structure is presented in Figure 45 and Figure 46.

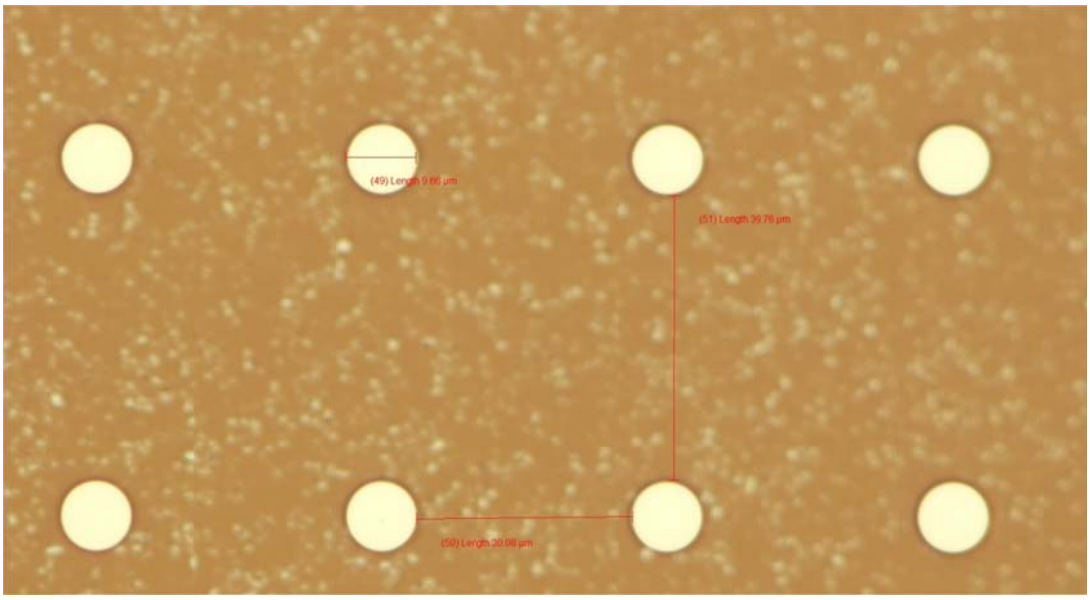

Figure 45: Optical microscope image for the top view of TSV array.

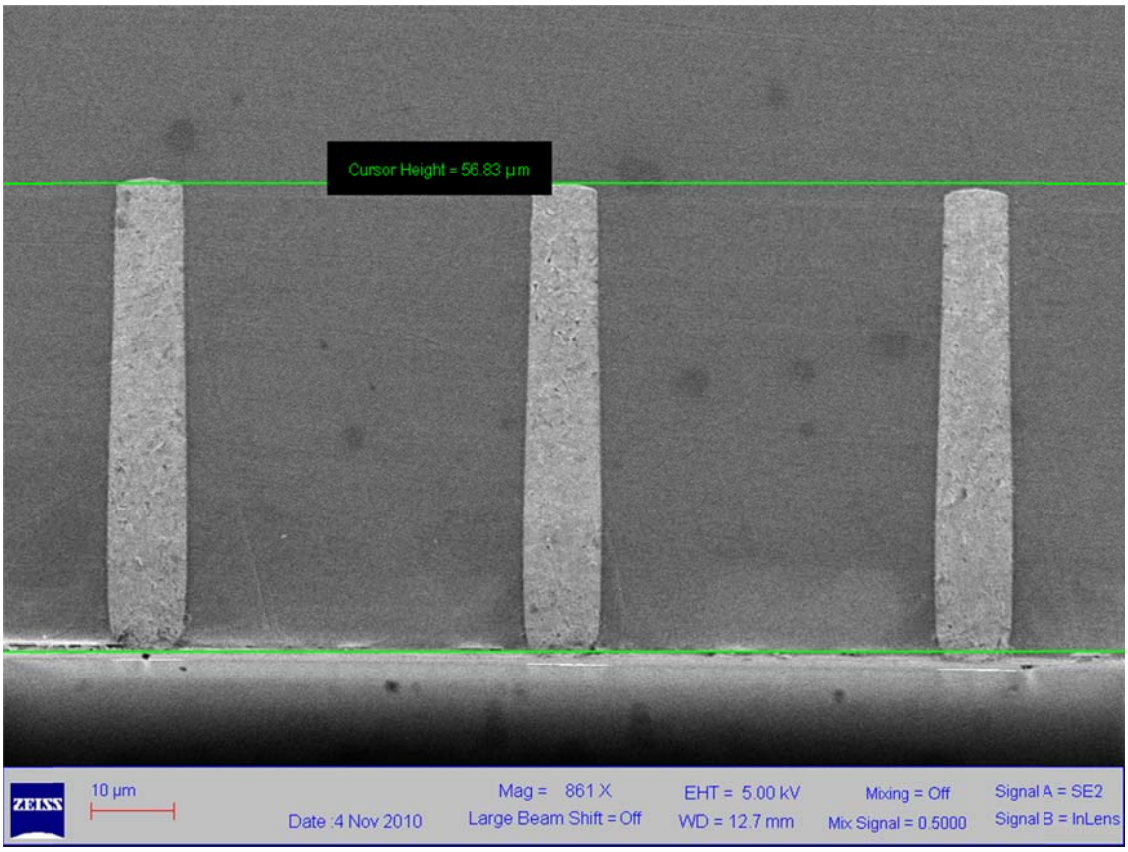

Figure 46: SEM micrograph of the cross section of TSV structure.

Several different SH imaging techniques were used to study the strain field within the Si wafer around TSV patterns: projection imaging, confocal and oblique incident angle scanning microscope. Projection imaging has the simplest setup layout: a fairly large beam (50 µ diameter spot size) was focused on to the sample at 45° incident angle, and the reflected beam was projected on to a CCD camera by a microscope objective (0.42 NA, 10 mm FL).[80] For the last two scanning microscopes, different scanning techniques were used. In the confocal configuration, the sample is kept fixed while the normal incident laser beam is scanning by a pair of Galvo mirrors[80]. For the last scanning microscope configuration, the sample is scanning at 1 µm step in a raster

manner while beam is stationary in order to achieve oblique incidence[81], similar to the technique used to obtain scanning SHG images of APB-laden GaAs epi-films in the previous chapter (see Figure 40).

5.2 PROJECTION SH IMAGING

Figure 47 shows the projection SH images acquired with 50 seconds exposure time at different fundamental wavelengths with 200 mW incident power. A clear feature of these images is the interference fringes near the sharp edge between Cu and Si, which was reported also for the EFISH imaging of Au electrode on Si substrate. [80]

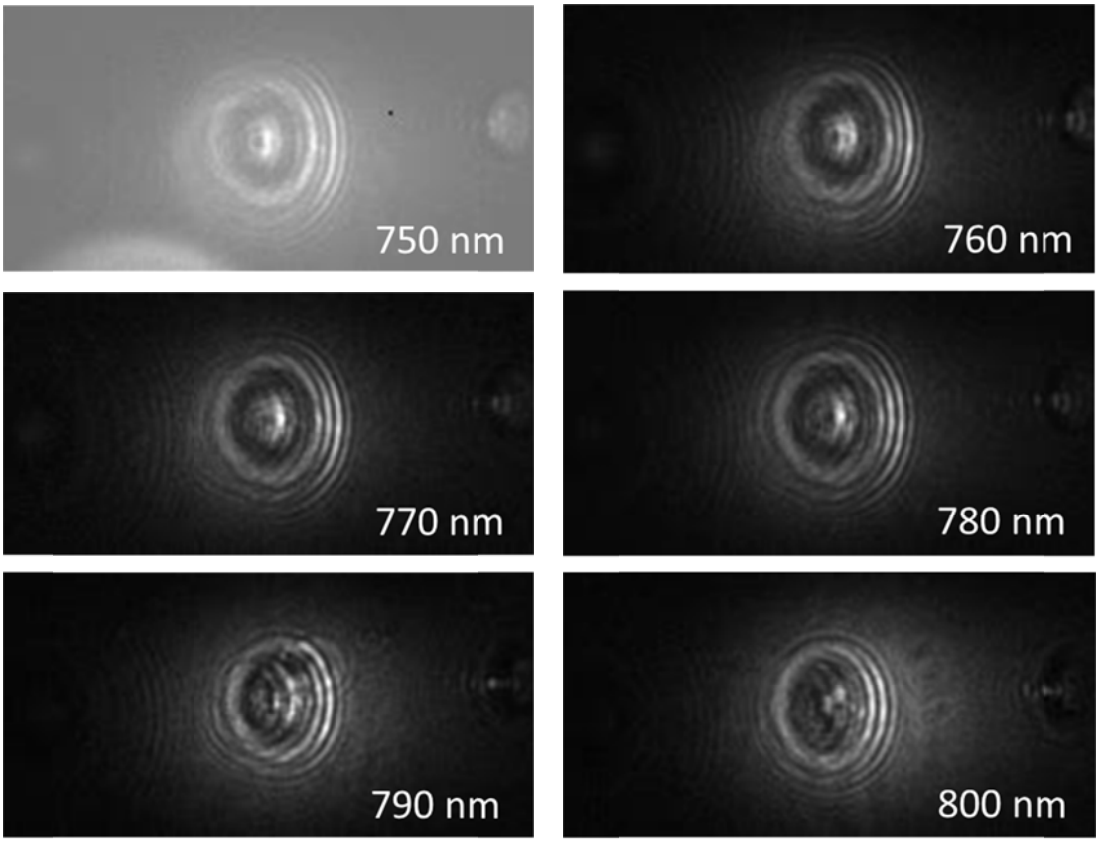

Figure 47: Projection SH images for different fundamental wavelengths at P_{in}/P_{out} configuration from a single TSV pattern.

The fringes near the sharp edge between Cu and Si are artifacts due to spatially coherent illumination, combined with wide-angle diffraction of light from these sharp edges outside the collection angle of the imaging optics. These fringes overlap the strained Si region, making the analysis of the strain-field-induced SHG rather cumbersome. Thus two different scanning SH microscopes were used to break the spatial coherence of SHG from different locations.

5.3 SCANNING SH IMAGING

During the scanning process, either the tightly focused beam or the sample is scanning in a raster manner. The coherence of SHG from different locations is broken by establishing a point-to-point relation between the sample and image. This offers a potentially more straightforward mapping of the strain field distribution by scanning SH imaging.

For the standard Leica TCS SP5 confocal microscope at Patterson Microscopy Center on campus, the scanning of the beam is achieved by a pair of Galvo mirrors which vibrate along perpendicular directions. Thus a 2-D scanning can be obtained for the laser beam whose geometry is limited to normal incidence. Figure 48 demonstrate the confocal scanning images obtained from TSV pattern.

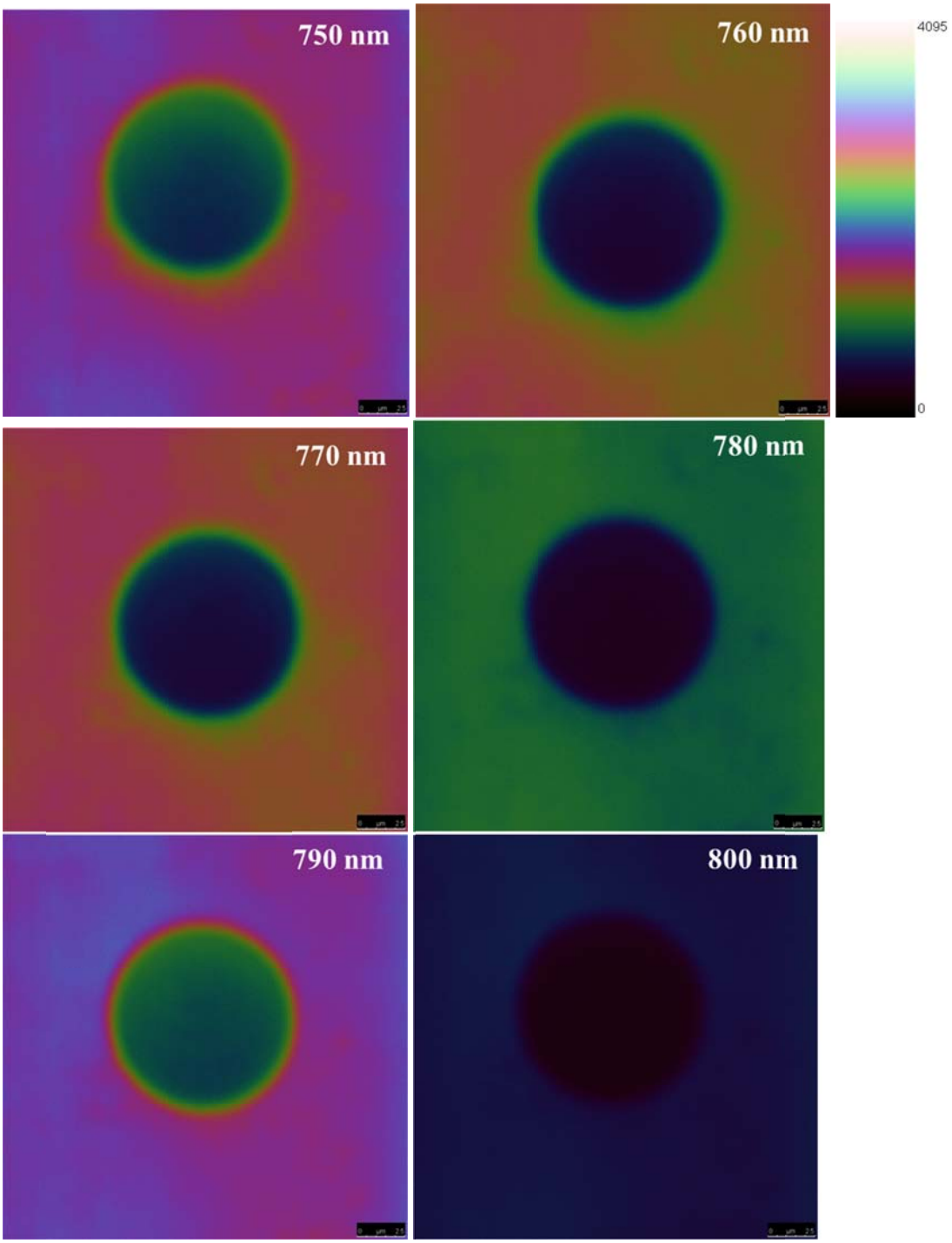

Figure 48: Confocal scanning SH images from TSV pattern with different fundamental wavelengths.

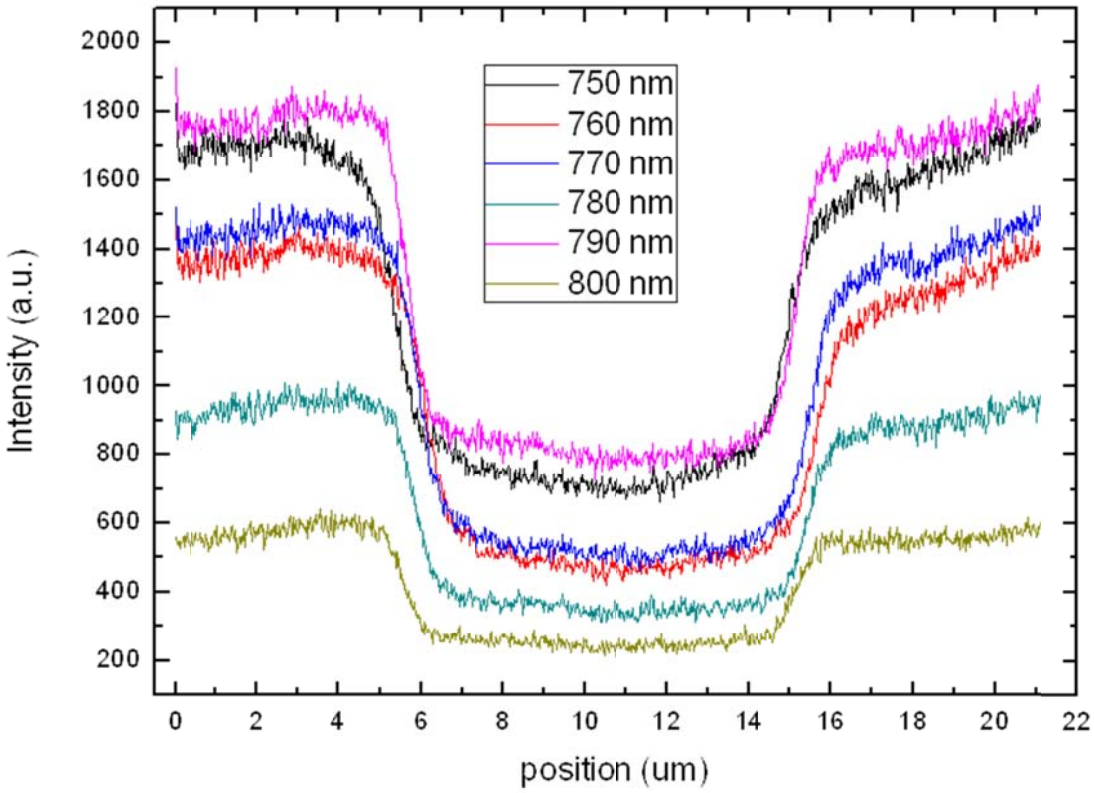

Figure 49: SH intensity along the radial direction from the images shown in Figure 48.

The confocal scanning images only demonstrate azimuthally isotropic distribution of SH signal around TSV and a monotonic gradual transition from Si to Cu along the radial direction as indicated by Figure 49. This may suggest that SHG is not sensitive to strain under normal incidence. Thus an oblique incident angle geometry may be required to explore any strain effect on SHG images.

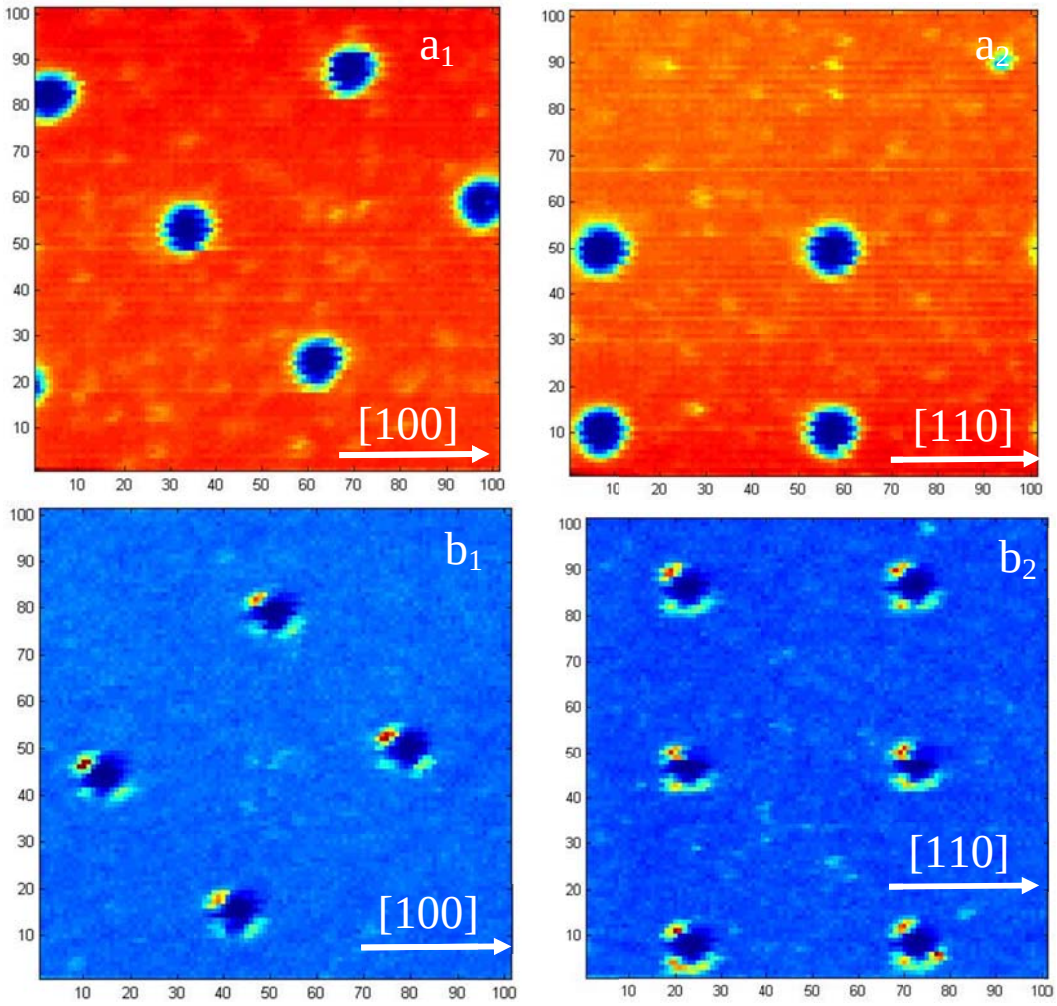

Figure 50: Oblique incident angle scanning SH images from TSV patterns at fundamental wavelength 775nm under P_{in}/P_{out} (a), P_{in}/S_{out} (b), S_{in}/S_{out} (c), S_{in}/P_{out} (d) polarization configurations. The arrow on the right corner indicates the Si crystallographic direction as well as the scanning direction. For the top 4 panels, the scanning is along [100] crystallographic direction, while the scanning for the bottom 4 panels is along [110] direction. The *p*-polarization is along horizontal axis for all images, and *s*-polarization is parallel to vertical direction.

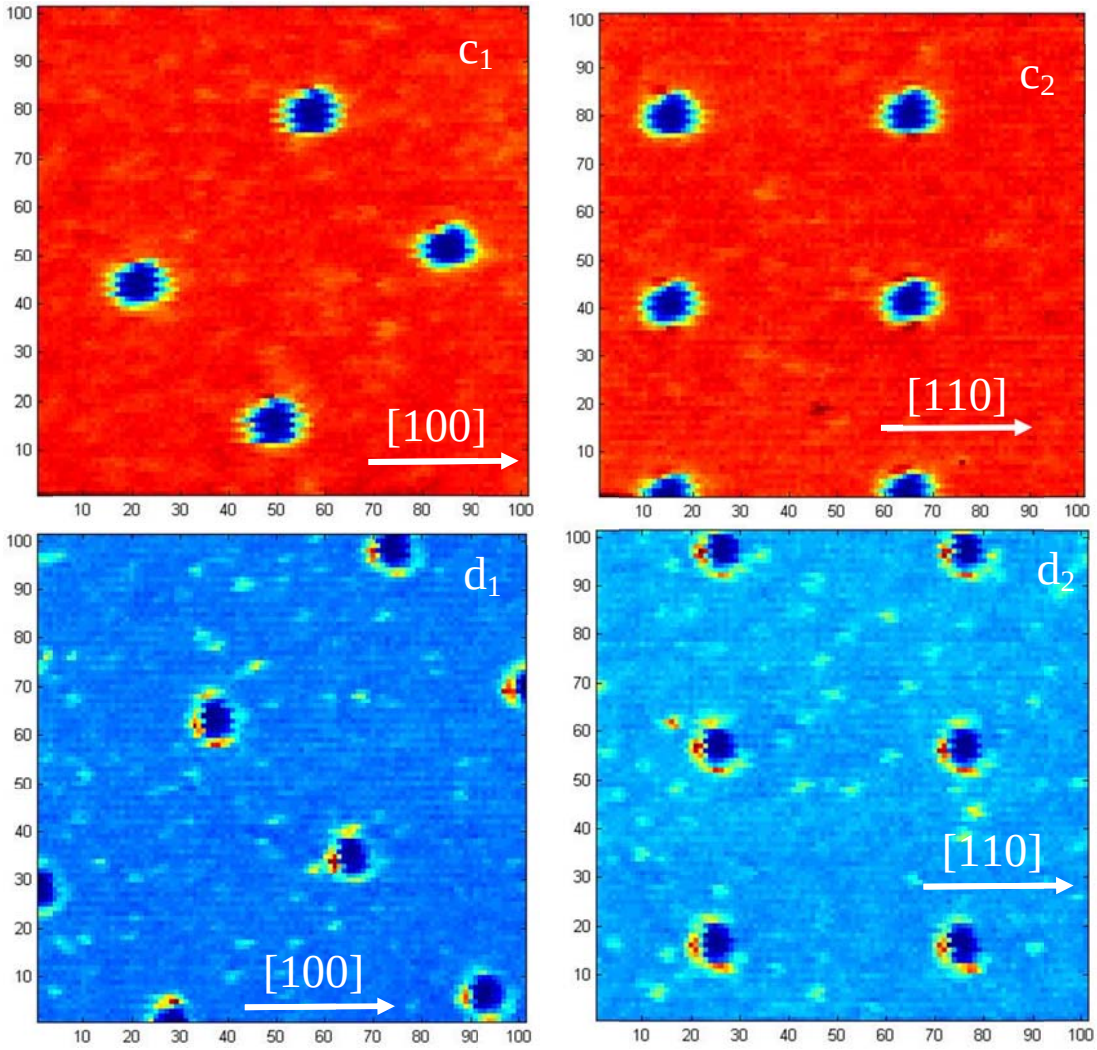

Figure 50 (continued): Oblique incident angle scanning SH images from TSV patterns at fundamental wavelength 775nm under P_{in}/P_{out} (a), P_{in}/S_{out} (b), S_{in}/S_{out} (c), S_{in}/P_{out} (d) polarization configurations. The arrow on the right corner indicates the Si crystallographic direction as well as the scanning direction. For the top 4 panels, the scanning is along [100] crystallographic direction, while the scanning for the bottom 4 panels is along [110] direction. The *p*-polarization is along horizontal axis for all images, and *s*-polarization is parallel to vertical direction.

Figures 50 show the scanning SH images from the TSV sample under different polarization configurations and scanning direction. The fundamental laser beam (775nm) was focused on a ~2μm spot at 45° incident angle, and the reflected SH signal was collected by a photo multiplier tube. Because of the oblique incident angle, the conventional beam scanning technique used in confocal configuration will not work. Thus during laser illumination, the sample was scanned two dimensionally in a raster manner in order to achieve the point-to-point mapping between the sample and the scanning image. An obvious observation is that for some polarization combinations (P_{in}/S_{out}, S_{in}/S_{out}, S_{in}/P_{out}), the region around the TSV pattern shows much higher SH signal than the background Si, and the bright patterns correlates closely with polarization combinations. Additionally these patterns tend to rotate with the laser beam (compare top and bottom data sets in Figure 50), thus ruling out any possibility of scattering from particles. These observations may indicate the correlation with strain field which may break the inversion symmetry of Si crystal around the TSV pattern. Especially the images obtained under P_{in}/S_{out} polarization combination as demonstrated in Figure 50b, exhibit a consistent spatial profile. The overall symmetry of strain induced SH intensity may be due to the polarization selectivity, in which case SH radiation follows a $\cos\phi$ angular relationship: $I^{(2\omega)}(\phi) \propto \cos^2\phi$, where ϕ is the azimuthal angle relative to *s*-polarization direction, *i.e.* the vertical axis. The asymmetry of SH intensity in the four quadrants may indicate the interference between the strain induced and the background SH signals. Further detailed model and analysis need to be developed in order to quantitatively explain the results, as well as correlation with simulation results [85, 86] and other metrologies [87, 88, 89].

Chapter 6: CONCLUSIONS AND FUTURE WORKS

6.1 SUMMARY

In conclusion, we have demonstrated SHG as an efficient, non-invasive metrology to characterize performance limiting defects and/or essential properties of novel materials for several current leading edge technologies in the microelectronic industry.

For SOI---the latest platform used in high performance/low power devices---, we have isolated the trapping dynamics of optically excited carriers at the buried Si/SiO_2 interface of ultrathin SOI layers, and measured their variation with SOI thickness and laser intensity (see Chapter 2). The results reveal that the dominant trapping sites are induced by thermal oxidation thinning of the SOI layer, and are thus denser for thinner films, and lie energetically at least 1 eV below the SiO_2 CB edge, and are thus long lived. The results demonstrate that SHG can noninvasively characterize defects critical to SOI device performance without device fabrication.

BeO is a promising interfacial passivation layer material. We have measured band alignment of ALD BeO on Si by internal photoemission and XPS (see Chapter 3). IPE and IMPE both yielded consistent results for the CBO of as-deposited samples, although the IPE/IMPE threshold may be determined by conduction band tail states. The CBO increases with PDA temperature, indicating a change in the interfacial atomic structure during thermal treatment. The VBO, as determined by synchrotron XPS, is consistent with the CBO measured by IPE/IMPE and the optical absorption edge measured by SE.

APB defects in epitaxial GaAs layers grown on nonpolar semiconductor substrates were evaluated by SHG (see Chapter 4). A significant degradation of average reflected SHG intensity compared to single-crystal GaAs, and appearance of micro-structure in scanning SH images, are attributed to APB structural defects.

Finally, scanning SH images may indicate the sensitivity of SHG to strain fields around TSV patterns (see Chapter 5). However, we are currently in need of a quantitative phenomenological model of the influence of strain gradients on SHG in order to understand the results in hand.

Thus SHG distinguishes itself as a non-destructive, *in-situ* and potentially in-line diagnostic of material properties important for both front-end-of-line and back-end-of-line of IC fabrication.

6.2 FUTURE WORK

So far the study of SHG from these novel materials for advanced device applications has been focused on two aspects based on the unique nonlinear optical property of specific material: IMPE (Chapter 2 and 3) and crystal symmetry (Chapter 4 and 5). IMPE-TDSHG has been widely applied to Si based systems, but there still lacks systematic research of IMPE on other post-Si material systems: Ge, III-Vs for example. The difficulty for such kind of study may be attributed to the much stronger background SHG from the bulk due to the absence of inversion symmetry (for III-V compound semiconductors), and/or larger surface recombination rate due to poorer interface quality. So innovative signal detection technique (which can isolate the interface specific contribution from the dominant bulk background), better interface passivation process (which may enhance charge injection at interface due to reduced competing surface recombination), and especially the possible replacement of Si by these materials may inspire more profound research in the very near future.

Due to the limited laser spot size of the scanning SH microscope designed to study APB defects in the epi GaAs, this far field imaging technique can not directly resolve the single domain structure. So a future study might focus on a near field

scanning SH microscope which could provide enough resolution for direct imaging of individual domain structure.[82, 83] For the HEMT sample discussed in Chapter 4, a detailed model and analysis is still needed to explain why the rotational anisotropy from on-axis sample shows 3-fold and 6-fold rotational symmetry rather than 4-fold symmetry.

As for the strain field study on TSV samples discussed in Chapter 5, more work still needs to be done to fully understand the results. The major challenges to establish an analytic model are the complexity of strain distribution and the tensor nature of nonlinear susceptibility. Both normal stress and shear stress may contribute to the break of crystal symmetry. Thus a way to isolate each contribution is prerequisite for the potential application of this metrology. An independent control measurement from a sample under known stress distribution may help understand the strain effect on SHG [90-94].

Appendix A: PHENOMENOLOGICAL MODEL OF SHG FROM SOI

Following the conventions for physical quantities listed in chapter 2.1, from the wave number $\tilde{\omega}_0 = \frac{2\pi}{\lambda_0}$, we can define the normal component (along *z* axis) of wave number $w_0 = \tilde{\omega}_0 \times \cos\theta_0$, and the in-plane component (projection along the interface) $\kappa = \sqrt{\tilde{\omega}_0^{\,2} - w_0^{\,2}}$. Similarly inside SiO_2, we can have $\tilde{\omega}_1 = n_1\tilde{\omega}_0$, $w_1 = \sqrt{\tilde{\omega}_1^{\,2} - \kappa^2} = \tilde{\omega}_1 \cos\theta_1$, where n_1 is the complex index of refraction and θ_1 is the angle inside SiO_2 related to incident angle θ_0 following Fresnel's law: $\sin\theta_0 = n_1 \sin\theta_1$ which also indicates the continuity of in-lane wave number κ. And we can also define these quantities for SH wave as well: $\tilde{\Omega}_0 = 2\tilde{\omega}_0$, $\tilde{\Omega}_1 = N_1\tilde{\Omega}_0$, $W_0 = \tilde{\Omega}_0 \times \cos\theta_0$, $\mathrm{K} = \sqrt{\tilde{\Omega}_0^{\,2} - W_0^{\,2}}$, $W_1 = \sqrt{\tilde{\Omega}_1^{\,2} - \mathrm{K}^2} = \tilde{\Omega}_1 \times \cos\Theta_1$, $\sin\theta_0 = N_1 \sin\Theta_1$. Thus the Fresnel's factors can be written by the above wave number components: $f_s = \frac{\kappa}{\tilde{\omega}_2}$, $f_c = \frac{w_2}{\tilde{\omega}_2}$ for fundamental field inside Si, and $F_{1s} = \frac{\mathrm{K}}{\tilde{\Omega}_1}$, $F_{1c} = \frac{W_1}{\tilde{\Omega}_1}$, $F_{2s} = \frac{\mathrm{K}}{\tilde{\Omega}_2}$, $F_{2c} = \frac{W_2}{\tilde{\Omega}_2}$ for SH wave inside SiO_2 and Si according to the subscript.

From the macroscopic Maxwell's equations:

$$\vec{\nabla} \cdot \vec{E} = -\frac{4\pi}{\varepsilon}\vec{\nabla} \cdot \vec{P} \ , \tag{A1.1}$$

$$\vec{\nabla} \times \vec{B} + i\tilde{\Omega}\varepsilon\vec{E} = -4\pi i\tilde{\Omega}\vec{P} \ , \tag{A1.2}$$

$$\vec{\nabla} \cdot \vec{B} = 0 \ , \tag{A1.3}$$

$$\vec{\nabla} \times \vec{E} - i\tilde{\Omega}\vec{B} = 0 \ , \tag{A1.4}$$

with localized source $\vec{P} = \vec{\eta}\delta(z - z_0^+)e^{i\vec{\mathrm{K}}\cdot\vec{R}}$, where $\vec{R} = \vec{x} + \vec{y}$, the general solution can be written as

$$\vec{E}(\vec{r}) = \vec{E}_+(\vec{r})e^{-iWz_0}\theta(z - z_0) + \vec{E}_-(\vec{r})e^{-iWz_0}\theta(z_0 - z) + \vec{\xi}\delta(z - z_0)e^{i\vec{\mathrm{K}}\cdot\vec{R}},$$

$$\vec{B}(\vec{r}) = \vec{B}_+(\vec{r})e^{-iWz_0}\theta(z - z_0) + \vec{B}_-(\vec{r})e^{-iWz_0}\theta(z_0 - z) + \vec{\zeta}\delta(z - z_0)e^{i\vec{\mathrm{K}}\cdot\vec{R}}.$$

The electromagnetic field is decomposed in the beam coordinate: $\vec{E}_{\pm}(\vec{r}) = (E_{s\pm}\hat{s} + E_{p\pm}\hat{p}_{\pm})e^{i\vec{V}_{\pm}\cdot\vec{r}}$, $\vec{B}_{\pm}(\vec{r}) = (B_{s\pm}\hat{s} \mp B_{p\pm}\hat{p}_{\pm})e^{i\vec{V}_{\pm}\cdot\vec{r}}$, where the subscript '+' denotes the field propagating upward, minus sign for downward, and the polarization unit vectors are written as : $\hat{s} = \hat{x}$, $\hat{p}_{\pm} = F_s\hat{z} \mp F_c\hat{y}$. Substitute this solution into (A2) and (A4), and equate the coefficients of different singularities (δ, δ'), then we have:

$$\vec{E}_{s\pm} = 2\pi i\tilde{\Omega}^2 W^{-1}\hat{s}\cdot\vec{\eta} \ , \qquad \text{(A2.1a)}$$

$$\vec{E}_{p\pm} = 2\pi i\tilde{\Omega}^2 W^{-1}\hat{p}_{\pm}\cdot\vec{\eta} \ , \qquad \text{(A2.1b)}$$

$$\xi_{\kappa} = 0 \ , \qquad \text{(A2.3)}$$

$$\xi_z = -4\pi\varepsilon^{-1}\eta_z \ , \qquad \text{(A2.4)}$$

$$\vec{\zeta} \equiv 0 \qquad \text{(A2.5).}$$

Note that only $\vec{E}_{s\pm}$ and $\vec{E}_{p\pm}$ are the propagating fields.

The solution for the bulk SHG is slightly different due to the nonlocalized nature of polarization source term, thus a green function algorithm proposed in reference [33] is used to obtain this solution:

$$\vec{E}(\vec{\mathrm{K}}, z) = \int \vec{\vec{G}}(\vec{\mathrm{K}}, z - z')\cdot\vec{P}(\vec{\mathrm{K}}, z')dz' \qquad \text{(A3).}$$

And the kernel is

$$\begin{aligned}\vec{\vec{G}}(\vec{\mathrm{K}}, z) = {} & 2\pi i\tilde{\Omega}^2 W_2^{-1}(\hat{s}\hat{s} + \hat{p}_+\hat{p}_+)\theta(z)e^{iW_2 z} \\ & + 2\pi i\tilde{\Omega}^2 W_2^{-1}(\hat{s}\hat{s} + \hat{p}_-\hat{p}_-)\theta(-z)e^{-iW_2 z} \ , \\ & - 4\pi\varepsilon_2^{-1}\hat{z}\hat{z}\delta(z)\end{aligned}$$

where $\theta(z) = \begin{cases} 1 & , \ z > 0 \\ 0 & , \ z \le 0 \end{cases}$. The first two term represent the field propagating upward ($z > 0$) and downward ($z < 0$) respectively. Thus once the polarization density is known, we can write down the SH radiation from both interface and bulk from equations (A2.1) and (A3). Before doing that, we need to find out the fundamental field inside Si by transfer matrix technique [31].

For a multi-layer structure with each medium denoted by m_1, m_2,…, m_n as shown in figure A1, we can define the corresponding transfer matrix M_{ij} at each interface between medium m_i and m_j, as well as the matrix M_i within media m_i with thickness d_m:

$$M_{ij} = \frac{1}{t_{ij}}\begin{bmatrix} 1 & r_{ij} \\ r_{ij} & 1 \end{bmatrix} \qquad \text{and} \qquad M_i = \begin{bmatrix} e^{iw_m d_m} & 0 \\ 0 & e^{-iw_m d_m} \end{bmatrix}.$$

The first matrix M_{ij} represents the reflection and transmission at each interface, and the matrix M_i denotes the propagation within each media.

Thus we can define the total transfer matrix for the propagation through a series of media from m_1 to m_n as:

$$\begin{aligned} M_{1n} &= \frac{1}{T_{1n}}\begin{bmatrix} T_{1n}T_{1n} - R_{1n}R_{1n} & R_{1n} \\ -R_{1n} & 1 \end{bmatrix} \\ &= M_{12} \times M_2 \times M_{23} \times \cdots \times M_n , \end{aligned} \tag{A4}$$

where T_{1n} and R_{1n} is the total transmission and reflection from this multi-layer structure. Thus for an arbitrary structure the total transitivity and reflectivity can be obtained from the transfer matrix element:

$$T = 1/M(4,4) \quad \text{and} \quad R = M(1,2)/M(4,4) \tag{A5}.$$

The typical transfer matrices at the interfaces between the media encountered in this problem can be written by the optical constants and wave number components from the boundary condition:

$$r_{10}^p = \frac{w_1 - w_0\varepsilon_1}{w_1 + w_0\varepsilon_1} = -r_{01}^p , \tag{A6.1}$$

$$t_{10}^p = \frac{2w_1 n_1}{w_1 + w_0\varepsilon_1} , \tag{A6.2}$$

$$r_{12}^p = \frac{w_1\varepsilon_2 - w_2\varepsilon_1}{w_1\varepsilon_2 + w_2\varepsilon_1} = -r_{21}^p , \tag{A6.3}$$

$$t_{12}^p = \frac{2w_1 n_1 n_2}{w_1\varepsilon_2 + w_2\varepsilon_1} , \tag{A6.4}$$

$$t_{21}^{p} = \frac{2w_2 n_1 n_2}{w_1 \varepsilon_2 + w_2 \varepsilon_1} \qquad \text{(A6.5).}$$

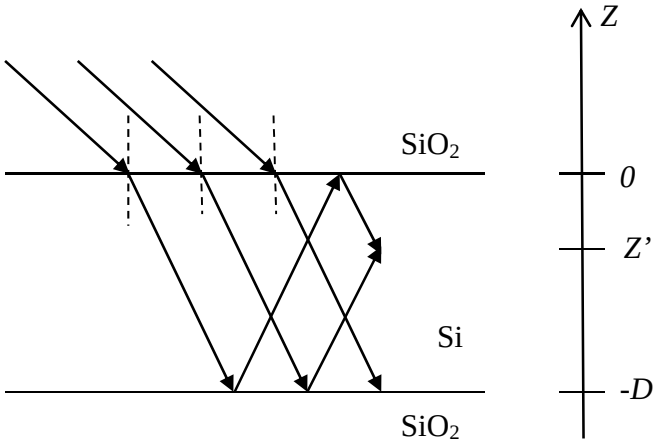

Figure A2: Multiple reflection of fundamental wave inside SOI film

Thus the total *p*-polarized fundamental field inside the SOI film due to internal multiple reflection as demonstrated in figure A2 can be written as: $\vec{E}(z) = \hat{p}_{-} e^{-iw_2 z} E_p + \hat{p}_{+} r_{bd}^{p} e^{2iw_2 D} e^{iw_2 z} E_p + \hat{p}_{-} r_{bd}^{p} r_{bo}^{o} e^{2iw_2 D} e^{-iw_2 z} E_p + \hat{p}_{+} r_{bd}^{p} r_{bo}^{p} r_{bd}^{p} e^{4iw_2 D} e^{iw_2 z} E_p + \ldots$,

where E_p is the fundamental field at $z = 0^{-}$ which is related to the incident field by $E_p = E_0 T_{ob}^{p}$ and each term corresponds to one more reflection at Si/SiO_2 interface. From this multiple reflection series the Cartesian components of electric field are:

$$\begin{aligned} E_z(z) &= \frac{E_p f_s}{1 - r_{bd}^{p} r_{bo}^{p} e^{2iw_2 D}} e^{-iw_2 z} + \frac{E_p f_s r_{bd}^{p} e^{2iw_2 D}}{1 - r_{bd}^{p} r_{bo}^{p} e^{2iw_2 D}} e^{iw_2 z} \\ &= E_p f_s [a(D) e^{-iw_2 z} + b(D) e^{iw_2 z}] \end{aligned} \qquad \text{(A7.1)}$$

,

$$\begin{aligned} E_y(z) &= \frac{E_p f_c}{1 - r_{bd}^{p} r_{bo}^{p} e^{2iw_2 D}} e^{-iw_2 z} + \frac{-E_p f_c r_{bd}^{p} e^{2iw_2 D}}{1 - r_{bd}^{p} r_{bo}^{p} e^{2iw_2 D}} e^{iw_2 z} \\ &= E_p f_c [a(D) e^{-iw_2 z} - b(D) e^{iw_2 z}] \end{aligned} \qquad \text{(A7.2).}$$

The reflectivity for each effective interface can be obtained from transfer matrix method mentioned before: $r_{bd}^{p} = r_{21}^{p} + \frac{t_{21}^{p} r_{12}^{p} t_{12}^{p} e^{2iw_1\delta}}{1 - r_{12}^{p} r_{12}^{p} e^{2iw_1\delta}}$, $r_{bo}^{p} = r_{21}^{p} + \frac{t_{21}^{p} r_{10}^{p} t_{12}^{p} e^{2iw_1 q}}{1 - r_{12}^{p} r_{10}^{p} e^{2iw_1 q}}$.

From the symmetry of Si(001) plane, the only nonzero $\chi^{(2)}$ components are $\chi_{xxz}^{(2)} = \chi_{yyz}^{(2)}$, $\chi_{zxx}^{(2)} = \chi_{zyy}^{(2)}$ and $\chi_{zzz}^{(2)}$. So the susceptibility tensor can be written in contract form:

$$\begin{bmatrix} p_x \\ p_y \\ p_z \end{bmatrix} = \begin{bmatrix} 0 & 0 & 0 & 0 & d_{15} & 0 \\ 0 & 0 & 0 & d_{15} & 0 & 0 \\ d_{31} & d_{31} & d_{33} & 0 & 0 & 0 \end{bmatrix} \begin{bmatrix} E_x^2 \\ E_y^2 \\ E_z^2 \\ 2E_yE_z \\ 2E_xE_z \\ 2E_xE_y \end{bmatrix} \quad \text{(A8).}$$

$$= \begin{bmatrix} 2d_{15}E_xE_z \\ 2d_{15}E_yE_z \\ d_{31}E_x^2 + d_{31}E_y^2 + d_{33}E_z^2 \end{bmatrix}$$

Thus at $z = 0^+$, we have

$$\vec{P}(0^+) = \begin{bmatrix} 0 \\ 2d_{15}E_y(0)E_z(0) \\ d_{31}E_y^2(0) + d_{33}E_z^2(0) \end{bmatrix}.$$

According to equation (A2), the SHG from interface I (NOX/SOI) then takes the form:

$$E_I^p = 2\pi i\tilde{\Omega}^2 W_1^{-1} \times \frac{T_{10}^{p} e^{iW_1 q}}{1 - R_{10}^{p} R_{ad}^{p} e^{2iW_1 q}} \times [F_{1s}(1 + R_{ad}^{p})P_z(0) - F_{1c}(1 - R_{ad}^{p})P_y(0)] \quad \text{(A9.1).}$$

Similarly, at $z = -D$, the SH field from interface II (SOI/BOX) can be expressed as:

$$E_{II}^p = 2\pi i\tilde{\Omega}^2 W_1^{-1} \times \frac{T_{co}^{p}}{1 - R_{co}^{p} R_{12}^{p} e^{2iW_1\delta}} \times \quad \text{(A9.2).}$$
$$[F_{1s}(1 + R_{10}^{p} e^{2iW_1\delta})P_z(-D) - F_{1c}(1 - R_{10}^{p} e^{2iW_1\delta})P_y(-D)]$$

And at $z = -D - \delta$,

$$E_{III}^{p} = 2\pi i\tilde{\Omega}^{2}W_{1}^{-1} \times \frac{T_{co}^{p} e^{iW_{1}\delta}}{1 - R_{co}^{p} R_{cd}^{p} e^{2iW_{1}\delta}} \times \\ [F_{1s}(1 + R_{cd}^{p})P_{z}(-D - \delta) - F_{1c}(1 - R_{cd}^{p})P_{y}(-D - \delta)] \quad \text{(A9.3).}$$

For Si(001) plane, the polarization density of anisotropic bulk SHG from SOI film can be written as [32]:

$$p_{y}(z) = i\tilde{\omega}_{2}n_{2}\zeta\frac{1}{4}f_{s}(\cos 4\phi + 3)f_{c}^{2}E_{p}^{2}[a^{2}(D) \times e^{-2iw_{2}z} + b^{2}(D) \times e^{2iw_{2}z} \\ - 2a(D) \times b(D)] \quad \text{(A10.1)}$$

,

$$p_{z}(z) = -i\tilde{\omega}_{2}n_{2}\zeta f_{s}^{2}f_{c}E_{p}^{2}[a^{2}(D) \times e^{-2iw_{2}z} - b^{2}(D) \times e^{2iw_{2}z}] \ , \quad \text{(A10.2)}$$

where ϕ is the azimuthal angle which denotes the angle between the incident plane and crystalline [100] direction.

Substituting equations (A10) into (A3), we can solve the anisotropic SHG contribution from SOI film:

$$E_{SOI}^{p} = i\pi\tilde{\Omega}_{2}^{3}n_{2}\zeta W_{2}^{-1}E_{p}^{2} \times \frac{T_{bo}^{p}}{1 - R_{bo}^{p}R_{bd}^{p}e^{2iW_{2}D}} \times \\ \Big\{f_{s}^{2}f_{c}F_{2s} \times [a^{2}\frac{1 - e^{i(W_{2}+2w_{2})D}}{W_{2} + 2w_{2}} - b^{2}\frac{1 - e^{i(W_{2}-2w_{2})D}}{W_{2} - 2w_{2}} \\ - R_{bd}^{p}e^{2iW_{2}D} \times (a^{2}\frac{1 - e^{i(W_{2}-2w_{2})D}}{W_{2} - 2w_{2}} - b^{2}\frac{1 - e^{i(W_{2}+2w_{2})D}}{W_{2} + 2w_{2}})] + \quad \text{(A11).} \\ \frac{f_{c}^{2}f_{s}(\cos 4\phi + 3)}{4}F_{2c} \times [a^{2}\frac{1 - e^{i(W_{2}+2w_{2})D}}{W_{2} + 2w_{2}} + b^{2}\frac{1 - e^{i(W_{2}-2w_{2})D}}{W_{2} - 2w_{2}} - 2ab\frac{1 - e^{iW_{2}D}}{W_{2}} + \\ R_{bd}^{p}e^{2iW_{2}D} \times (a^{2}\frac{1 - e^{i(W_{2}-2w_{2})D}}{W_{2} - 2w_{2}} + b^{2}\frac{1 - e^{i(W_{2}+2w_{2})D}}{W_{2} + 2w_{2}} - 2ab\frac{1 - e^{-iW_{2}D}}{W_{2}})]\Big\}$$

And the bulk quadrupolar SHG from the substrate:

$$E_{sub}^{p} = \frac{i\pi\tilde{\Omega}_{2}^{3}n_{2}\zeta W_{2}^{-1}}{4} \times \frac{T_{do}^{p}}{W_{2} + 2w_{2}} \times f_{s}(\frac{T_{od}^{p}}{T_{ob}^{p}})^{2}E_{p}^{2} \times \\ [f_{c}^{2}F_{2c}\cos 4\phi + 3f_{c}^{2}F_{2c} + 4F_{2s}f_{s}f_{c}] \quad \text{(A12).}$$

Thus the total SHG is coherent superposition of all the above SH fields:

$$E_{Total}^{p} = E_{I}^{p} + E_{II}^{p} + E_{III}^{p} + E_{SOI}^{p} + E_{sub}^{p} \quad \text{(A13).}$$

Appendix B: DIRECTORY OF SAMPLE SOURCES

Materials	Grower/Source(contact)/Vendor
50 nm SOI	Sigen (contact sigen.com)
SOI with DOX and all samples related to chemical etching process	Ming Lei (performed at Pickle's Research Center, see Section 2.2 for description of growth procedure)
TCV on glass	Dr. Diego R. Yankelevich from UC Davis (yankelev@ece.ucdavis.edu, see Reference [37] for detailed growth procedure)
ALS BeO on Si	J. H. Yum (jung.hwan.yum@sematech.org, see Reference [62] for detailed growth procedure)
Epi $In_xGa_{(1-x)}As$ on GaAs, Epi GaAs	Man Hoi Wong from SEMATECH (ManHoi.Wong@sematech.org), Jimmy Price from SEMATECH (Jimmy.Price@sematech.org)
TSV	Prof. Paul Ho from UT Austin, Zhuujie Wu (wuzj@physics.utexas.edu)

Appendix C: DIRECTORY OF DIAGNOSTIC EQUIPMENT

Instrument	Location
J.A. Woollam spectroscopic ellipsometer M2000	Microelectronic Research Center (training contact: mertech@mer.utexas.edu)
All semiconductor processing (cleaning, etching deposition, PDA, etc)	Microelectronic Research Center (training contact: mertech@mer.utexas.edu)
SEM	Center for Nano- and Molecular Science (FNT 3.110)
confocal scanning microscope	Patterson Microscopy Center (Patterson building, RM 334, training contact: wes@mail.utexas.edu)
XRD	SVTC (Jimmy.Price@sematech.org)
HRTEM	Albany (Dr. Kathy Dunn, Dr. PY Hung)
Scanning SH Microscope	RLM 2.408 (built by Ming Lei, leiming@physics.utexas.edu)
IPE	RLM 2.408 (built by Ming Lei, leiming@physics.utexas.edu)

Training is required for all the equipment listed here

Bibliography

[1] R. H. Dennard, F. H. Gaensslen, L. Kuhn, and H. N. Yu, IEDM Tech. Dig., 168 (1972).

[2] Jean-Pierre Colinge and Cynthia A. Colinge, Physics of Semiconductor Devices (Kluwer Academic Publishers, New York, 2002).

[3] G. K. Celler and S. Cristoloveanu, J. Appl. Phys. **93**, 4955 (2003).

[4] S. Renn, C. Raynaud, J. Pelloie and F. Balestra, IEEE Trans. Electron Devices, **45**, 2146 (1998).

[5] B. Jun, R. D. Schrimpf, D. M. Fleetwood, Y. V. White, F. Brunier, N. Bresson, S. Cristoloveanu and N. H. Tolk, Appl. Phys. Lett. **85**, 3095 (2004).

[6] M. Alles, R. Pasternak, X. Lu, N. Tolk, R. Schrimpf, D. Fleerwood, R. Dolan and R. Standley, IEEE Trans. Semicond. Manuf., **20**, 107 (2007).

[7] K. Pedersen and T. G. Pedersen, J. Opt. Soc. Am. B, **26**, 917 (2009).

[8] S. Thompson, P. Packan, and M. Bohr, Intel Tech. J. **2**, (Q3, 1998).

[9] C. T. Liu, IEDM Tech. Dig., 174 (1998).

[10] P. T. Wringt and K. C. Saraswat, IEEE Trans. Electron Dev., **37**, 1884 (1990).

[11] S. H. Lo, D. A. Buchanan, Y. Taur, and W. Wang, IEEE Electron Dev. Lett., **18**, 209 (1997).

[12] G. D. Wilk, R. M. Wallace, and J. M. Anthony, J. Appl. Phys., **89**, 5243 (2001).

[13] O. A Aktsipetrov, A. A. Fedyanin, A. V. Melnikov, E. D. Mishina, A. N. Rubtsov, M. H. Anderson, P. T. Wilson, M. ter Beek, X. F. Hu, J. I. Dadap, and M. C. Downer, Phys. Rev. B **60**, 8924 (1999).

[14] V. V. Afanas'ev and A. Stesmans, J. Appl. Phys. **102**, 081301 (2007).

[15] J. Bloch, J. Mihaychuk, and H. van Driel, Phys. Rev. Lett. **77**, 920 (1996).

[16] Z. Marka, R. Pasternak, S. N. Rashkeev, Y, Jiang, S. T. Pantelides, and N. H. Tolk, Phys. Rev. B **67**, 045302 (2003).

[17] J. J. H. Gielis, B. Hoex, M. C. M. van de Sanden, and W. M. M. Kessels, J. Appl. Phys. **104**, 073701 (2008).

[18] J. Price, Y. Q. An, P. Lysaght, G. Bersuker, and M. C. Downer, Appl. Phys. Lett. **95**, 52906 (2009).

[19] M. Lei, J. Price, and M. C. Downer, Appl. Phys. Lett. **96**, 241105 (2010).

[20] M. Lei, J. H. Yum, J. Price, T. W. Hudnall, C. W. Bielawski, S. K. Banerjee, P. S. Lysaght. G. Bersuker and M. C. Downer, *Appl. Phys. Lett.* **100**, 122906 (2012).

[21] S. L. Wright, H. Kroemer, and M. Inada, J. Appl. Phys. **55**, 2916 (1984).

[22] S. Kalem, J. Chyi, C. W. Litton, H. Morkoc, S. C. Kan, and A. Yariv, Appl. Phys. Lett. **53**, 562 (1988).

[23] M. Yata, Thin Solid Films **137**, 79 (1986).

[24] T. S. Rao, J. B. Webb, D. C. Houghton, J. M. Baribeau, W. T. Moore, and J. P. Noad, Appl. Phys. Lett. **53**, 51 (1988).

[25] J. Chyi, D. Biswas, S. V. Iyer, N. S. Kumar, H. Morkoc, R. Bean, K. Zanio, R. Grober, and D. Drew, J. Vac. Sci. Technol. B. **7**, 345 (1989).

[26] M. Razeghi, F. Omnes, M. Defour, and P. Maurel, Appl. Phys. Lett. **52**, 209 (1988).

[27] M. Razeghi, R. Blondeau, M. Defour, F. Omnes, and P. Maurel, Appl. Phys. Lett. **53**, 854 (1988).

[28] S. F. Fang, K. Adomi, S. Lyer, H. Morkoc, H. Zabel, C. Choi, and N. Otsuka, J. Appl. Phys. **68**, R31(1990).

[29] H. Kroemer, J. Cryst. Growth **81**, 193 (1987).

[30] P. R. Pukite and P. I. Cohen, J. Cryst. Growth **81**, 214 (1987).

[31] D. S. Bethune, J. Opt. Soc. Am. B **6**, 910 (1989)

[32] J. E. Sipe, D. J. Moss, and H. M. van Driel, Phys. Rev. B **35**, 1129 (1987)

[33] J. E. Sipe, J. Opt. Soc. Am. B **4**, 481 (1987)

[34] S. Farrens, J. Dekker, J. Smith, and B. Roberds, J Electrochem. Soc., **142,** 3949 (1995).

[35] O. Naumova, E. Vohmina, T. Gavrilova, N. Dudchenko, Mater. Sci. Eng. B **135,** 238 (2006)

[36] P. T. Wilson, Y. Jiang, R. Carriles and M. C. Downer, J. Opt. Soc. Am. B **20**, 2548 (2003)

[37] D. R. Yankelevich, P. Pretre, A. Knoesen, G. Taft, M. M. Murnane, H. C. Kapteyn and R. J. Twieg, Opt. Lett. **21**, 1487 (1996).

[38] E. D. Palik, *Handbook of Optical Constants of Solids* (Academic Press 1995).

[39] K. Kim and D. Choi, J. Mater. Sci. Lett., **20**, 245 (2001).

[40] Mitsuo Takeda, Hideki Ina and Seiji Kaobayashi, J. Opt. Soc. Am. **72**, 1 (1982).

[41] S. M. Sze and Kwok K. Ng, *Physics of semiconductor devices*, 2nd Edition (Wiley, New York, 1981).

[42] R. J. Powell, J. Appl. Phys. **41**, 2424 (1970).

[43] V. V. Afanas'ev, M. Houssa, A. Stesmans, G. J. Adraenssens, and M. M. Heyns, J. Non-Crystalline Solids, **303**, 69 (2002).

[44] V. V. Afanas'ev, M. Houssa, A. Stesmans, and M. M. Heyns, J. Appl. Phys. **91**, 3079 (2002).

[45] M. Lei, J. H. Yum, S. K. Banerjee, G. Bersuker, and M. C. Downer, Physica status solidi B, 249, 1160 (2012).

[46] C. N. Berglund and R. J. Powell, J. Appl. Phys. **42**, 573 (1971).

[47] D. J. Maria and P. C. Arnett, IBM J. Res. Dev. **21**, 227 (1977).

[48] I. S. Chen and C. R. Wronski, J. Non-Crystalline Solids, **190**, 58 (1995).

[49] G. Lucovsky, G. B. Rayner, Jr., D. Kang, G. Appel, R. S. Johnson, Y. Zhang, D. E. Sayers, H. Ade, And J. L. Whitten, Appl. Phys. Lett. 79, 1775 (2001).

[50] J. H. Yum, T. Akyol, M. Lei, K. W. Park, T. W. Hudnall, M. C. Downer, C. W. Bielawski, G. Bersuker. E. T. Yu, J. Price, J. C. Lee and S. K. Banerjee, IEEE Teans. Electron Dev., **58**, 4384 (2011)

[51] T. H. DiStefano and D. E. Eastman, Sol. State Commun. **9**, 2259 (1971).

[52] V. V. Afanas'ev, A. Stesmans, C. Zhao, M, Caymax, T. Heeg, J. Schubert, Y. Jia, D. G. Schlom and G. Lucovsky, Appl. Phys. Lett. **85**, 5917 (2004).

[53] V. V. Afanas'ev, Internal Photoemission Spectroscopy: Principles and Applications (Elsevier, 2008).

[54] Patrick S. Lysaght, Joel Barnett, Gennadi I. Bersuker, Joweph C. Woicik, Daniel A. Fischer, Brendan Foran, Hsing-Huang Tseng and Raj Jammy, J. Apply. Phys. **101**, 24105 (2007).

[55] G. Bersuker, C. S. Park, J. Barnett, P. S. Lysaght, P. D. Kirsch, C. D. Young, R. Choi, B. H. Lee, B. Foran, K. Van Benthem, S. J. Pennycook, P. M. Lenahan, and J. T. Ryan, J. Appl. Phys. **100,** 094108-6 (2006).

[56] J. T. Ryan, P. M. Lenahan, G. Bersuker, and P. Lysaght, Appl. Phys. Lett. **90,** 173513 (2007).

[57] David Chi and P. C. McIntyre, Appl. Phys. Lett. **85,** 4699 (2004).

[58] G. Lucovsky, G. B. Rayner, Jr., D. Kang, G. Appel, R. S. Johnson, Y. Zhang, D. E. Sayers, H. Ade, And J. L. Whitten, Appl. Phys. Lett. 79, 1775 (2001).

[59] S. Sayan, T. Emge, E. Garfunkel, Xinyuan Zhao, L. Wielunski, R. A. Bartynski, David Vanderbilt, J. S. Suehle, S. Suezer, and M. Banaszak-Holl, J. Apply. Phys. 96, 7485 (2004).

[60] E. Bersch, S. Rangan, R. A. Bartynski, E. Garfunkel, and E. Vescovo, Phys. Rev. B **78**, 85114 (2008).

[61] C. Y. Yim, D. H. Ko, M. H. Jang, K. B. Chung, M. H. Cho, and H. T Jeon, Appl. Phys. Lett. **92**, 12922 (2008).

[62] J. H. Yum, T. Akyol, M. Lei, T. Hudnall, G. Bersuker, M. C. Downer, C. W. Bielawski, J. C. Lee, and S. K. Banerjee, J. Apply. Phys. **109**, 064101 (2011).

[63] K. J. Hubbard and D. G. Schlom, J. Mater. Res., **11**, 11, (1996).

[64] J. H. Yum, T. Akyol, D. A. Ferrer, J. C. Lee, S. K. Banerjee, M. Lei, M. Downer, Todd. W. Hudnall, C. W. Bielawski and G. Bersuker, J. Vac. Sci. Technol. A, 29, 061501 (2011).

[65] V. K. Adamchuk and V. V. Afanas'ev, Prog. Surface Sci., **41**, 111 (1992).

[66] V. A. Sashin, M. A. Bolorizadeh, A. S. Kheifets and M. J. Ford, J. Phys.:Condens. Matter 15, 3567 (2003).

[67] A. Stroppa and M. Peressi, Phys. Rev. B, **71**, 205303 (2005).

[68] J. F. Nye, Physical Properties of Crystals (Oxford, 1985).

[69] J. E. Ayers, J. Crystal Growth, **135**, 71 (1994).

[70] L. Vegard, Z. Phys. **5**, 17 (1921).

[71] J. C. Woolley and B. C. Smith, Proc. Phys. Soc. London, **72**, 214 (1958).

[72] J. Zou, D. J. H. Cockayne, and B. F. Usher, J. Appl. Phys. **73**, 619 (1993).

[73] Yu B Bolkhovityanov and O PPechelyakov, Physics Uspekhi **51**, 437 (2008).

[74] P. R. Pukite and P. I. Cohen, Appl. Phys. Lett. **50**, 1739 (1987).

[75] R. J. Pressley, Handbook of Lasers(CRC, Cleveland, OH, 1971).

[76] D. J. Bottomley, G. Luke, J. G. Mihaychuk, and H. M. van Driel, J. Appl. Phys. **74**, 6072 (1993).

[77] D. B. Holt, C. Hardingham, L. Lazzarini, L. Nasi, C. Zanotti-Fregonara, G. Salviati, and M. Mazzer, Mater. Sci. Eng., **B42**, 204 (1996).

[78] Richard Beeler, Jay Mathews, Change Weng, John Tolle, Radek Roucka, A.V.G. Chizmeshya, Reid Juday, Sampriti Bagchi, Jose Menendez, and John Kouvetakiz, Solar Energy Materials & Solar Cells, **94**, 2362 (2012).

[79] Yuan Li, and L. J. Giling, J. Cryst. Growth **163**, 203 (1996).

[80] K. Wu, J. D. Canterbury, P. T. Wilson, and M. C. Downer, phys. Stat. sol. (c), **8**, 3081 (2003).

[81] C. Meyer, G. Lüpke, E. Stein von Kamienski, A. Gölz, and H. Kurz, Appl. Phys. Lett. 69 2243 (1996).

[82] I. I. Smolyaninov, A. V. Zayats and C. C. Davis, Phys. Rev. B **56**, 9290 (1997).

[83] B. I. Bozhevolnyi, B. Vohnsen and K. Pedersen, Opt. Commun., **150**, 49 (1998).

[84] P. Garrou, C. Bower and P. Ramm, Handbook of 3D Integration: Technology and Applications of 3D Integrated Circuits (Wiley-VCH, 2008), Vols. I-II.

[85] K. H. Lu, X. Zhang, S. Ryu, J. Im, R. Huang, and P. S. Ho, Electronic Components and Technology Conference, pp. 630, (2009).

[86] B. Wunderle, R. Mrossko, O. Wittler, E. Kaulfersch, P. Ramm, B. Michl, H. Reichl, Matter. Res. Soc. Symp. Proc., **970**, 67, (2007).

[87] L. W. Kong, P. Krueger, E. Zschech, A. C. Rudack, S. Arkalgud, and A. Diebold, AIP Conf. Proc. 1300, 221 (2010).

[88] L. W. Kong, J. R. Lloyd, K. B. Yeap, E. Zsxhen, A. Rudack, M. Liehr, and A. Diebold, J. Appl. Phys., 110, 53502 (2011).

[89] C. McDonough, J. Capulong, B. Backes, P. Sigh, L. Smith, W. Wang, and R. E. Geer, Proc. 11th Int. Workshop on Stress-induced Phenomena Metallization (2010).

[90] O. A. Aktsipetrov, V. O. Bessonov, T. V. Dolgova, and A. I. Maidykovskii, JETP Lett. **90**, 718 (2009).

[91] J. Zhao, W. Su, Q. Chen, Y. Jiang, Z. Chen, G. Jia, and H. Sun, IEEE J. Quantum Electron., **47**, 55 (2011).

[92] W. Daum, H. J. Krause, U. Reichel, and H. Ibach, Phys. Rev. Lett., **71**, 1234 (1993).

[94] J. Y. Huang, Jpn. J. Appl. Phys., **33**, 3878 (1994).